THE MINISTRY OF NATIONAL
INFRASTRUCTURES
GEOLOGICAL SURVEY OF ISRAEL

Current Deformation in the Southern Dead Sea Transform: Radar Interferometry Measurements and their Tectonic Implications

Yaron Finzi

This work was submitted as a M.Sc. Thesis to the Institute of Earth Sciences,
The Hebrew University of Jerusalem, under the supervision of:

Prof. Ze'ev Reches, The Institute of Earth Sciences, The Hebrew University of Jerusalem
Dr. Gidi Baer, The Geological Survey of Israel

Jerusalem, June 2005 Report GSI/24/04

ABSTRACT

We present an analysis of recent (1995-2001) tectonic activity along the Arava Valley (AV) section of the Dead Sea Transform (DST) based on Interferometric Synthetic Aperture Radar (InSAR) measurements of surface displacement. We suggest that aseismic deformation detected at AV fault stepovers plays an important role in the seismic moment balance of this section of the DST.

The DST is a left-lateral strike-slip plate boundary between the Arabian plate and the Israel-Sinai sub-plate. The AV is a 160 km long depression in the DST between the Dead Sea in the north and the Gulf of Elat (Aqaba) in the south. It consists of several NNE-striking en-echelon fault segments each a few tens of kilometers long, enclosing small extensional and compressional structures in the major stepover zones. The current slip rate along the DST is poorly constrained and there are some indications that the AV segments are locked and that a seismic gap is forming along them. For example, paleoseismic data indicate decrease in earthquake magnitudes since Late Pleistocene, and a low seismicity level has been measured during the past 15 years.

In order to detect and analyze all observable surface deformation features along the AV, we processed all available SAR data collected by the European Space Agency Remote Sensing Satellites, ERS-1 and ERS-2. Using a hybrid approach of topographic phase construction (combining an independent DEM with a topographic phase constructed from suitable ERS-1 to ERS-2 tandem pairs) we analyzed five ERS frames of both descending and ascending tracks. Interferograms (i.e. surface displacement maps) were generated from almost every possible pair and span periods of 2-74 months between 1995 and 2001. We observed three surface deformation features that are attributed to tectonic processes based on their magnitude, spatial characteristics and on their correlation with active faults. Incorporating our measurements and independent geologic knowledge, fault dislocation models were constructed. Analysis of these models indicates that the observed deformation features are induced by interseismic creep events at fault stepovers within the AV.

At Yotvata Playa, southern AV, uplift of ~120 mm occurred during the period of 3/1995-5/1999 over a shallow reverse fault connecting a right stepover between Elat Fault and Aqaba-Gharandal Fault. The uplift at Yotvata covers an area of approximately 30 km^2,

it is continuous in time with measured displacement rates between 80 mm/yr (3/1995-11/1995) and 10 mm/yr (11/1996-12/1998).

Near Zofar settlement, northern AV, interferograms of ascending and descending tracks reveal subsidence of ~37 mm during the period of 4/1998-10/2000. The subsidence is induced by oblique slip on Zofar Fault (AV western border fault) and normal slip on Wadi-Musa Fault which is a shallow fault traversing the AV. The subsidence at Zofar covers an area of approximately 10 km^2, it is continuous with an average rate of ~15 mm/yr and maximal rate of ~30 mm/yr during the first half of 1999.

At Avrona Basin, southern AV, we detected a complex pattern of local uplift and subsidence features that occurred between 3/1995 and 1/1999. The subsidence features are induced by oblique (left-lateral and normal) slip on four segments of Elat Fault forming two left stepovers, and the uplift is related to oblique (left-lateral and reverse) slip on a right bend in Elat Fault. The average displacement rate of both subsidence features is approximately 15 mm/yr, and the average rate at the uplift feature is 10 mm/yr.

Based on dislocation models, the moment release in each deformation site was calculated. The uplift at Yotvata Playa released $19.7 \cdot 10^{16}$ N·m, equivalent to an earthquake with magnitude M_L~5.5 (assuming instantaneous seismic moment release of $19.7 \cdot 10^{16}$ N·m). The subsidence near Zofar released $5.9 \cdot 10^{16}$ N·m, equivalent to an earthquake with magnitude M_L~5.2. And the complex deformation at Avrona Basin released $12.2 \cdot 10^{16}$ N·m, equivalent to an earthquake with magnitude M_L~5.4. Comparing these results with the seismic record from the AV indicates that during the period of 1995-1999 the aseismic moment release is two orders of magnitude larger than the moment released by seismicity. Assuming that the AV slips at an average rate of 3.1 mm/yr (based on GPS measurements), we suggest that the aseismic displacement released approximately 50% (!) of the moment accumulated along the AV during this time period.

InSAR measurements and their tectonic analysis indicate that during the period of 1995-2001 significant creep occurred along the AV within Yotvata, Zofar and Avrona fault stepover zones. Although no strike slip motions were detected outside of these stepover zones, it is still possible that creep along the intervening AV segments occurs at rates lower than the detection limit of ~4 mm/yr for such motions (less than 25 mm during the study period).

ACKNOWLEDGMENTS

I thank the following for their generous advice during the course of this study:
- my supervisors, Ze'ev Reches and Gidi Baer.
- David Sandwell of Scripps Institute of Oceanography (UCSD) deserves special thanks for his support.
- Michelle Schossberger (Finzi), Ori Dor, Leehee Laronne Ben-Itzhak, Onn Crouvi, Einat Magal, Amotz Agnon, Amos Salamon, Meir Abelson, Ze'ev B. Begin and Rami Hofstetter.
- and to Magi, Mali, Carmella, Batia, Avraham, Debbie, Sharon, Zelda, Mark and Olga, from the geology department at the Hebrew University of Jerusalem.

This work was supported by the U.S.- Israel Binational Science Foundation (BSF).

TABLE OF CONTENT

LIST OF FIGURES

LIST OF TABLES

1. INTRODUCTION

Knowledge of current tectonic activity along the Arava Valley (AV) segment of the Dead Sea Transform (DST) is based primarily on current seismicity and on long-term geologic observations. Space geodetic measurements of surface displacement provide a new and powerful tool to constrain current deformation rates, to detect aseismic surface deformation and to understand the partitioning between seismic and aseismic tectonic activity along the AV. This study applies the Interferometric Synthetic Aperture Radar (InSAR) method to measure surface displacement that occurred along the AV during the years 1995-2001. Using InSAR we calculate the surface deformation field within and around the AV with unsurpassed accuracy and spatial resolution. Three deformation features were measured and analyzed in this work. Tectonic models characterizing the faults and slip distribution that generated the observed surface displacements were constructed. The tectonic analysis of these deformation features indicates that they are induced by aseismic creep. Based on our unprecedented geodetic measurements of creep along the DST, we discuss the role of aseismic creep in the tectonics of the AV.

1.1 Geological setting

1.1.1 The Dead Sea Transform

The Dead Sea Transform is a left-lateral strike-slip plate boundary between the Arabian plate and the Israel-Sinai sub-plate. Since its formation in early Miocene (e.g. Garfunkel, 1981), the DST has accommodated approximately 105 km of sinistral displacement (Quennel, 1959; Freund, 1970), of which at least 30 km post-dated the Miocene (Joffe and Garfunkel, 1987). The DST extends more than 1000 km from the Red Sea in the south, to the Taurus-Zagros collision zone in the north (Figure 1.1). The DST consists of several en-echelon segments that strike in general N15ºE direction, and which create large pull-apart basins such as the Sea of Galilee, the Dead Sea and the Gulf of Elat (Reches et al., 1987). The Jordan and Arava valleys are located in between these basins (Figure 1.1) where relatively simple linear segments of the DST are characterized by almost pure strike slip motion (Garfunkel, 1981).

Figure 1.1. Tectonic setting and main structures within the Arava Valley, Dead Sea Transform. The Southern DST stretches from the Sea of Galilee (SG) in Northern Israel through the Jordan Valley (JV), Dead Sea and Arava Valley (AV), to the Gulf of Elat (Aqaba) and to the Red Sea. The AV stretches from the Dead Sea Basin in the north (gray) to the Gulf of Elat (Aqaba) in the south (blue), it consists of four basins: Shezaf (turquoise), Zofar (pink), Yaalon (green) and Avrona (yellow). In northern AV the basins are separated by Amazyahu Fault (AMF) and Shezaf Fault (SHF). Zofar Basin is traversed by a series of normal faults (dashed lines), the southernmost is Wadi-Musa Fault. The settlements of Zofar (northern AV) and Yotvata and the city of Elat (southern AV) are marked by red dots. PAF and THF are Paran Fault and Themed Fault respectively. AV faults based on Frieslander (2000).

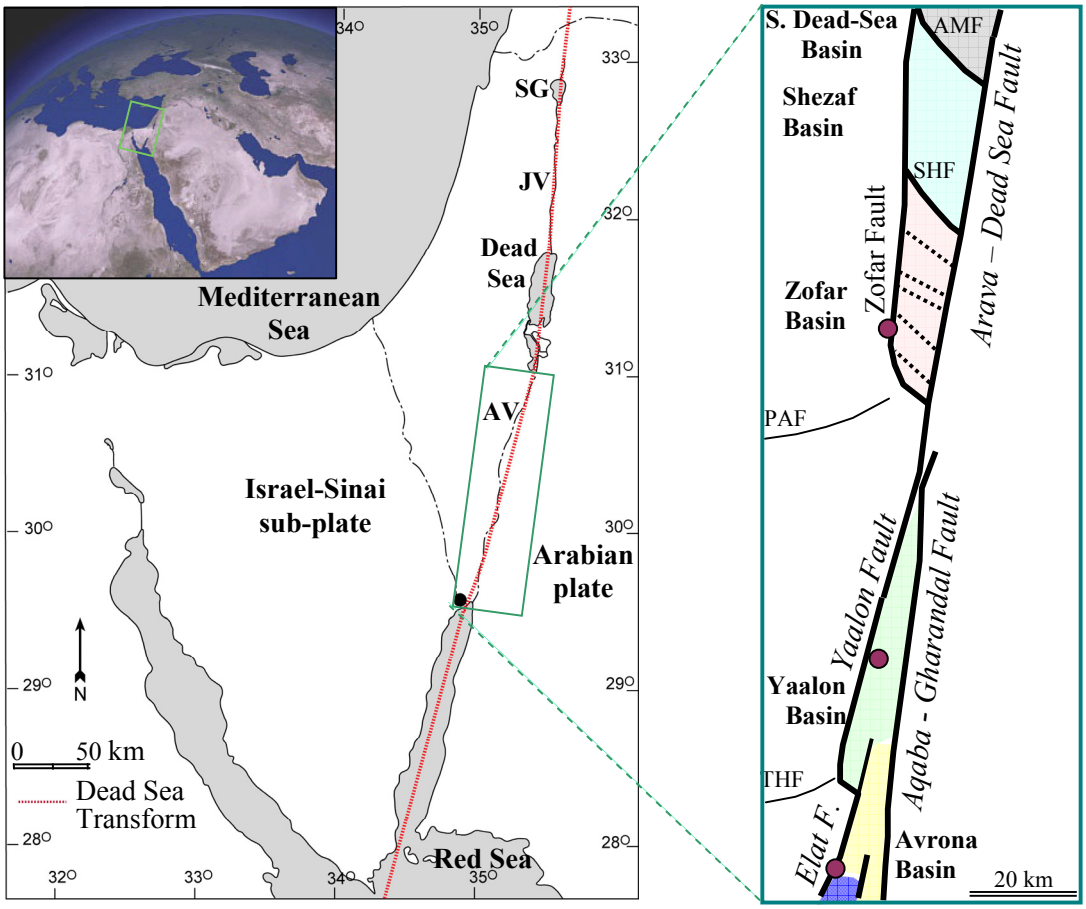

Estimates of the long-term slip rate along the DST range from 6 to 9 mm/yr according to regional plate kinematic models (Garfunkel et al., 1981; Joffe and Garfunkel, 1987) and global tectonics (DeMets et al., 1994) respectively. While the long-term DST slip rate is in general consensus, the short-term slip rate is not well constrained. The estimated short-term slip rate ranges widely, 1-10 mm/yr, depending on the method used and on the region studied. Plate kinematic models and large-scale geological observations suggest

Quaternary slip rates between 7 and 10 mm/yr (Garfunkel et al., 1981; Freund et al., 1968; Reches et al., 1987). Geomorphologic studies based on translocated drainage systems and morphotectonic observations, yield Pliocene-Quaternary slip rates of 2-7.5 mm/yr (Enzel et al., 1994; Ginat et al., 1998; Klinger et al., 2000a). The short-term slip rate derived from historic record of earthquakes and related damage along the DST is considerably lower than the long-term slip rate. Slip rates of 1-4 mm/yr were estimated based on 4500 years of documented earthquakes (Ben-Menahem, 1981; North, 1974). Analysis of seismic observations of the last one hundred years indicates an average slip rate of 1-2 mm/yr (Salamon, 1993). As this estimate preceded the 1995 Nuweiba earthquake sequence, it probably underestimates the current seismic activity along the DST. Archaeological observations of damaged structures near the Sea of Galilee (Figure 1.1) indicate a minimum rate of 2.5 mm/yr during the past 800 years (Marco et al., 1996). The slip rate estimates for the entire DST during the Quaternary are summarized in Table 1.1.

Table 1.1. Slip rate estimates along the DST during the Quaternary (based on Marco, 1996).

Slip Rate (mm/yr)	Relevant period	Method/Data	Reference
7-10	Quaternary	Plate kinematics	Garfunkel et al., 1981,
5.5 – 6	Pleistocene	Geologic	Heimann 1990
10	Late Pleistocene - present	Geologic	Freund et al., 1968
9	Holocene	Geologic	Reches et al., 1987
2-6	Holocene	Morphotectonic	Klinger et al., 2000a
2.2	4500 yr	Historic seismicity	Ben-Menahem 1981
>2.5	800 yr	Archaeologic	Marco et al., 1996
1-2	100 yr	Recorded seismicity	Salamon, 1993

The first geodetic slip rate estimate, based on continuous GPS monitoring (GIL network, Wdowinski et al., 2001), yielded values of 2.6 ±1.1 mm/yr (Pe'eri et at., 2002). However, these measurements were based on three years data from only three GPS stations, located 0, 5.5 and 70 km west of the fault zone. Based on a larger network (11 stations), longer time span (1996-2003) and improved modeling, Wdowinski et al. (in press) estimated the DST slip rate to be 3.3±0.5 mm/yr.

The apparent decrease in slip rate could be partly attributed to the fact that historic slip rates are derived primarily from documented earthquakes and from their traces. The short-term slip rates may not represent an entire seismic cycle and may reflect an incomplete earthquake record due to the sparse population in the region. In addition, the low values of slip rate derived from seismicity could be a reflection of the low seismic efficiency typical of the DST (only 30-50% of the moment accumulated is released in earthquakes; Salamon et al., 2003; Garfunkel et al., 1981).

The DST is the main source of seismicity in the Levant, it has produced over a hundred large earthquakes ($6.0 < M < 8.0$) during the past 4500 yr (Ben-Menahem, 1981). The last major event occurred on the 22/11/1995 in the Gulf of Aqaba (Nuweiba earthquake, M_W=7.2). Paleoseismic studies suggest that several large earthquakes with magnitudes M~7 occurred along the DST since the Pleistocene (Amit et al., 1999; Marco et al., 1996). In addition, there is evidence for decrease in earthquake magnitude and recurrence interval along the Southern DST during the Holocene (Amit et al., 2002). The recorded seismicity of the past 5 decades (GII, 2000) displays a spatially non-uniform distribution with increased activity at major fault stepovers (i.e. Dead Sea, Gulf of Elat and near the Sea of Galilee) and quiescence along the intervening segments (i.e. Arava and Jordan valleys).

1.1.2 The Arava Valley

The Arava Valley is a 160 km long depression between the Dead Sea and the Gulf of Elat (Figure 1.1). The uplifted western and eastern margins of the AV are built of Precambrian basement rocks overlain by Paleozoic to Cenozoic sedimentary and igneous rocks. The AV and the basins within it are filled with Miocene to Holocene clastic sediments with depth between several hundreds of meters to a few kilometers (Zak, 1967; Garfunkel et al., 1981; Freund et al., 1968; Frieslander, 2000). The main fault segment along the AV displays a relatively linear trace that strikes N20˚E. This simple geometry strongly suggests pure strike-slip motion along this segment (Garfunkel et al., 1981). Nevertheless, extensional and compressional jogs, and minor variations of the fault azimuth create topographic features along the AV such as the pressure ridge in central Arava (Garfunkel et al., 1981). The AV consists of several elongated tectonic basins (Figure 1.1) each bordered by sub parallel segments of the DST (Bartov, 1994; Bartov et al., 1998). In northern Arava, the Southern Dead Sea Basin, Shezaf Basin and Zofar Basin

are separated by listric faults striking approximately NW (Frieslander, 2000). In southern AV, the Yaalon Basin is located northwest of the Avrona Basin in a left stepping en-echelon pattern (Frieslander, 2000; ten-Brink et al., 1999) (Figure 1.1).

The current and historic seismicity along the AV is considerably lower than the seismicity of adjacent sections of the DST (GII, 2000; Ben-Menahem, 1981; Ben-Menahem and Aboodi, 1981) apparently forming seismic gaps (Shapira, 1997; Shapira and Shamir, 1994; Salamon, 1993). Although the DST has a long history of destructive earthquakes, only three large historic events were inferred for the Arava Valley region, the earthquakes of 1068, 1212 and 1293 A.D. (Ambraseys et al., 1994; Ben-Menahem, 1991; Zilberman et al., 1998; Amit et al., 2002). Paleoseismic studies along the AV suggest that during the Upper-Pleistocene and Holocene (past 80,000 years), earthquake magnitudes have decreased from a magnitude range of 6.7 - 7 to magnitudes 5.9 - 6.7 (Amit et al., 2002 and references therein). The suggested decrease in earthquake magnitude, combined with the low current and historic seismicity level is interpreted by Amit et al. (2002) as an indication that the AV fault segments are locked and forming a seismic gap.

1.1.3 Current slip rate along the Arava Valley

The current horizontal slip rate along the AV is not well constrained. Geomorphologic observations (Enzel et al., 1994; Ginat et al., 1998; Klinger et al., 2000a) and analysis of seismicity along the Southern DST (Ben-Menahem, 1981; Shapira and Hofstetter, 1993; Klinger et al., 2000b) yield slip rates similar to those of the entire DST (see above). Current GPS measurements by Wdowinski et al. (in press) yielded a slip rate estimate of 3.1±1.1 mm/yr for the Southern DST. The sparse geodetic instrumentation along the Southern DST limits the spatial resolution of slip rate estimates, thus yielding poorly constrained AV slip rates. Some constraints are found, however, for the vertical slip component. Long-term subsidence rates of basins along the AV varies from 0.1 mm/yr at the southern end of Zofar Basin (Frieslander, 2000; based on seismic reflection) to ~1 mm/yr at the Southern Dead Sea Basin (based on Sedom-1 and Amaziahu-1 deep drills; Gardosh et al., 1997; Gardosh et al., 1990). Paleoseismic studies conducted within Avrona Basin (Amit et al., 2002; Amit et al., 1999) inferred a vertical slip rate of 0.1-0.3 mm/yr during the past 14,000 yr. The current subsidence rate of AV basins is not resolved due to insufficient geodetic measurements.

1.2 Geodetic measurement and tectonic analysis of surface deformation at plate boundaries

1.2.1 Monitoring methods and basic analysis approaches

During the past decades several geodetic methods evolved enabling continuous (or frequently repeated) measurement sufficiently accurate for monitoring surface deformation along plate boundaries. Most existing instruments measure the precise position (e.g. GPS, precise leveling) of a point of interest or the distance between two such points (e.g. Electromagnetic Distance Measurement (EDM), Very Long Base-line Interferometry (VLBI), strain-meters). Repeated measurements of an array of interest points can yield a time series describing either the displacement vector of each specific point relative to a reference frame or the two dimensional deformation (i.e. strain) of the measured baselines. In order to monitor the displacement field associated with plate boundaries, vast arrays of continuously measuring instruments are deployed. Examples of such arrays are the SCEC (Southern California Earthquake Center) permanent GPS array (SCIGN) and the strain-meters installed at the Parkfield Earthquake Experiment (Roeloffs and Langbein, 1994). Based on geodetic measurements of surface displacement one can study the current tectonic activity at depth and the slip-rate along plate boundaries. In addition, analysis of surface displacement associated with earthquakes aids in characterizing seismic faults and in evaluation of the seismic risk imposed by them. For example, a suitable array of GPS stations on two sides of a plate boundary may record the strain accumulation and the slip distribution along the fault system, thus revealing fault segments with slip deficit. An important approach to seismic hazard analysis is based on the strain balance on faults. This approach is implemented by basic earthquake models such as the time predictable model (Shimazaki and Nakata, 1980) and the slip predictable model (Kiremidjian and Anagnos, 1984) that compare the geodetic slip rate (representing tectonic strain rate) with the rate of strain release by earthquakes in order to evaluate seismic risk. The geodetic and seismic data are used to evaluate the efficiency in which a fault system releases the strain accumulated on it, and determine whether it is accumulating an excess amount of strain (i.e. forming a seismic gap). Seismic hazard studies of the past few decades also implemented surface displacement measurements and fault models derived from them to

assess the interaction between earthquakes and the implications that large earthquakes have on their tectonic environment (e.g. Ben-Zion et al., 1993; Lienkaemper et al., 2001). Today there is a growing consensus that earthquakes may trigger one another through changes in the regional stress field by means of stress transfer.

Although the DST has been intensively studied for over 50 years, the detection of current plate motion and the measurement of current slip rate were based until lately on seismicity (e.g. Ben-Menahem, 1981; North, 1974) and on archeological findings (e.g. Marco et al., 1996) rather than on geodetic measurements. During the past 20 years, space geodetic measurements of the DST provided the first direct estimates of current plate motion. Early geodetic studies, which used episodic measurements, were able to detect the relative motion between Israel-Sinai, Africa and Eurasia plates (Smith et al., 1994; Karcz et al., 1997). However, due to the low rates of crustal deformation in the region, these measurements were not accurate enough to detect interseismic deformation across the DST (Adler et al., 2001; Ostrovsky, 2001). During the years 1996-2001 a network of 11 continuous GPS stations (GIL network) was constructed in Israel to monitor current crustal movements across the DST (Wdowinski et al., 2001). Data from the GIL network and from additional stations in Amman, Jordan and Damascus, Syria enable evaluation of the current tectonic plate motion in the Eastern Mediterranean. However, due to the limited GPS array along the southern part of the DST (only 5 stations south of 32°N, all west of the DST), the slip rate estimates relevant to the AV are still not well constrained (see 1.1.3).

1.2.2 InSAR contribution and applicability for studying the Dead Sea Transform

Until the advent of space geodesy, measurements of surface displacement relied on terrestrial methods in which repeated surveys revealed deformation of the crust. These methods provide precise measurements of displacement; however, they are time intensive and costly, they are restricted to sparse point measurements, and they do not allow for the direct measurement of three dimensional displacements (Burgmann et al., 2000). During the past few decades space geodetic methods, especially GPS, have overcome some of the limitations of terrestrial geodesy enabling the analysis of crustal deformation on a global scale. Interferometric Synthetic Aperture Radar (InSAR) is the latest addition to space geodesy. Encompassing unique capabilities that complement the existing methods, it enables the study of active deformational processes that were previously inaccessible.

Although the displacement measurement capabilities of InSAR were demonstrated earlier (Gabriel et al., 1989), it was the successful measurement of displacement associated with the 1992 Landers Earthquake, California, that demonstrated the uniqueness of the technique (Massonnet et al., 1993; Zebker et al., 1994b). The InSAR derived coseismic displacement maps and fault models were comparable to data from other geodetic measurements (particularly GPS), to field observation, and to models based on seismic data (Massonnet et al., 1993; Zebker et al., 1994b). The Landers case study proved that InSAR could be applied worldwide to measure surface displacement at dense pixel spacing of ~20 m with precision comparable to GPS and leveling, but without requiring ground stations or fieldwork. Since the Landers Earthquake, a large variety of geophysical studies profit from the advantages of InSAR; these can be classified in three categories: (a) Complex or subtle surface deformation processes with wide spatial extent. Examples for such studies are complex earthquake ruptures (e.g. Price and Sandwell, 1998), surface creep (e.g. Burgmann et al., 2000; Lyons and Sandwell, 2003), triggered slip and post-seismic deformation (Peltzer et al., 1996; Massonnet et al., 1994). (b) Vertical displacement such as associated with volcanic and geothermal activity (Rosen et al., 1996), and with land subsidence (Amelung et al., 1999; Baer et al., 2002). (c) Deformation processes in remote, inaccessible areas, and in regions otherwise not monitored with geodetic instruments (Goldstein et al., 1993; Baer et al., 2001; Baer et al., 2002).

During the past few years InSAR has been applied in several studies of the Dead Sea Transform. These studies demonstrated that the arid conditions and limited anthropogenic activity along the DST combined with good ERS SAR coverage make the region suitable for InSAR. Problems such as inaccessibility and the lack of geodetic arrays monitoring both sides of the plate boundary can now be solved by InSAR. Two examples of InSAR studies along the DST are (a) measurement and analysis of sinkholes and other subsidence features along the Dead Sea shores (Baer et al., 2002), and (b) characterizing the underwater rupture geometry and the slip distribution of the 1995 Nuweiba Earthquake (Baer et al., 1999 and 2001). In the first example, InSAR ability to measure subtle vertical displacements was proven valuable in detecting various types of subsidence features with rates as low as 5 mm/yr. In the second example, InSAR measurements successfully

compensated for the lack of direct observations of the underwater rupture, and were used to refine estimations of fault geometry and slip distribution based on seismology.

1.3 Objectives

The main objective of this study is to characterize the current surface deformation along the Arava Valley, Southern Dead Sea Transform. This work aimed to measure the ground movements along the Arava Valley by processing all available (relevant) SAR data, and to analyze and determine the mechanisms of observable surface deformation features. The analysis of InSAR measurements aimed to isolate and model the deformation generated by tectonic processes. In addition, the tectonic analysis of observed surface deformation features examined their role in the Arava Valley strain balance. We hope that our measurements and tectonic analysis will provide a detailed description of current tectonic activity in the Southern DST, and will strengthen the geodetic basis for studies such as regional tectonics and seismicity, seismic hazard analyses and definitions of active faults.

2. METHODS

2.1 Interferometric Synthetic Aperture Radar (InSAR)

2.1.1 Principles of SAR and InSAR

Since 1978 Earth's crust is being continuously monitored with space-borne radar (Radio Detection And Ranging) instruments. Satellites that are used as platforms for side-looking radar orbit the earth in ascending and descending near polar tracks. Each track is orbited once every repetition cycle. The data from each orbit (of each track) is divided into frames of about 100 km x 100 km, which are the basic processing units. Some basic radar definitions are visualized in Figure 2.1, and parameter values are demonstrated based on the European Remote Sensing satellites (ERS-1,2) which are the data source for this work.

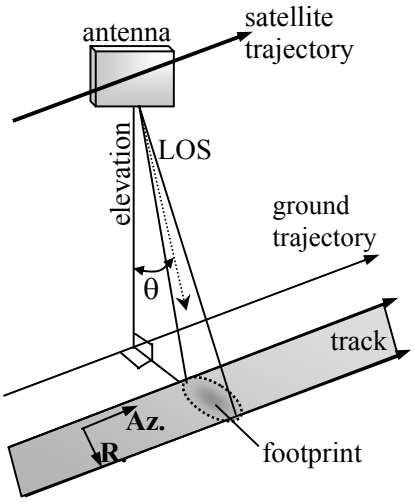

Figure 2.1. Simplified imaging geometry of side-looking radar. The European Remote Sensing (ERS) satellites orbit the earth in trajectories N12°W and S12°W, they image the earth from an elevation of ~780 km, at an incidence angle, θ, of ~23° between the Line Of Site (LOS) and the vertical. The radar footprint is ~100 km in the range direction (R.) and ~5 km in the azimuth direction (Az.). The resulting tracks are ~100 km wide and the frames within them each cover an area of approximately 100x100 km. ERS frames are usually imaged once every orbit repetition period of 35 days. Compiled from Gabriel and Goldstein (1988); Curlander and McDonough (1991); Rosen et al. (1996).

In conventional radar imaging, the target is illuminated with electromagnetic waves of microwave frequency and the reflected signal is used to deduce information about the target. SAR (Synthetic Aperture Radar) combines signal-processing techniques with satellite orbit information in order to improve radar image resolution from its natural resolution of approximately 5-10 km, to tens of meters. Fine resolution in the range direction (perpendicular to the satellites track, Figure 2.1) is achieved by using a radar signal of high frequency that improves the differentiation of radar echoes from closely spaced targets (e.g. 5.3 GHz used in ERS-1,2). Improving the resolution in the azimuth direction (along-track, Figure 2.1) relies on the synthetic aperture provided by a moving antenna. The moving antenna enables each particular point target on the ground to contribute to successively recorded radar echoes (i.e. the radar footprints of successive pulses overlap). These echoes are combined to synthesize a larger antenna aperture (~5 km long) and thus achieve much improved resolution with respect to a fixed antenna Radar (Curlander and McDonough, 1991; Burgmann et al., 2000). The resulting SAR image is a map in which each 20x4 m pixel records the amplitude and phase of the signal return from targets within the imaging area. The amplitude in SAR images is a measure of ground reflectivity and the phase is a measure of both the distance from the Radar to the target and the phase shift of the waves reflected from the ground.

InSAR is a method in which the phase information of two SAR images acquired at different times and/or from slightly different viewing position is used to determine the phase difference between each pair of corresponding image points. In this way the phase difference between two SAR images spanning a short time interval and acquired from

slightly different viewing direction measures surface topography (Figure 2.2.a), yielding a Digital Elevation Model (DEM). Alternatively, phase differences between two SAR images taken at different times from the same viewing direction (Figure 2.2.b) correspond to changes in satellite-to-ground range (Goldstein and Zebker, 1987; Massonnet et al., 1993). In this case, the resulting phase difference map is called a change interferogram, and displays fringes of equal surface displacements in the satellites Line Of Sight (LOS). In fact, the phase differences between any two SAR images consist of phase contribution from five sources: (a) surface displacement that occurred during the time between acquisitions, (b) earth curvature, (c) orbit error, (d) topography, (e) variations in signal delay within the propagation medium (i.e. atmospheric delay). To successfully image surface displacement it is necessary to subtract the other phase contributions from the interferogram or to identify their contribution and differentiate it from surface displacement.

Precise orbital information (Scharroo and Visser, 1998) is used to remove the largest phase signal due to Earth curvature. These orbits have radial accuracy of 50 mm and crossover repeatability within 70 mm, giving an overall baseline (distance vector between the reference and repeat satellites) accuracy better than 70 mm. As repeat orbits are usually not parallel, the baseline must be calculated for every point in both azimuth and range within an image frame (Gabriel and Goldstein, 1988). An error in calculating these changes in baseline (i.e. the convergence or divergence of the orbital trajectories) can create along-track fringes, and require adjusting the repeat orbital trajectory according to the references (this procedure, called “orbital tuning”, is detailed in subsection 2.1.3).

To remove the topographic phase contribution, a DEM is subtracted from the interferogram. This is done either by projecting a previously existing independent DEM into the radar coordinates or by using InSAR to generate a DEM of the imaged area. The first method, known as the two-pass method (Massonnet et al., 1993), requires at least one three-dimensional ground control point and precise orbit data. In the second method, the three- or four-pass method (Gabriel et al., 1989; Zebker et al., 1994b), the residual phase from a pair of SAR images with negligible phase contribution from deformation (preferably a tandem ERS-1 to ERS-2 pair with one day interval) is used to remove the

topographic phase from interferograms. Combining the above methods is possible when both types of DEM are available, as described in the InSAR processing subsection (2.1.3).

Variations in signal delay within the propagation medium can result from local tropospheric turbulences, from regional ionospheric perturbations and from differences in the hydrostatic component of the troposphere (Massonnet and Feigl, 1995a; Rosen et al., 1996; Zebker et al., 1997; Hanssen, 2001). Because we cannot yet remove these atmospheric signals from interferograms, it is important to recognize them as atmospheric artifacts so that they are not confused with deformation. Determination of InSAR artifacts is elaborated in the following section.

2.1.2 InSAR imaging geometry, error sources and limitations

In this section InSAR imaging geometry is explained and its inherent error sources, artifacts and limitations are described.

First, we describe the equations needed to calculate ground displacement from InSAR phase measurements (following Zebker et al., 1994b). Consider two SAR satellites imaging the same target on the ground at two incidents from two positions (i.e. reference and repeat, Figure 2.2.a). The measured phase at each point in each of the image consists of a "propagation term" proportional to the round-trip distance traveled and a "scattering term" reflecting the interaction of the wave with the ground. Assuming that no deformation occurred during the period between the two acquisitions (Figure 2.2.a) and that the backscatter of corresponding resolution elements on the ground does not change, then the phase difference between the images depends solely on the imaging geometry.

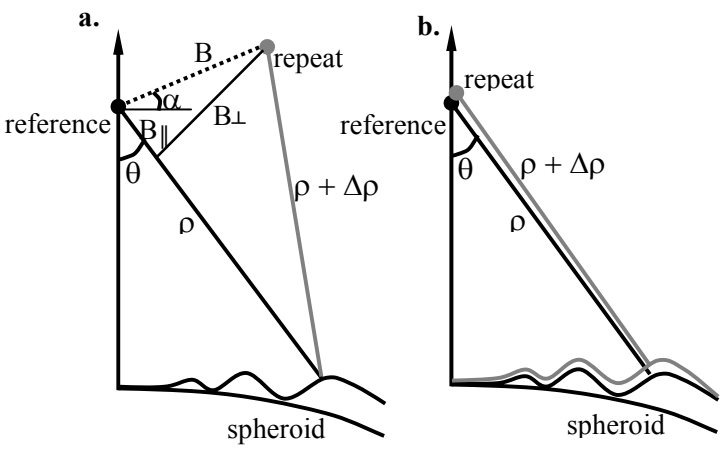

Figure 2.2. InSAR imaging geometry. B is the baseline vector between the reference and repeat satellites. $B_{\parallel}$ and $B_{\perp}$ are the components of baseline parallel and perpendicular to the line of sight. ρ is the range from sensor to ground target, θ is the angle of incidence. In case (a) the phase difference is due to topography, earth curvature and possibly atmospheric delay. In case (b) a surface deformation component is added and the topographic component is minimized due to a short baseline.

Taking the two path lengths to be ρ and ρ+Δρ, the measured phase difference ϕ is:

$$\phi = \frac{4\pi}{\lambda}\Delta\rho \tag{1}$$

The phase difference therefore equals 2π times the round trip distance difference in wavelengths. Using the law of cosines we can express Δρ in terms of imaging geometry:

$$(\rho + \Delta\rho)^2 = \rho^2 + B^2 - 2\rho B\sin(\theta - \alpha) \tag{2}$$

where the baseline is B, the satellite to target range is ρ, the look angle is θ, and the angle of the baseline with respect to horizontal at the radar is α (Figure 2.2). Neglecting terms of order $(\Delta\rho)^2$ yields:

$$\Delta\rho \approx B\sin(\theta - \alpha) + \frac{B^2}{2\rho} \tag{3}$$

Following Zebker and Goldstein (1986) in their analysis of InSAR topographic mapping, the parallel-ray approximation ($B \ll \rho$) implies that the second term on the right-hand side of (3) can be ignored. Based on the geometric relation defining the baseline component parallel to the look direction, $B_{\parallel} = B\sin(\theta - \alpha)$, we deduct that Δρ is approximately equal to $B_{\parallel}$, and therefore the topographic contribution to phase difference (eq.1) is:

$$\phi \approx \frac{4\pi}{\lambda} B_{\parallel} \tag{4}$$

Now consider a second pair of SAR images of the same target but with surface deformation occurring during the time period between the two acquisitions (Figure 2.2.b). Here in addition to the phase dependence on topography there is a phase change due to the radar line of sight component of the displacement Δρ. In this interferogram the phase ϕ' is given by:

$$\phi' \approx \frac{4\pi}{\lambda}\left(B'_{\parallel} + \Delta\rho\right) \tag{5}$$

If the precise orbital positions of the satellites are known and a previously determined DEM can be registered into the satellite coordinate system and correlated to the two SAR images, then the topographic phase contribution can be subtracted from the interferogram (Massonnet et al., 1993; Massonnet and Rabaute, 1993). Alternatively, the phase difference from the initial (deformation free) interferogram (ϕ) can be scaled by the ratio of the parallel components of the baseline and subtracted from the second interferogram (ϕ'). In

this procedure, called the four-pass method (Zebker et al., 1994; Gabriel et al., 1989), the LOS displacement $\Delta\rho$ can be obtained as follows:

$$\phi' - \frac{B'_{\parallel}}{B_{\parallel}}\phi \approx \frac{4\pi}{\lambda}\Delta\rho \tag{6}$$

As the parallel components of the baselines are a function of the look angle θ, the LOS displacement given here still depends on the illumination geometry and on the topography at each point in the image. Zebker et al. (1994b) devised an indirect approach to bypass the need for an independent DEM. By removing the phase contribution of earth's curvature, the "flattened" phase difference, ϕ_{flat}, of the interferogram is given by:

$$\phi_{flat} \approx \frac{4\pi}{\lambda}\left[B\sin(\theta-\alpha) - B\sin(\theta_0-\alpha)\right] \tag{7}$$

where θ_0 is the look angle to each point in the image assuming zero local height. The flattened interferogram phase represents topographic variation relative to a spherical surface and displacements in the LOS. Noting that the deviations of the exact θ from θ_0 are small, the right-hand side of equation (7) can be expanded, as follows:

$$\phi_{flat} \approx \frac{4\pi}{\lambda}\delta\theta B\cos(\theta_0-\alpha) \approx \frac{4\pi}{\lambda}\delta\theta B_{\perp} \tag{8}$$

where $\delta\theta = \theta - \theta_0$, and $B_{\perp}$ is the perpendicular component of the baseline assuming no topography. Thus the ratio ϕ_{flat}/ϕ'_{flat} is now in terms of θ_0 rather than θ and depends only on the viewing geometry and the baseline. Finally, the differential phase equation (6) can be written in terms of flattened phase, as follows:

$$\phi'_{flat} - \frac{B'_{\perp}}{B_{\perp}}\phi_{flat} \approx \frac{4\pi}{\lambda}\Delta\rho \tag{9}$$

With this equation it is possible to calculate the LOS displacement $\Delta\rho$ without requiring the exact values of θ, and hence the topographic information, at an intermediate step. In the final interferogram (flattened and topography-free), one cycle of phase difference (2π) corresponds to a satellite-to-target range difference of $\lambda/2$ (28 mm for the ERS satellites).

Based on the above equations it is easy to compare between the inherent sensitivities of InSAR phase measurements to displacement (in the LOS) and to topography. The

sensitivity to displacement is obtained by differentiating (5) with respect to displacement, as follows:

$$\frac{d\phi'}{d\Delta\rho} = \frac{4\pi}{\lambda} \tag{10}$$

The sensitivity to topography is obtained by differentiating (5) with respect to the topographic variation from the spheroid. Based on the equation $B_{\parallel} = B \sin(\theta - \alpha)$, and on the geometric relation $z = h - \rho \cos\theta$ in which z is topography, h the satellite altitude, and θ the exact look angle, we can derive $dz = \rho \sin\theta \, d\theta$, and obtain:

$$\frac{d\phi'}{dz} = \frac{4\pi}{\lambda} B' \cos(\theta - \alpha) \frac{d\theta}{dz} = \frac{4\pi}{\lambda} \frac{B' \cos(\theta - \alpha)}{\rho \sin\theta} \tag{11}$$

Since $B << \rho$, it can be inferred from equations (10) and (11) that InSAR phase measurements are much more sensitive to surface displacement than to surface topography. A sensitivity ratio of 1:3000 was calculated by Zebker et al. (1994) for ERS-1 interferograms of the Landers Earthquake. This ratio also represents the ratio between the accuracy of InSAR derived elevation models (10-50 m) and the accuracy of InSAR displacement maps (mm-cm) (Hanssen, 2001; Massonnet and Feigl, 1995a; Zebker et al., 1994a,b).

After discussing InSAR imaging geometry and the theoretical considerations in calculating surface deformation from phase measurements, we can examine and evaluate possible error sources and their significance for ground displacement analysis. By implementing baseline length and angle errors (δB, $\delta\alpha$) in the above displacement equations (7,9) Zebker et al. (1994b) determines that in addition to the desired term $\Delta\rho$ (the accurate LOS range change) two erroneous phase components are induced. The first component is a sinusoidal artifact across the entire displacement field caused by inaccurate estimation of the angle between the two orbits. Convergence of the orbital trajectories by less than 1 m over the entire length of the image can create series of parallel fringes across the interferogram. Removing a planar phase from the interferogram in a procedure called "orbital tuning" can usually eliminate this kind of artifact (Massonnet and Feigl, 1998). The second erroneous phase component is a residual of the topographic phase ϕ_{flat}. By expanding ϕ_{flat} about θ_0 in equation (7) Zebker et al. (1994b) shows that the displacement

contribution of the residual topographic phase ($\Delta\rho_{topo}$) is dependent on the angular deviation of the look direction due to topography ($\delta\theta = z / \rho$), as follows:

$$\Delta\rho_{topo} \approx \frac{\lambda}{4\pi}\phi_{flat}\frac{\delta B}{B} \approx \delta B \cdot \delta\theta \approx \delta B \frac{Z}{\rho} \qquad (12)$$

Thus, considering the estimated error $\delta B < 0.2$ m for ERS orbital positions by Scharoo and Visser (1998), the typical slant range of ρ = 800,000 m and assuming a realistic maximal topographic variation within a scene z_{max}= 4000 m, yields a displacement error lower than 1 mm due to baseline determination errors.

A second type of error in interferograms results from incomplete topographic phase removal, either due to errors in the topographic phase or due to inaccurate alignment between the interferogram and the topographic phase (Massonnet and Feigl, 1998). In this case, the induced artifacts are proportional to the topographic relief and to the perpendicular baseline $B_\perp$. These topographic artifacts are described using the notion of altitude of ambiguity h_a (Massonnet and Rabaute, 1993), which is the topographic relief capable of inducing a phase difference of 2π (one fringe) in an interferogram:

$$h_a = \frac{\rho\lambda \sin\theta_0}{2B_\perp} \qquad (13)$$

Massonnet and Feigl (1995a) show that the number of "topographic" fringes induced by an inaccurate DEM equals to the DEM elevation error divided by the altitude of ambiguity h_a. For example, a 30 m error in a DEM used to remove the topographic phase from interferograms with perpendicular baselines ranging between 5 m and 200 m ($1900 > h_a > 50$ m) will induce a range change of 0.5-17 mm, respectively. In any case, these artifacts are easily discriminated from phase changes induced by surface displacement by comparing their magnitude in different interferograms with different perpendicular baseline, and by correlating their location with topographic features (Massonnet and Feigl, 1995a). It is important to note that unlike topographic artifacts, phase changes induced by deformation are not proportional to the baseline and should appear similar in all interferograms spanning the same time period.

An additional error source is the variation of signal delay within the propagation medium due to atmospheric phenomena. As we do not yet have the knowledge to remove these phase signals it is important to recognize atmospheric artifacts so they are not

confused with deformation. Short-wavelength atmospheric artifacts (which could be confused with small-scale tectonic deformations) typically have length scales on the order of 5–10 km and induce a phase change between 1/6 and 1/2 a fringe, equivalent to a range increase of 5-15 mm (Massonnet and Feigl, 1995a; Hanssen, 2001). Regional atmospheric effects corresponding to long-wavelength, ionospheric perturbations and to differences in the hydrostatic component of the troposphere manifest themselves as a planar phase trend in an interferogram (Tarayre and Massonnet, 1996). This phase trend can be removed in a procedure similar to "orbital tuning" (see 2.1.3). A more problematic type of atmospheric artifact can result from vertical stratification of the lower atmosphere in regions with significant relief variations (Hanssen, 2001). In such a case the average atmospheric delay is dependent of the topographic altitude of each target cell on the ground, yielding a phase change correlative to topographic features but independent of the baseline. These atmospheric artifacts can be confused with deformation that correlates with topographic features. As all atmospheric artifacts result from the atmospheric conditions at the acquisition time of one of the SAR images used to construct the "corrupted" interferogram, the artifacts should appear similar in all interferograms constructed from that image. Thus by comparing several interferograms of the study area during the study period, it is usually easy to identify the "corrupted" image and avoid any confusion with phase changes induced by deformation (Massonnet and Feigl, 1995a).

The applicability of InSAR for measuring geophysical phenomena is limited by SAR imaging geometry and orbital repetition rate. As InSAR interpretation depends on identifying a fringe pattern consisting of several pixels, measurements are meaningless on a single pixel scale (~20 m for ERS-1,2) and on scales larger than an interferogram (~100 km for ERS-1,2). The orbit repetition interval (35 days for ERS-1,2) limits InSAR applicability in measuring reversal phenomena such as tidal loading. Even within the above physical limitations, SAR interferometry only works under coherent conditions, where the received reflections are correlated between two SAR images. In order to avoid random phase contribution, elementary targets must remain stable and contribute the same way to both images used in constructing an interferogram. Loss of coherence and destruction of the organized fringe pattern is a phenomenon known as "decorrelation". The two largest decorrelation sources that are non-reversible (i.e. that can not be reduced by

filtering) are related to the phase gradient and the temporal variation in the physical distribution of elementary scatterers on the ground (Hanssen, 2001). Steep spatial gradients of range change (>10^{-3} or 1 mm per 1 m) reduce interferometric coherence and cause decorrelation of interferograms. This limit implies that displacements that induce a phase change higher than a significant fraction of fringe within one pixel (e.g. fault rupture and catastrophic volcanic eruption) do not form interpretable fringe patterns in interferograms. Orbit inaccuracies and long wavelength atmospheric gradients may obscure subtle large-scale deformation patterns, thus imposing a low spatial gradient limit of 10^{-7} (1 cm per 100 km). Temporal decorrelation poses a major limitation for the application of InSAR in large parts of the world when using long time intervals between the SAR images. For temporal decorrelation to occur, the incoherent sum of variable scatterers within a pixel should be a significant fraction of the coherent sum of stable scatterers. Weathering, vegetation and anthropogenic activity are common causes for temporal decorrelation (Gabriel et al., 1989; Massonnet and Feigl, 1998; Hanssen, 2001). Finally, the thermal noise of the ERS Radar imposes an additional limit on applying InSAR to measure small magnitude range changes (i.e. the expected thermal noise level of 1 mm; Hanssen, 2001). This last condition implies an upper limit of phase accuracy. Massonnet and Feigl (1998) and Massonnet et al. (1997) estimate the natural noise levels in interferograms to be ~ 2 mm, thus InSAR is applicable for measuring LOS displacement larger than ~2 mm. The limitations on InSAR are summarized in Table 2.1.

Table 2.1. InSAR limiting conditions.

Limit	Explanation	Acceptable range
High spatial gradient	Destruction of continuous phase pattern – decorrelation	< 10^{-3}
Low spatial gradient	Orbital inaccuracies and atmospheric gradients	> 10^{-7}
Maximum extent	Swath width	< 100 km
Minimum extent	Pixel size	> 20 m
Minimum magnitude	Noise level	> 2 mm

In addition to the above limits on InSAR applicability, it is important to note that InSAR allows measuring a change in range along the look direction (LOS) but it does not provide the full three-dimensional displacement vector. For instance, one fringe in an interferogram constructed from ERS data (~28 mm of LOS range change) could be interpreted as ~31 mm of pure vertical displacement ($28/\cos\theta$, where θ is the incidence angle), ~74 mm of eastward displacement ($28/(\sin\theta \cdot \cos\beta)$, where β is the angle between the satellite's ground trajectory and the north), or ~345 mm of horizontal northward displacement ($28/(\sin\theta \cdot \sin\beta)$). To establish geographic components of a displacement vector, we can combine information from interferograms of both ascending (trajectory N12˚W) and descending (S12˚W) satellite orbit tracks, integrate data from other geodetic sources (such as GPS), or constrain the deformational components using geologic knowledge.

2.1.3 InSAR processing

SAR data for this study were collected by the European Space Agency Remote Sensing Satellites ERS-1, which imaged the area between April 1992 and October 1997, and ERS-2, which has been imaging the area since July 1995. During the overlapping period (1995-1997), the two satellites performed tandem missions, at 1-day intervals.

The raw SAR data are processed using a JPL-heritage SAR processor. The output signal is a measure of the complex backscatter of a patch on the ground delayed by the travel time of the Radar waves from sensor to target and back (Curlander and McDonough, 1991). Following Scripps Institution of Oceanography InSAR processing system (SIOSAR), we first focus the SAR data by maximizing the spectral overlap in azimuth direction. This is obtained by calculating the average mean doppler center frequency of the images that will be combined into interferograms, and processing each of the SAR images using that value. Then, the focused SAR images must be matched to a sub-pixel level. This procedure consists of two steps: coarse and fine coregistration. In the first step, the offsets between each "slave" image and one selected "master" image are approximated either by comparing coordinates of common points in the image (i.e. by visual inspection) or according to precise orbit information of both satellites. Once the relative offsets between the SAR images are estimated within tens of meters in range and azimuth, the fine (sub-pixel) registration can be performed. Coherent registration techniques apply the full complex

(amplitude and phase) data to perform a complex cross correlation and yield shift and stretch parameters. After matching the SAR images, interferograms (phase and amplitude) are calculated by multiplying each complex pixel in one image by the complex conjugate of the matching pixel in the other image.

Precise orbital information (Scharroo and Visser, 1998) with respect to the WGS84 and EGM96 ellipsoids is used to remove the largest phase signal due to Earth curvature. A low-resolution digital elevation model (Hall, 1993) is projected into the Radar coordinates and removed from the full-resolution interferogram. The vertical and horizontal accuracies of this DEM were tested by Hall et al. (1999), and were found to be 10-30 m and 20-50 m respectively. In addition to removing the crude DEM, the residual phase from a suitable tandem ERS-1 to ERS-2 pair is unwrapped and added back to the crude topographic phase model to form a full-resolution topography model needed for isolating the phase signal due to ground motion. This hybrid approach of topographic phase construction retains the long-wavelength accuracy of the two- pass method (Massonnet and Feigl, 1998) and the full topographic resolution of the four-pass method (Zebker et al., 1994a).

The final interferogram may display residual orbital contribution due to inaccuracies in calculating the baseline between the SAR images (see previous subsection). "Orbital tuning" is a procedure aimed to eliminate these orbital artifacts by attribution of the residual fringes in the interferogram to the repeat orbit. Assuming that the baseline error is linear (i.e. represents convergence or divergence), calculation of the number of residual fringes per pixel in both the range and azimuth direction enables the fine-tuning of the slave orbit. This procedure is similar to that suggested by Massonnet and Feigl (1998).

2.2 Tectonic interpretation tools

2.2.1 Synthetic interferogram

Synthetic interferograms are interferometric phase change models calculated based on a surface displacement field induced by a fault dislocation model. Assuming the displacement field is induced by a rectangular fault buried in an elastic medium, the synthetic interferogram enables the determination of the fault and slip parameters. Following Feigl et al. (1995) we use all available data on fault parameters (e.g. fault location, dimensions, strike, dip and estimated slip) to calculate a model displacement field

using the dislocation formulation of Okada (1985). Then, the surface displacements are translated to "synthetic" LOS range changes based on orbit trajectory and imaging geometry. Analysis of both ascending (LOS azimuth N78˚E) and descending (LOS azimuth N78˚W) interferograms assists in determination of the geographic components of the displacement in interferograms. Finally, in order to minimize the difference between the observed range changes and the modeled ones we use forward modeling in which fault model parameters are adjusted until the best solution is obtained.

2.2.2 Fault dislocation analysis and static stress transfer

Over the past 20 years, and especially since the 1992 Landers earthquake, much effort has been focused on understanding if and how earthquakes modify the behavior of nearby subsequent seismicity (e.g. Scholz, 1990; Savage, 1980 and references therein). There is a growing consensus that earthquakes may trigger one another through changes in the regional stress field; this effect is called earthquake stress transfer. Most stress transfer studies start with similar basic assumptions. Given a slip distribution for the mainshock of interest, the theory of elastic deformation from dislocations in a half-space (Okada, 1992) is used to compute coseismic stress increment tensors at specified locations. These tensors are then decomposed into fault-normal stress and fault-parallel shear stress.

The most commonly used stress formulation is the static Coulomb Failure Stress (e.g. Jaeger and Cook, 1979; Scholz, 1990). The coseismic change in CFS is given by

$$\Delta CFS = \Delta\sigma_s + \mu(\Delta\sigma_n + \Delta p) \; ; \qquad (14)$$

where $\Delta\sigma_s$ is the coseismic change in shear stress in the direction of fault slip, $\Delta\sigma_n$ is the change in normal stress (with tension positive), Δp is the change in pore-fluid pressure, and μ is an assumed "coefficient of internal friction". The ΔCFS criterion provides a measure of the proximity of a fault to failure and has been used by numerous authors to study the distribution of aftershocks after an earthquake, and to explore earthquake-induced static stress changes (e.g. Stein and Lisowski, 1983; Oppenheimer et al., 1988; Stein, 1999). In the most general case, in order to calculate the change in CFS (ΔCFS) at a location in the medium caused by an earthquake, it is necessary to know the deviatoric stress tensor before the earthquake and after the earthquake. It is possible to calculate the changes in static stress caused by the earthquake from a dislocation model, given a known "regional" state of stress before the earthquake. Alternatively, if a slip direction (rake) can be assumed

for specified fault planes (e.g. based on independent geologic date), then the regional field can be dispensed with entirely, and the changes in static stress are sufficient to calculate whether failure on these planes has been "encouraged" or "discouraged".

In our work, basic fault dislocation analysis was performed on the “GNStress” program prior to constructing synthetic interferograms. This program, written by Russell Robinson of the Institute of Geological & Nuclear Sciences, New Zealand, is used to model stresses induced by faulting and earthquakes. The program uses a code based on Okada (1985, 1992) to solve stresses induced by a dislocation in a 3-dimensional elastic half space. Given user-defined dislocation (faults properties and slip parameters) GNStress displays the induced change in the stress field expressed as ΔCFS and the displacement field at a chosen reference plane (e.g. at the surface). Results can be map view, cross-section, or projected onto a specified fault plane. GNStress was used to analyze the surface displacement field induced by model fault dislocations and to evaluate the possibility of interaction between these faults and earthquakes that occurred during the study period in the vicinity of the observed surface deformation.

2.3 Arava Valley interferometry

2.3.1 InSAR data processed and interferogram inventory

The AV is covered by six frames of three ERS tracks (Figure 2.3), each frame is imaged by ERS-1 and ERS-2 satellites every 35 days (the orbit repetition interval of each satellite). To achieve a complete analysis of the surface deformation, all available images of the AV were considered. A total of 83 interferograms spanning periods of 2-74 months between 1995 and 2002 were constructed from image pairs with perpendicular baseline lower than 150 m (Table 2.2); using this small baseline is aimed to minimize the topographic phase contribution and the degradation of pixel correlation. In order to apply the hybrid approach for obtaining topography-free interferograms, topographic phases were constructed for the processed frames. Image pairs for topographic phase were chosen for their minimal time span and wide range of perpendicular baseline (Table 2.3).

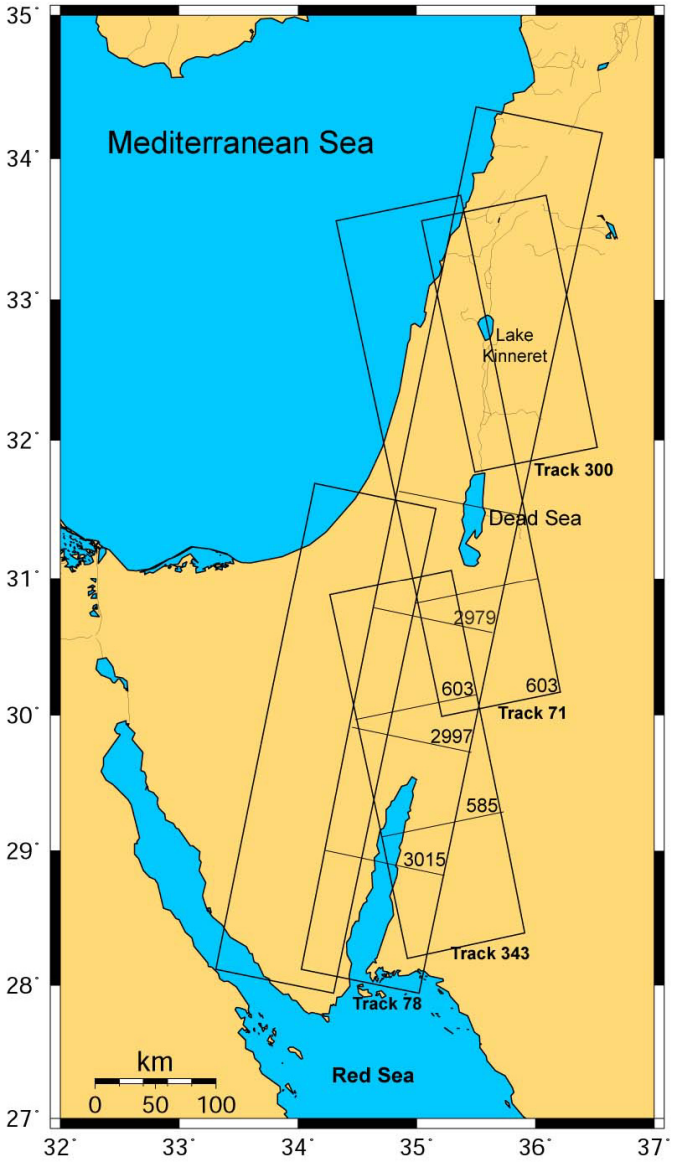

Figure 2.3. ERS coverage of the Arava Valley. Images of the following frames were processed: frame 603 of track 71, frames 603 and 585 of track 343, frames 2979, 2997 and 3015 of track 78. The combination of ascending (343, 71) and descending (78) tracks helps to constrain geographic components of LOS displacements.

Table 2.2. Interferograms processed for the analysis of surface deformation along the AV. Interferograms are referred to by the orbit numbers of their reference and repeat orbits. "Baseline perp." is the perpendicular baseline between the two orbits forming the interferogram (continued on the following page).

Interferogram (reference_repeat)	Time span (reference_repeat)	Baseline perp. (m)	Interferogram (reference_repeat)	Time span (reference_repeat)	Baseline perp. (m)
Frame 585, Track 343:			Frame 603, Track 343:		
19369_21874	29/3/95 – 20/9/95	10	19369_21373	29/3/95 – 15/8/95	90
19369_22876	29/3/95 – 29/11/95	35	19369_21874	29/3/95 – 20/9/95	2
19369_03203	29/3/95 – 30/11/95	40	19369_03203	29/3/95 – 30/11/95	30
19369_25381	29/3/95 – 22/5/96	150	19369_19736	29/3/95 – 28/1/99	5
19369_10217	29/3/95 – 3/4/97	6	19870_05708	3/5/95 – 23/5/96	80
19369_15728	29/3/95 – 23/4/98	105	19870_28754	3/5/95 – 19/10/00	25

Interferogram (reference_repeat)	Time span (reference_repeat)	Baseline perp. (m)	Interferogram (reference_repeat)	Time span (reference_repeat)	Baseline perp. (m)
Frame 585, Track 343 (continued):			Frame 603, Track 343 (continued):		
19369_19736	29/3/95 – 28/1/99	10	21373_12221	15/8/95 – 21/8/97	25
19870_05708	3/5/95 – 23/5/96	85	21373_15728	15/8/95 – 23/4/98	35
05708_28754	23/5/96– 19/10/00	45	01700_15728	16/8/95 – 23/4/98	45
21874_22876	20/9/95 – 29/11/95	30	01700_25381	16/8/95 – 22/5/96	30
21874_03203	20/9/95 – 30/11/95	30	21874_10217	20/9/95 – 3/4/97	15
21874_10217	20/9/95 – 3/4/97	25	21874_19736	20/9/95 – 28/1/99	8
21874_19736	20/9/95 – 28/1/99	15	02201_10718	21/9/95 – 8/5/97	55
02201_10718	21/9/95 – 8/5/97	60	02201_19235	21/9/95 – 24/12/98	6
02201_19235	21/9/95 – 24/12/98	5	22375_08213	25/10/95 – 14/11/96	8
22375_08213	25/10/95 – 14/11/96	1	22375_34766	25/10/95 – 13/12/01	110
22375_34766	25/10/95 – 13/12/01	130	02702_08213	26/10/95 – 14/11/96	20
02702_08213	26/10/95 – 14/11/96	15	02702_34766	26/10/95 – 13/12/01	120
22876_25381	29/11/95 – 22/5/96	110	22876_10217	29/11/95 – 3/4/97	10
22876_10217	29/11/95 – 3/4/97	5	22876_19736	29/11/95 – 28/1/99	20
22876_19736	29/11/95 – 28/1/99	15	03203_10217	30/11/95 – 3/4/97	15
03203_25381	30/11/95 – 22/5/96	120	03203_19736	30/11/95 – 28/1/99	25
03203_10217	30/11/95 – 3/4/97	10	25381_12221	22/5/96 – 21/8/97	30
03203_19736	30/11/95 – 28/1/99	20	25381_15728	22/5/96 – 23/4/98	15
25381_15728	22/5/96 – 23/4/98	15	08213_34766	14/11/96 – 13/12/01	100
08213_34766	14/11/96 – 13/12/01	130	10217_19736	3/4/97 – 28/1/99	10
10217_19736	3/4/97 – 28/1/99	15	10718_19235	8/5/97 – 24/12/98	50
10718_19235	8/5/97 – 24/12/98	50	12221_15728	21/8/97 – 23/4/98	10
Frame 3015, Track 78:			Frame 2979, Track 78:		
05443_21475	5/5/96 – 30/5/99	40	01435_09451	30/7/95 – 9/2/97	1
29992_39511	14/1/01 – 10/11/02	2	01435_22611	30/7/95 – 11/11/95	1
			03439_12958	17/12/95 – 12/10/97	7
Frame 2997, Track 78:			03439_29992	17/12/95 – 14/1/01	40
05443_19972	5/5/96 – 14/2/99	75	04732_12958	11/6/92 – 12/10/97	90
05443_21475	5/5/96 – 30/5/99	45	04732_22110	11/6/92 – 7/10/95	30
19972_21475	14/2/99 – 30/5/99	120	04732_29992	11/6/92 – 14/1/01	125
20974_29491	25/4/99 – 10/12/00	20	06445_29992	14/7/96 – 14/1/01	45
			09451_20473	9/2/97 – 21/3/97	135
Frame 603, Track 71:			10744_03439	5/8/93 – 17/12/95	35
20099_22470	19/5/95 – 7/8/99	25	10744_06445	5/8/93 – 14/7/96	50
22103_21468	6/10/95 – 29/5/99	10	10744_12958	5/8/93 – 12/10/97	25
			10744_29992	5/8/93 – 14/1/01	8
			12958_29992	12/10/97 – 14/1/01	35
			13960_20473	21/12/97 – 21/3/97	15
			21108_06445	29/7/95 – 14/7/96	140
			22110_03439	7/10/95 – 17/12/95	55
			22110_12958	7/10/95 – 12/10/97	65
			22611_09451	11/11/95 – 9/2/97	1

Table 2.3. Image pairs used in constructing topographic phases for the analysis of surface deformation along the Arava Valley.

Frame (Track)	Image pair (reference_repeat)	Time span (reference_repeat)	Perpendicular baseline (m)
585 (343)	22876_03203	29/11/95 – 30/11/95	5
	10217_10718	3/4/97 – 8/5/97	165
	25381_05708	22/5/96 – 23/5/96	95
	19235_19736	24/12/98 – 28/1/99	210
603 (343)	21874_02201	20/9/95 – 21/9/95	215
	21373_01700	16/8/95 – 17/8/95	80
	25381_05708	22/5/96 – 23/5/96	95
	22375_02702	25/10/95 – 26/10/95	5
2997 (78)	19972_21475	14/2/99 – 30/5/99	120
2979 (78)	21108_01435	29/7/95 – 30/7/95	40
	21108_22110	29/7/95 – 7/10/95	150
	22611_03439	11/11/95 – 17/12/95	140

2.3.2 Discrimination of surface deformation features from InSAR artifacts

This subsection addresses InSAR artifacts observed in AV interferograms and their discrimination from surface deformation features. The relief within the AV is very moderate and thus topographic artifacts are rare. Local topographic features within the AV may induce artifacts in interferograms with long perpendicular baseline or when the topographic contribution is not entirely removed (Figure 2.4). On the other hand, the high cliffs and deep canyons on both sides of the AV, and particularly on its eastern side, induce significant topographic artifacts (Figure 2.5). In both cases the topographic artifacts are easy to detect and discriminate from surface deformation (Figure 2.4, 2.5). Local tropospheric artifacts are not very common along the AV due to the yearlong dry weather; when encountered they form wavy range-changes with short wavelength of ~1 km (Figure 2.5). Regional atmospheric gradients may induce small range-changes with long-wavelength of 100 km scale (Hanssen, 2001) which are easily discriminated from the local (<20 km) surface deformation features observed along the AV. Decorrelation due to human activity is also rare along the AV and is limited to a few cultivated fields (Figure 2.4), a few settlements and to nature reserves (Figure 2.5). Substantial decorrelation due to surface processes occurs in the local playas and river beds along the AV and is visible in interferograms spanning long time intervals, and interferograms spanning the rare event of rain and floods which occurred in October 1997 in AV (Hydrologic Service annual report, 1997).

Figure 2.4. Strips of interferograms 21874_10217 (a) and 19369_22876 (b) of frame 585. Atmospheric artifacts of a wavy form are indicated by white arrows, and topographic artifacts along the cliffs on the eastern border of the AV are indicated by black arrows. The higher baseline of (b) accounts for the greater topographic artifacts. Also visible are local deformation features (indicated by black circles) possibly induced by human activity at Timna Mines nature reserve (perhaps subsidence over the deserted mines).

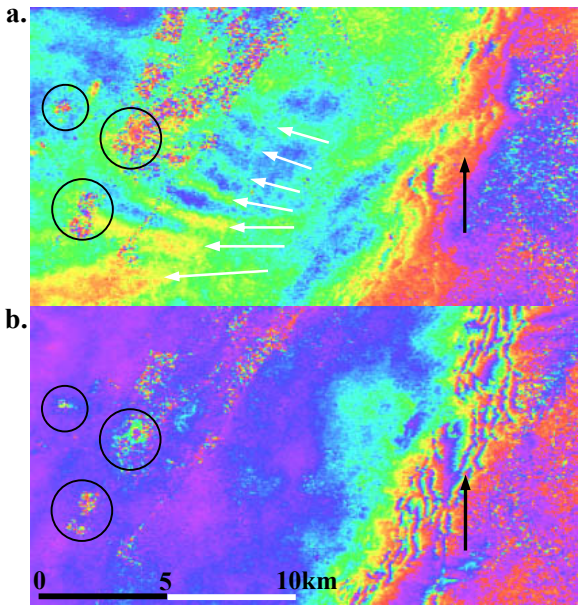

Figure 2.5. a. Part of interferogram 02702_34766 (frame 603 of track 343) showing an increase of 40 mm in the satellite-target range (Zofar subsidence, see section 3.3.1). Also apparent are topographic artifacts (indicated by white arrows) and a distinct zone of decorrelation (indicated by a black arrow). b. The same interferogram superimposed on the amplitude image of the region. c. Amplitude image showing topographic features (indicated by white arrows) and cultivated areas (indicated by a black arrow) near the village of Zofar, central Arava. The topographic artifacts in the interferogram are a result of an incomplete topographic phase removal.

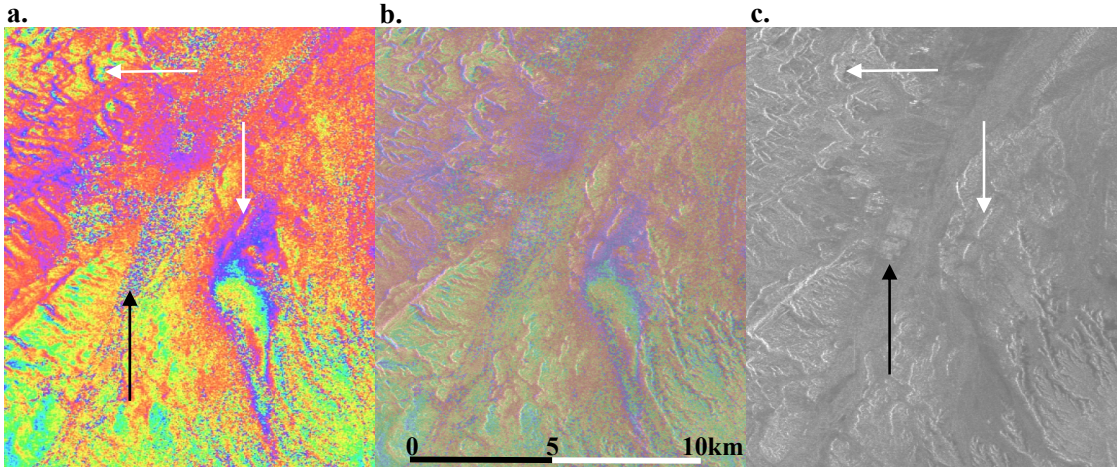

3. RESULTS

3.1 General characteristics of surface deformation along the Arava Valley

3.1.1 Magnitude, rate and distribution of surface deformation features

AV interferograms of the 1995-2001 period reveal several local, sporadic surface deformation features with dimensions <20 km. The main observed deformation features are found at fault stepover zones and their associated basins or ridges. Temporal characteristics of the detected features varied from monotonous LOS range-change during the entire study period with rates of 10-80 mm/yr, to shorter events with rates of 15-20 mm/yr.

Three regions within the AV display systematic ground displacement that could be attributed to tectonic activity (Figure 3.1). (1) East of Zofar (northern AV), an area approximately 7 km long and 3 km wide exhibits continuous subsidence during 1998-2000. (2) In Yotvata Playa (southern AV), an area about 10 km long and 5 km wide exhibits continuous ground uplift with variable rates of 10-80 mm/yr. Yotvata uplift is the largest surface deformation feature detected in this study exhibiting 135 mm of LOS range decrease between 1995 and 1999. (3) The Avrona Basin (southern AV) exhibits a complex pattern of subsidence and uplift within a 12 km long and 3 km wide region.

3.1.2 Detection of strike slip motion on Dead Sea Transform fault segments

The orientation of the DST is sub-parallel to ERS descending track trajectory (Figure 2.3), and thus it is practically impossible to detect strike slip motions along the DST in interferograms of descending ERS satellites. To evaluate the detection threshold of DST strike slip displacements in interferograms of ascending satellites, the LOS component of such motion is calculated here. Assuming that horizontal strike slip motions on AV segments of the DST are at an angle of about 25-30º from the satellites trajectory and that ERS incident angle is 23º from vertical, the LOS component of strike slip displacement parallel to the DST is:

$$\text{LOS change} = \text{Displacement} \cdot \sin(23^\circ) \cdot \sin(30^\circ) \approx 0.2 \cdot \text{Displacement}$$

This relation implies, for example, that 25 mm of strike slip surface displacement along DST parallel faults correspond to ~5 mm of LOS range-change; this value is considered by Massonet and Feigl (1998) as the detection threshold of InSAR due to background noise typically lower than 5 mm. Considering the estimated low slip rate of the Southern DST

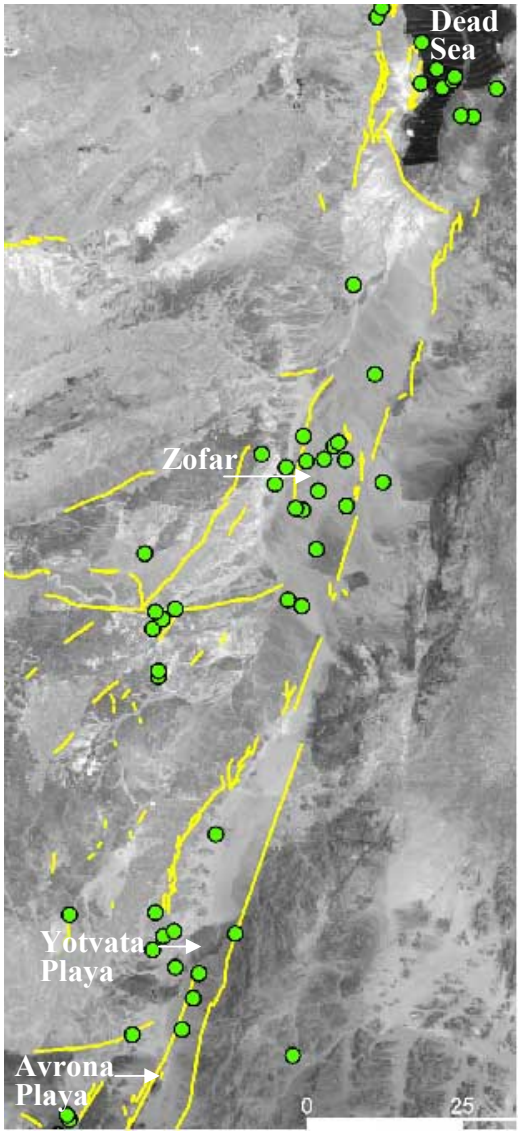

Figure 3.1. Location map for Arava Valley surface deformation features. Zofar, Yotvata and Avrona are indicated with white arrows on a satellite image of the Arava Valley (from the Dead Sea in the northeastern corner to the city of Elat near the southwestern corner). Also indicated are active faults (Bartov et al., 2002), and earthquakes of M_L>2.5 that occurred during the period of 1990-2000 (GII, 2000).

(0-5 mm/yr), strike slip motions on DST parallel faults could be detected only in interferograms with time span of at least 5 years (Figure 3.2). In contrast to this limiting threshold for strike slip motions, vertical displacements have a larger LOS effect (LOS change = cos (23º) · Vertical displacement ≈ 0.9 · Vertical displacement) and can be detected more easily by InSAR. Compared to the DST, strike-slip displacement on the San Andreas Fault and the Hayward Fault have a higher LOS component (~0.35) and higher slip rates (10-50 mm/yr), and therefore are easily monitored with InSAR (Burgmann et al., 2000; Lyons and Sandwell, 2003).

Although the expected strike slip displacements on DST major segments are below the detection threshold, such displacements may induce LOS range-changes at fault

terminations, at sub-parallel secondary faults and at stepovers. Detection of deformation features at stepovers within the AV without detection of creep on the intervening segments may be a result of these limitations and can not rule out the possibility that AV segments creep at rates lower than ~4 mm/yr.

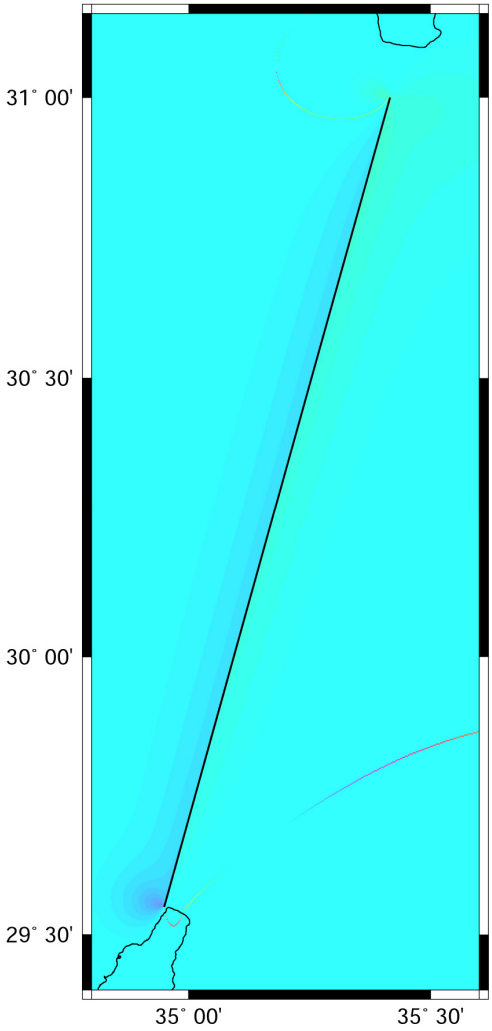

Figure 3.2. Dead Sea Transform synthetic interferogram (from the Dead Sea to the gulf of Elat). The input dislocation model is of surface displacement of 25 mm (left-lateral slip) along a continuous fault segment within the AV. The surface deformation appears as a phase change of approximately 1/6 fringe (~5 mm LOS range change) across the fault.

3.2 Surface deformation features along the Arava Valley

3.2.1 Zofar

In Zofar region, northern AV, we detected an area about 7 km long and 3 km wide that displays ~40 mm of LOS range increase during a period of 2-2.5 years. The Zofar feature is characterized by a constant and well-defined spatial extent during the entire deformation period (Figure 3.3). The feature displays steep displacement gradients along its boundaries,

particularly the southwestern boundary. In order to achieve a complete analysis of deformation magnitude, rate and temporal variations at Zofar, we processed and analyzed 35 interferograms spanning 3-74 months between March 1995 and December 2001 (Table 3.1, Figure 3.3).

Table 3.1. Interferograms and range-change at Zofar surface deformation feature.

Time span	Interferogram (reference_repeat)	LOS change (mm)	Time span	Interferogram (reference_repeat)	LOS change (mm)
Frame 603, Track 343			Frame 603, Track 343 (continued)		
29/3/95 – 15/8/95	19369_21373	0	29/11/95 – 3/4/97	22876_10217	0
29/3/95 – 20/9/95	19369_21874	0	29/11/95 – 28/1/99	22876_19736	5
29/3/95 – 30/11/95	19369_03203	0	30/11/95 – 3/4/97	03203_10217	0
29/3/95 – 28/1/99	19369_19736	5	30/11/95 – 28/1/99	03203_19736	5
3/5/95 – 23/5/96	19870_05708	0	22/5/96 – 21/8/97	25381_12221	0
3/5/95 – 19/10/00	19870_28754	40	22/5/96 – 23/4/98	25381_15728	0
15/8/95 – 21/8/97	21373_12221	0	14/11/96–13/12/01	08213_34766	40
15/8/95 – 23/4/98	21373_15728	0	3/4/97 – 28/1/99	10217_19736	5
16/8/95 – 23/4/98	01700_15728	0	8/5/97 – 24/12/98	10718_19235	5
16/8/95 – 22/5/96	01700_25381	0	21/8/97 – 23/4/98	12221_15728	0
20/9/95 – 3/4/97	21874_10217	0	Frame 2997, Track 78		
20/9/95 – 28/1/99	21874_19736	5	5/5/96 – 14/2/99	05443_19972	10
21/9/95 – 8/5/97	02201_10718	0	5/5/96 – 30/5/99	05443_21475	15
21/9/95 – 24/12/98	02201_19235	5	14/2/99 – 30/5/99	19972_21475	5
25/10/95 – 14/11/96	22375_08213	0	25/4/99 – 10/12/00	20974_29491	30
25/10/95 – 13/12/01	22375_34766	40	Frame 603, Track 71		
26/10/95 – 14/11/96	02702_08213	0	19/5/95 – 7/8/99	20099_22470	25
26/10/95 – 13/12/01	02702_34766	40	6/10/95–29/5/99	22103_21468	15

The total cumulative LOS range-change at Zofar is ~40 mm with an average rate of 15-20 mm/yr (Figure 3.4). The surface displacement initiated some time between April and December 1998, as no subsidence occurred prior to 4/1998 (e.g. interferograms 21373_15728, 25381_15728; Table 3.1). Approximately 5 mm of LOS range-increase occurred during the second half of 1998 (e.g. interferogram 10718_19235; Table 3.1), an additional 25-30 mm of range-change occurred during 1999, and 5-10 mm occurred between January and October 2000. No subsidence occurred between 10/2000-12/2001.

Figure 3.3. Zofar interferograms of ascending track 343 (frame 603) and descending track 78 (frame 2997) indicate 40 mm of LOS range increase between April 1998 and October 2000. No deformation is observed between May 1996 and April 1998 (interferogram 25381_15728) indicating that the 15mm of range change observed between May 1996 and May 1999 (05443_21475) occurred between April 1998 and May 1999. The total range change of 40 mm is observed between May 1995 and October 2001 (19870_28745), but interferogram 25381_15728 indicates that this range change occurred after April 1998. Zofar and Wadi-Musa faults are outlined red in the amplitude images.

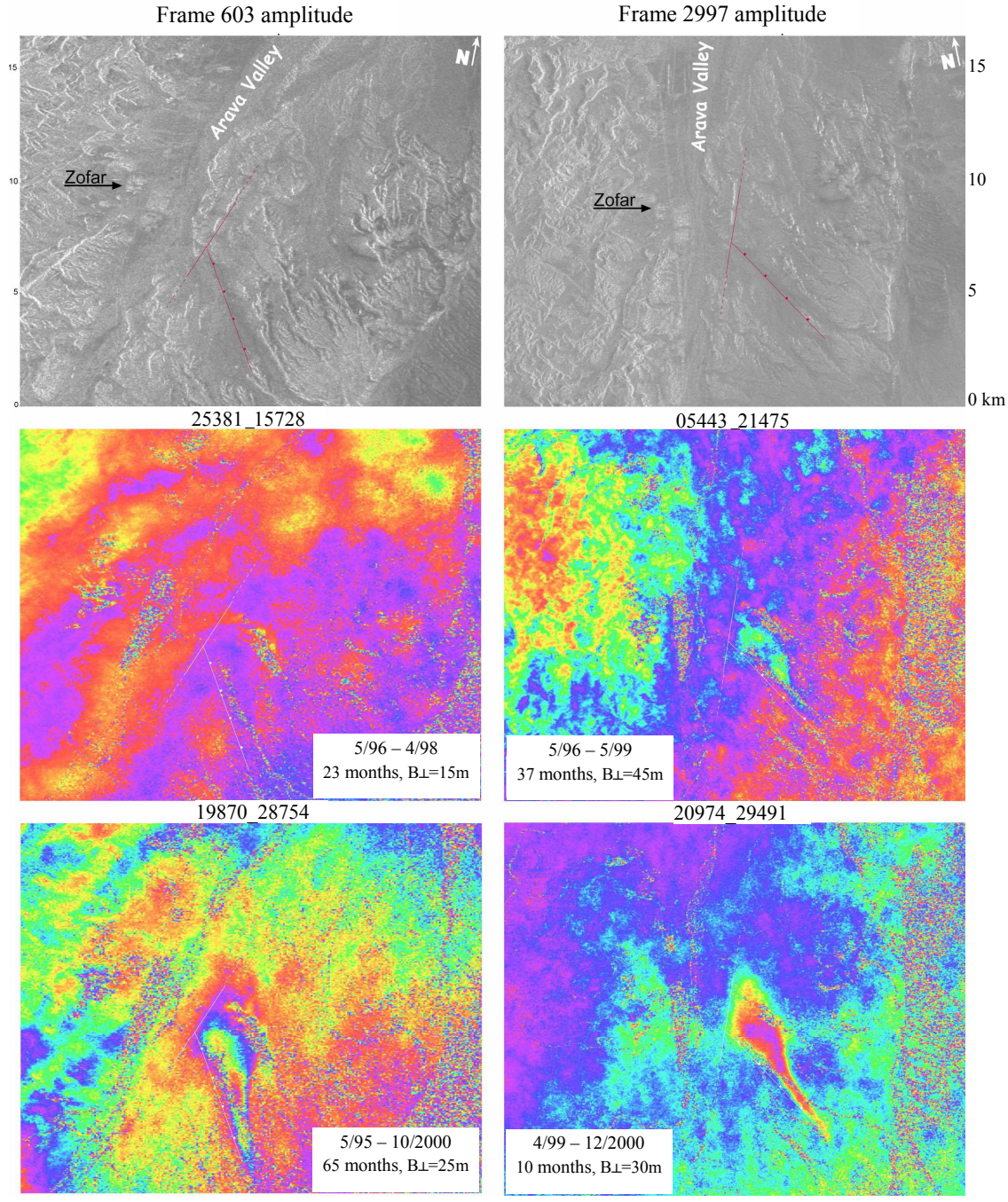

The similar range-change in interferograms of ascending and descending tracks (tracks 343 and 78 respectively; Figure 3.3) suggests predominant vertical surface displacement (subsidence) in Zofar.

Zofar subsidence is attributed to tectonic processes based on the temporal and spatial characteristics that distinguish it from topographic, atmospheric and orbital artifacts. The LOS range change is not correlated with perpendicular baseline or with topographic features indicating that it reflects surface displacement rather than topographic signature. The fact that the range change is long-lasting (not reversal) and cumulative, and that it consistently appears in all coherent interferograms supports the interpretation that the range change reflects tectonic deformation. Non-tectonic sources for the Zofar subsidence could be rejected as follows. First, surface processes, such as erosion and changes in ground cover or ground use, would generate decorrelation in the interferograms as exhibited along riverbeds and cultivated agricultural fields (Figure 2.5). Second, groundwater withdrawal and sediment compaction were shown to induce subsidence near the Dead Sea (Baer et al., 2002), and therefore water data from wells in Zofar region was analyzed (Hydrologic Service of Israel data base). During the study period (1995-2001) water level data is available only for one well near Zofar, this is the Omer 1 well, located 3-5 km NW of the deformation feature (Appendix A). Water level records of six other wells near Zofar during the five years preceding the observed subsidence do not display uniform trends (Figure 3.5), suggesting that the level changes are related to local activity (e.g. pumping) at each well. The water level in Omer 1 well displays no correlation to the behavior in Zofar feature: (1) During 1993-7, the water level rose gradually with annual fluctuations while the Zofar feature displays no surface displacement. (2) During 1998-2001, the water level displays very subtle decline while all the Zofar subsidence occurred. A similar decline in water level occurred at Omer 1 during 1996-7 prior to the subsidence at Zofar. (3) The water level changes at Omer 1 are relatively subtle (<1.5 m), and as the water level at this well is relatively deep (~12 m below the surface), the effect these changes may have on the surface is negligible. Therefore, the water level-descent between March 1998 and July 1999 is rejected as a possible mechanism for the observed surface deformation.

Figure 3.4. Zofar time series indicating LOS displacement accumulation with time. Each data point indicates the cumulative LOS displacement at the acquisition time of an ERS image used to construct Zofar interferograms. The 5 mm error bars represent the typical noise level in interferograms.

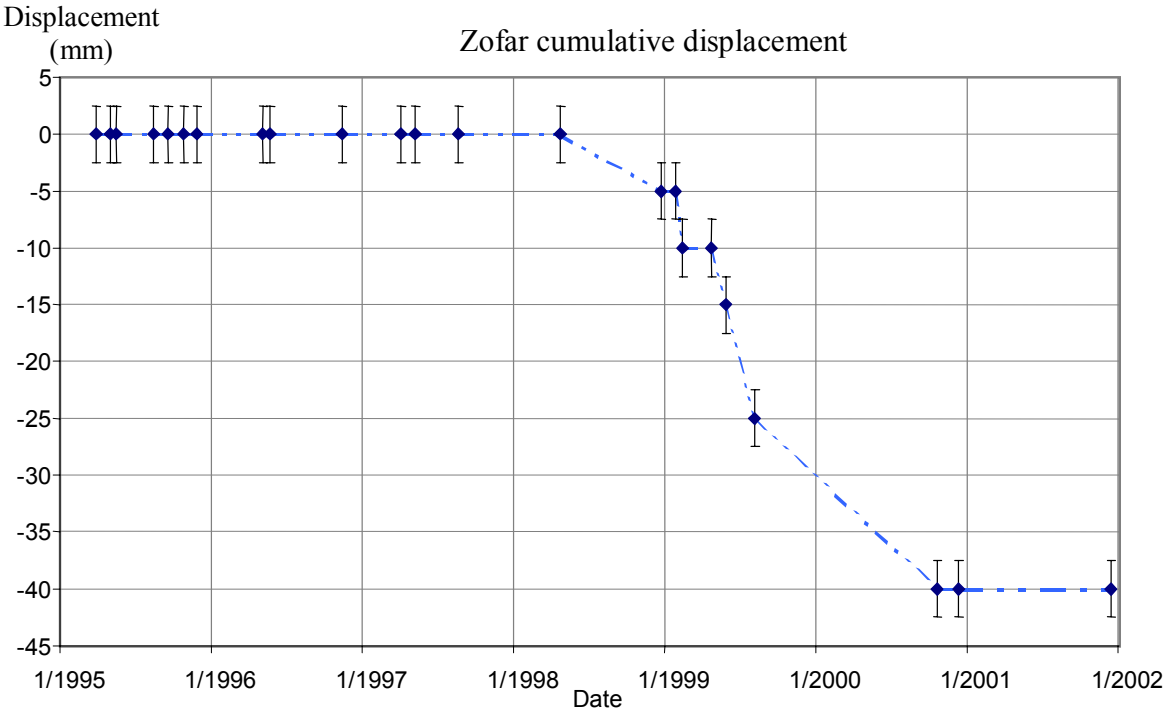

Figure 3.5. Changes in water levels at wells near Zofar relative to water levels in January 1990. During the period of 1994-1998 "Omer 1" well exhibited periodic low amplitude changes in water level (~1.5 m) while no surface displacement occurred at Zofar site (gray dashed line, smoothed version of Figure 3.4). During the first half of 1999 a very subtle linear drop occurred in "Omer 1" water level (~0.3 m) while Zofar displacement rate reached its maximum.

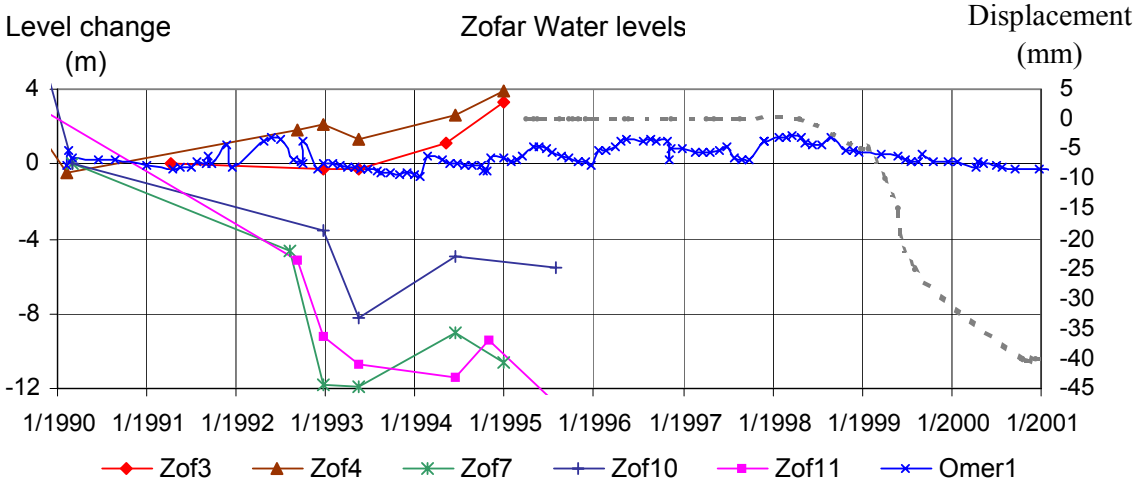

3.2.2 Yotvata

The most intense surface displacement feature detected in the present study is located SE of Yotvata, in southern AV (Figure 3.6). The Yotvata feature occupies an area about 10 km long and 5 km wide, and exhibits 135 mm of cumulative LOS range decrease during the 1995-1999 period. This feature is characterized by large continuous range decrease with maximal change near the southeastern boundary, steep displacement gradients along its western and southeastern boundaries, and well-defined spatial extent growing with time and with cumulative range decrease. These characteristics distinguish Yotvata feature from possible atmospheric and orbital artifacts and from local topographic artifacts.

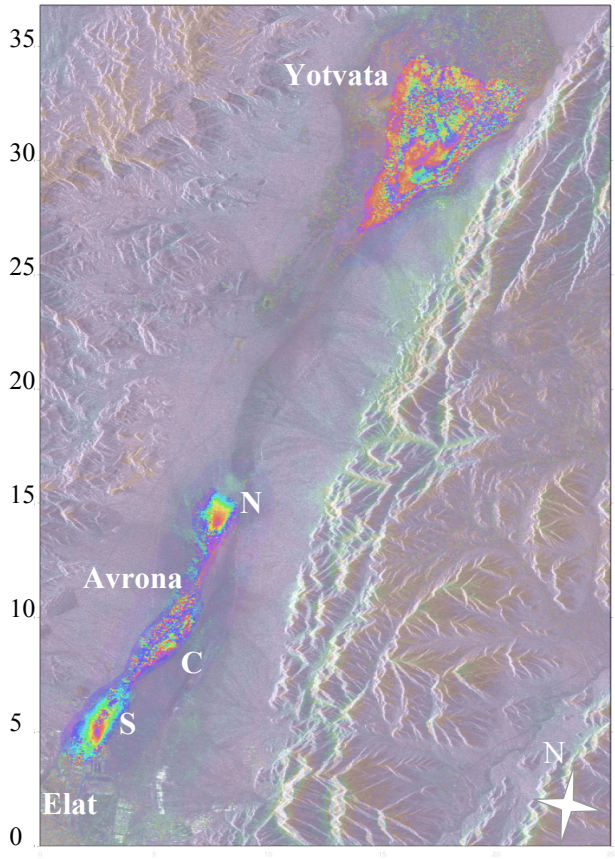

Figure 3.6. Interferogram 19369_22876 (29/3/95 - 29/11/95) superimposed on the amplitude image of southern AV (from Yotvata in the north to the Gulf of Aqaba and the city of Elat in the south). The interferogram shows 55 mm of LOS range decrease near Yotvata and a complex deformation feature at Avrona consisting of range increase at Avrona North (N) and Avrona South (S) and range decrease obscured by decorrelation in Central Avrona (C).

We processed and analyzed 32 interferograms spanning 3-74 months between March 1995 and December 2001; however, due to coherence problems, surface deformation analysis was possible only for the period of March 1995 to May 1999 (Table 3.2, Figure 3.7).

Figure 3.7. Southern AV and Yotvata interferograms (frames 603 and 2997 respectively). The interferograms display different stages of the 135 mm LOS range decrease near Yotvata (3/1995-5/1999), and indicate that most of Avrona deformation occurred between March and September 1995. Atmospheric artifacts in 19369_21874 and 21874_22876 (wavy strokes in upper-left quadrant) are attributed to conditions on 20/9/95 (orbit 21874). The regional phase change along southern AV observed in interferogram 25381_15728 is also interpreted as an atmospheric artifact based on its shape wavelength and the fact it is exclusive to interferograms constructed with orbit 15728. Scale is indicated by a grid with 5 km interval along each interferogram.

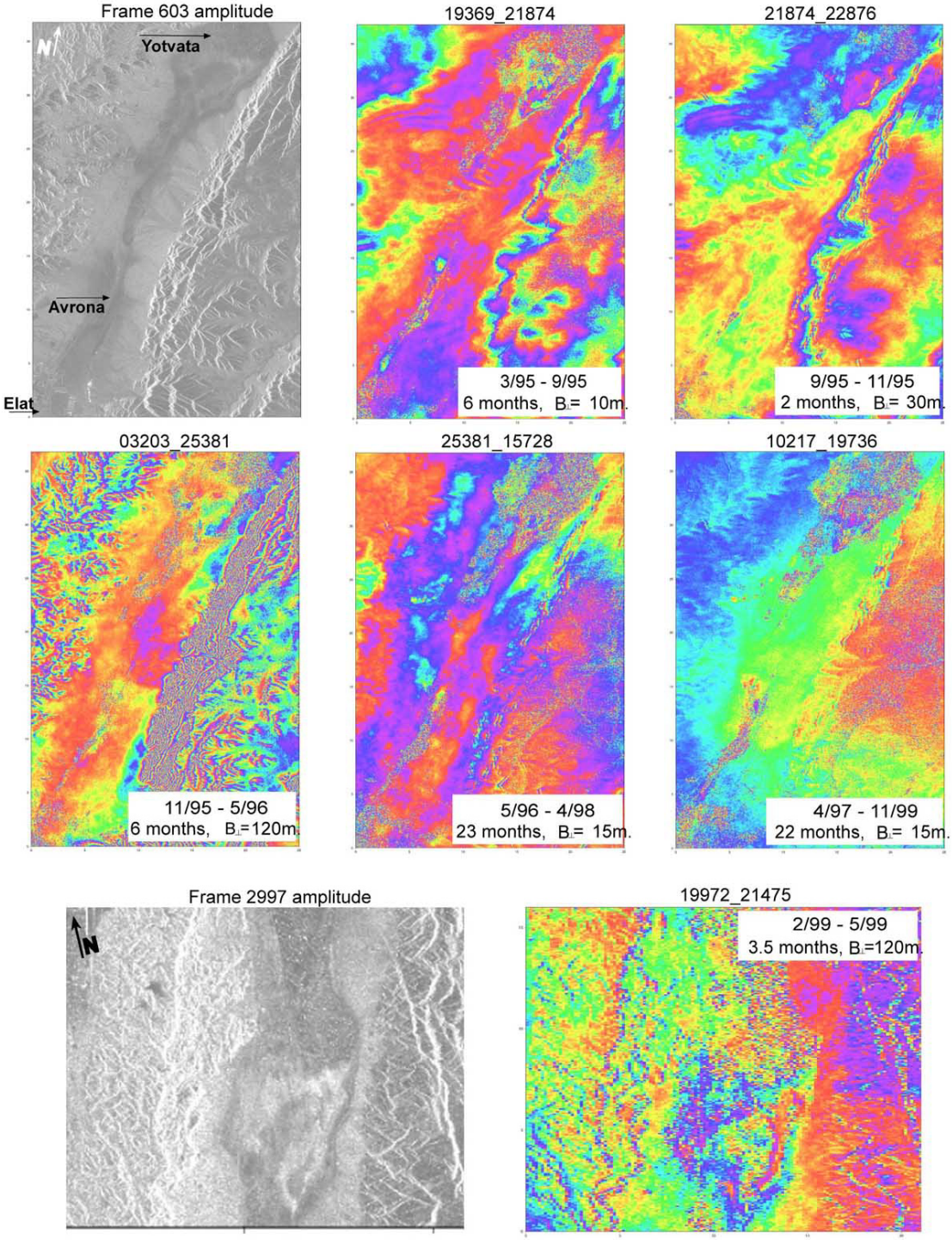

Yotvata interferograms exhibit 95 mm of LOS range decrease between March 1995 and April 1998 (interferograms 19369_21874, 21874_22876, 03203_25381, 25381_15728), and additional range decrease of 15 mm (prior to January 1999) is deduced from interferogram 10217_19736 (Figure 3.7). Interferogram 19972_21475 of frame 2997 indicates another 25 mm of range change accumulating to the total of 135 mm between March 1995 and May 1999.

Table 3.2. Interferograms and range-change at Yotvata surface deformation feature. Interferograms that could not be interpreted due to decorrelation are marked ***.

Time span	Interferogram (reference_repeat)	LOS change (mm)	Time span	Interferogram (reference_repeat)	LOS change (mm)
Frame 585, Track 343			Frame 585, Track 343 (continued)		
29/3/95 – 20/9/95	19369_21874	45	25/10/95–13/12/01	22375_34766	***
29/3/95 – 29/11/95	19369_22876	55	26/10/95–14/11/96	02702_08213	35
29/3/95 – 30/11/95	19369_03203	55	29/11/95–22/5/96	22876_25381	10
29/3/95 – 22/5/96	19369_25381	65	29/11/95 – 3/4/97	22876_10217	30
29/3/95 – 28/1/99	19369_19736	***	29/11/95–28/1/99	22876_19736	55
3/5/95 – 23/5/96	19870_05708	40	30/11/95–22/5/96	03203_25381	10
23/5/96– 19/10/00	05708_28754	***	30/11/95 – 3/4/97	03203_10217	30
20/9/95 – 29/11/95	21874_22876	10	30/11/95–28/1/99	03203_19736	55
20/9/95 – 30/11/95	21874_03203	10	22/5/96 – 23/4/98	25381_15728	30
20/9/95 – 3/4/97	21874_10217	40	14/11/96–13/12/01	08213_34766	***
20/9/95 – 28/1/99	21874_19736	***	3/4/97 – 28/1/99	10217_19736	25
21/9/95 – 8/5/97	02201_10718	45	8/5/97–24/12/98	10718_19235	15
21/9/95 – 24/12/98	02201_19235	***	Frame 2997, Track 78		
25/10/95–14/11/96	22375_08213	35	14/2/99 – 30/5/99	19972_21475	25

The continuous LOS range-change at Yotvata (Figure 3.8) occurred with rates varying from 10 mm/yr to 80 mm/yr. Interferograms with long time span (> 2 yr) and post 1999 interferograms did not yield coherent data of surface deformation in Yotvata Playa, and therefore were not included in our interpretation.

Yotvata feature is attributed here to tectonic processes based on the range change characteristics discussed above and on rejection of an aquifer related mechanism as follows. The water table measured in wells near Yotvata during 1995-2001 exhibit large annual changes probably related to seasonal changes in water influx and water pumping (Figure 3.9; Appendix A). Most wells do not exhibit a long-term change in water level, and some wells exhibit subtle drop of water level. These water level changes do not correlate with the observed monotonous uplift at Yotvata Playa; thus aquifer processes are rejected

as a possible mechanism for the observed deformation.

Figure 3.8. Yotvata time series indicating LOS displacement accumulation with time. Each data point indicates the cumulative LOS displacement at the acquisition time of an ERS image used to construct Yotvata interferograms. The 5 mm error bars represent the typical noise level in interferograms.

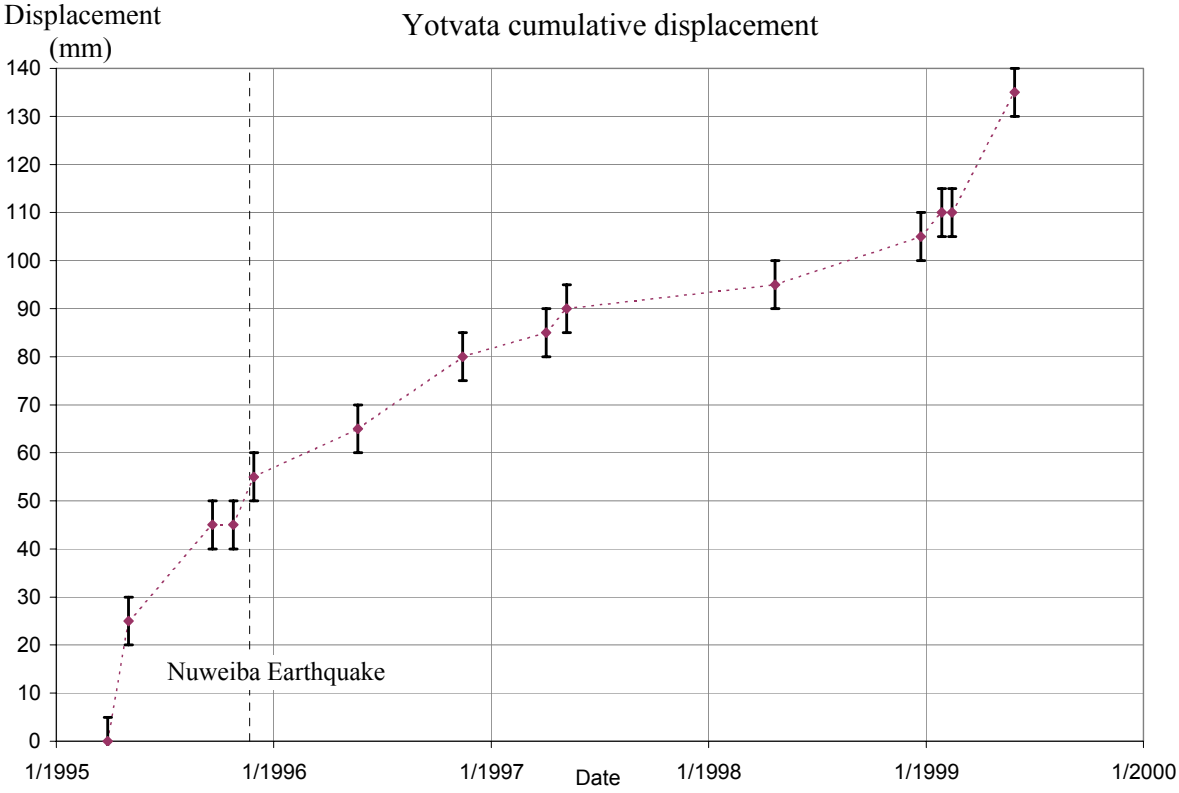

Figure 3.9. Water level data from 6 wells near Yotvata exhibit annual fluctuations without a consistent long-term level increase that could produce surface uplift. As these changes in water level do not correlate with the continuous uplift in Yotvata, they were rejected as a possible mechanism for the surface deformation. (compiled from Hydrologic Service of Israel data base)

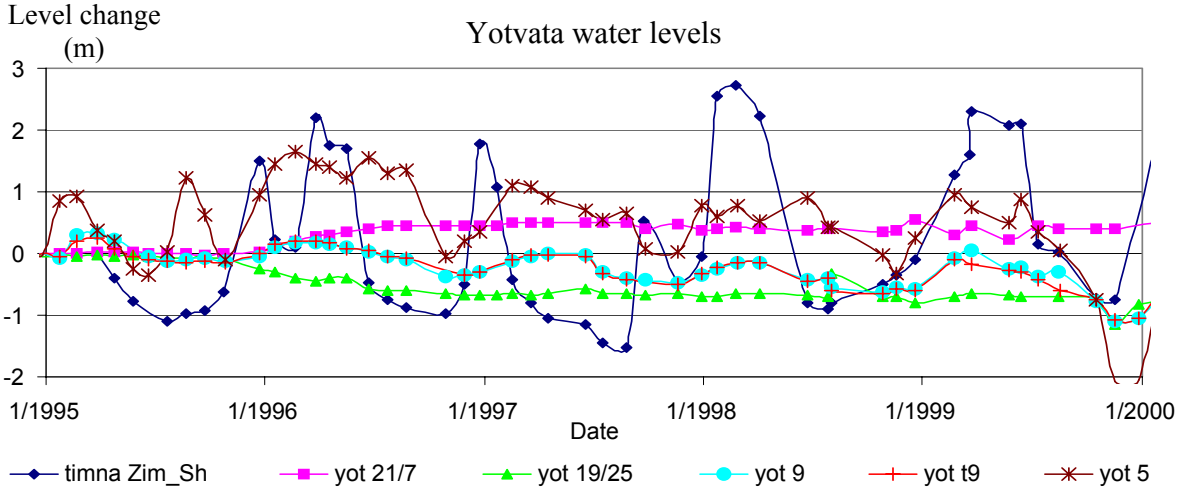

3.2.3 Avrona

The most complex pattern of surface deformation was detected at Avrona Basin, a few kilometers north of Elat. We found two zones of subsidence separated by a zone of uplift at the eastern margins of the Avrona Playa (Figure 3.6). The subsiding zones display moderate displacement gradients along their boundaries, and the central uplift feature displays non-uniform elongated displacement pattern. We analyzed the Avrona feature using the same 32 interferograms presented in the analysis of Yotvata feature (Table 3.2), and again, due to coherence problems, the surface deformation could be analyzed only for 3/1995 to 1/1999. Most of the deformation in Avrona Playa occurred between March and November 1995, and is apparent in interferograms 19369_21874 (Figure 3.7). The two subsiding zones, hereafter referred to as Avrona North and Avrona South, exhibit almost similar deformation pattern and magnitude prior to April 1997, after which Avrona North expanded and exhibited an additional 10 mm of subsidence while Avrona South exhibited 10 mm of uplift (interferogram 10217_19736, Figure 3.7). The cumulative range-change at the three Avrona features is summarized in Figure 3.10.

Unlike Yotvata and Zofar features, the Avrona deformation feature could not be fully attributed to tectonic processes, as non-tectonic mechanisms could not be rejected. During 1995-2001 water wells south of Avrona (elat1, sabcha18; Figure 3.11; Appendix A) exhibit a continuous descend in water level, while wells north of Avrona (ora6,7 and timna50; Appendix A) exhibit a continuous water level rise. These trends show limited correlation to the observed surface deformation, for example, the level drop in the southern wells partly correlate to the subsidence observed in Avrona South prior to April 1997. Thus, the contribution of water level changes to the deformation can not be rejected. A possible indication for such interaction between water level changes and tectonic deformation was found in well ora4, located ~2 km west of Central Avrona feature. This well exhibited an abrupt level drop coinciding with the Nuweiba earthquake, and then a gradual rise with a rate similar to the wells north of Avrona (Figure 3.11, Appendix A). The abrupt change in ora4 could be related to deformation associate with the Nuweiba earthquake. Thus, although no clear correlation was found between the water level changes and the observed surface deformation, one may speculate that both phenomena are related to a common tectonic cause; the nature of this relation is unknown.

In the following analysis of Avrona surface deformation, we assume that most of the surface deformation is due to tectonic activity, excluding the uplift at Avrona South after April 1997. This assumption enables the description of Avrona complex pattern of surface displacement by a relatively simple tectonic model, without incorporating an uplift phase at the subsidence site of Avrona South.

Figure 3.10. Avrona time series indicating LOS displacement accumulation with time.

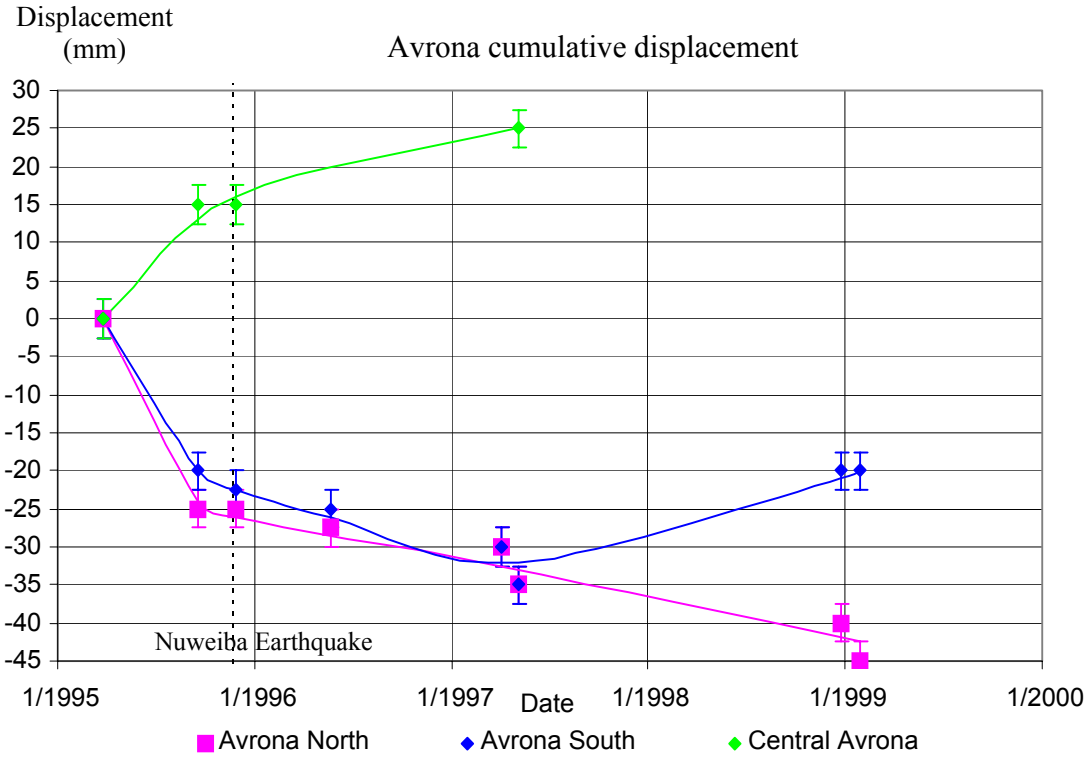

Figure 3.11. Water level data from wells near Avrona, listed from south (in warm colors) to north (cool colors). Unlike wells near Yotvata, these wells do not exhibit annual fluctuations. They display long-term trends of water level rising (in wells north of Central Avrona site, latitude 29.62ºN) and level drop (south of Central Avrona site). Well ora4 (coordinates: 29.69ºN/34.99ºE) displays an abrupt drop in water level that coincides with the occurrence of Nuweiba earthquake (22/11/95, M_W=7.2) that occurred approximately 100 km to the south (Shamir, 1996).

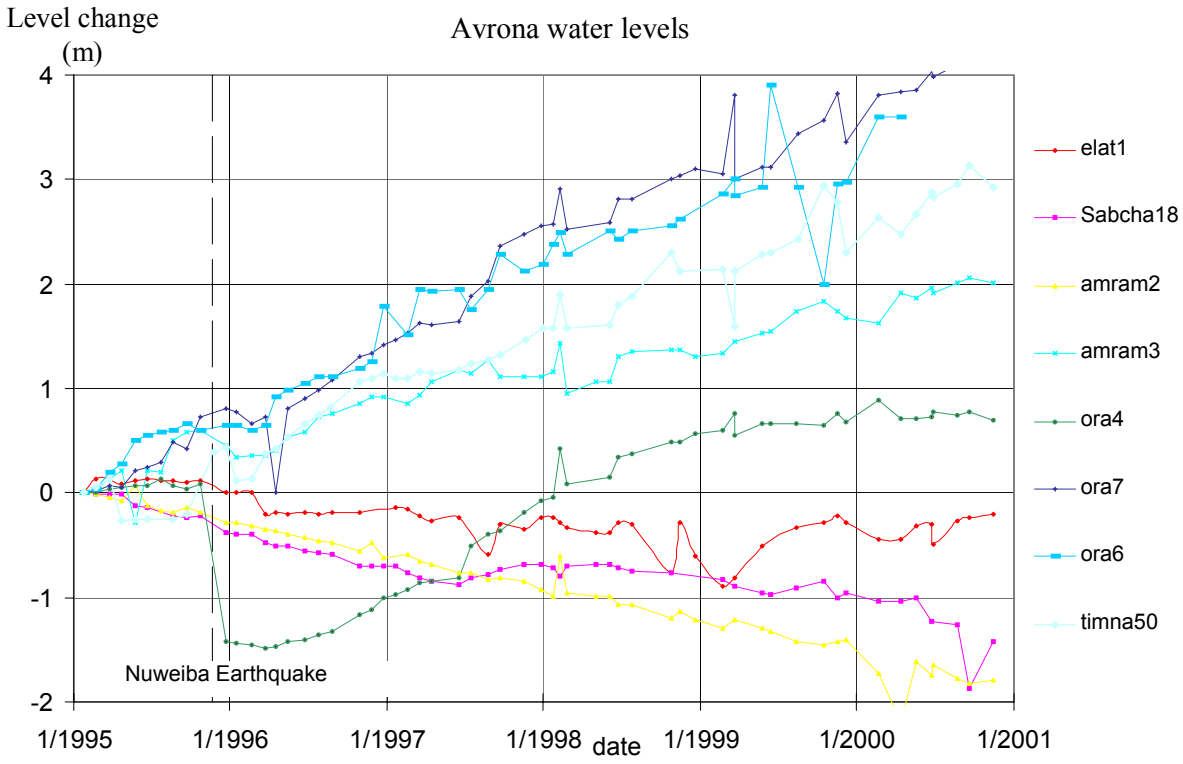

4. TECTONIC ANALYSIS

In this section we present the tectonic interpretation of the surface deformation features described above. We derive fault dislocation models for each of the three features. The model construction was primarily based on finding the dislocation parameters that generate surface displacement similar to the observed. The models were constrained by known geologic features within the DST and by their tectonic context.

4.1 Zofar Basin subsidence

4.1.1 Related tectonic features

Zofar Basin, in which Zofar deformation feature is located, is one of several elongated tectonic basins along the AV (Bartov, 1994). It is approximately 40 km long and 12 km wide confined between Zofar Fault on the west, Arava Fault on the east and Shezaf Fault on the north (Figure 1.1). The basin shallows to the south towards the northern flanks of the structurally uplifted region southeast of Paran (Bartov, 1994; Bartov et al., 1998). Zofar Basin is characterized by a northward thickening of the post Eocene sequence (i.e. Hazeva and Dead-Sea groups) partially due to normal faulting on a series of secondary faults that traverse the basin (Bartov et al., 1998; Frieslander, 2000). The displacements on these secondary faults change from oblique left-lateral with normal displacement in the south (i.e. Wadi-Musa and Um-Mitla faults) to normal faulting in the northern part of the basin (i.e. Bureida and Ein-Yahav faults; Frieslander, 2000). Northern Zofar Fault is traceable at the surface and displays significant normal displacements on a fault plane dipping at 60º-70º to the east (Bartov, 1994; Bartov et al., 1998). Southern Zofar Fault, which is not exposed, was shown by Frieslander (2000) to have smaller vertical displacements. Data from 6 seismic lines near the settlement Zofar, along the western boundary of the observed deformation feature, indicates a vertical displacement of 100-300 m (Frieslander, 2000). In this region, the thickness of post Eocene sequence drops to less than ~1 km, compared to 1-3 km in northern Zofar Basin (Frieslander, 2000).

4.1.2 Fault dislocation models

To model Zofar feature by fault dislocations, we used the previously mapped faults that correlate spatially and structurally with the InSAR observations. The linear trace and high gradients of observed surface displacement along the near surface faults of Zofar and Wadi-Musa suggest that slip along these faults generated the observed surface deformation (Figure 4.1). The similar deformation patterns displayed in ascending and descending interferograms (tracks 343 and 78 respectively; Figure 3.3) indicate the predominance of vertical displacements (subsidence). Yet, one cannot eliminate a possible contribution of horizontal displacement along Zofar fault, as LOS range changes are significantly less sensitive to such displacement (see 3.1.2).

Figure 4.1. Zofar surface deformation (interferogram 20974_29491) and main tectonic features (based on Frieslander, 2000 and Bartov et al., 2002) superimposed on a satellite image of northern AV. The high gradients along the linear borders of the observed deformation correlate with the surface trace of Zofar Fault and Wadi-Musa Fault (WMF). Profiles (a) and (b) indicate an increase of LOS range by 30 mm. In addition, the profiles display background noise level of 5 mm, which is typical in InSAR (Massonnet and Feigl, 1998).

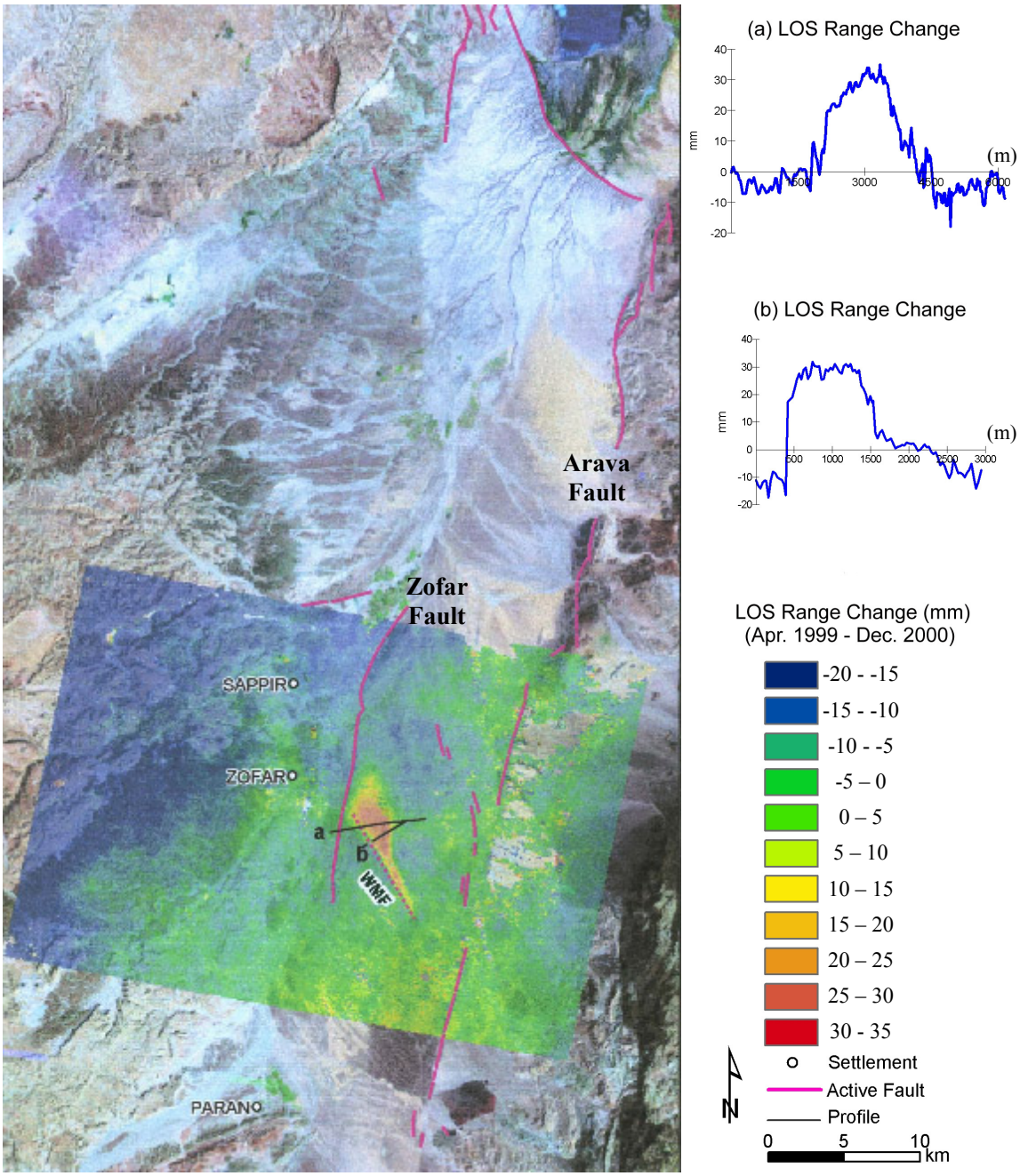

Considering the dominance of vertical displacements on the LOS range change, the GNStress program was used to construct dislocation models, in which the vertical displacement field was compared to the observed LOS range change in the interferograms. The initial models were intended to reproduce the general characteristics of the observed displacement while ensuring that the strike-slip component of the dislocation slip are left lateral (in accord with the DST). These models included oblique slip along two faults that correspond to the known Zofar and Wadi-Musa faults (Figure 4.2). Model parameters (fault location and dimensions, depth to top of fault, slip magnitude, dip and strike) were refined by trial-and-error to fit the observed spatial extent, magnitude and gradient of the subsidence feature. This analysis yielded good constraints for the dislocation solution. For example, the steep displacement gradients at the SW boundary of Zofar feature (Figure 3.3) could not be reproduced by a fault buried deeper than 1.5 km. For similar reasons the southeastern elongated termination of the subsiding area, could only be reproduced by fault slip at the surface. This southeastern elongated deformation zone could reflect an extensional flower structure confining a narrow graben between two parallel fault planes, similar to those observed by Frieslander (2000) along various AV strike-slip segments. However, we attempted to describe our observations using the simplest model geometry and therefore did not incorporate such a possibility in the model. In addition, the model requires that both faults dip less than 75º in order to reproduce the observed asymmetric pattern of deformation in which no surface displacement occurred to the south and west of the faults (Figure 3.3). The GNStress model (Figure 4.2) fits the observed displacement pattern and magnitude in interferograms 20974_29491 and 19870_28754 (Figure 3.3), in particular it reproduces the high displacement gradients and asymmetry mentioned above, and the observed subtle uplift to the north of the subsidence feature.

The synthetic interferogram based on these solutions (Figure 4.3) produced the LOS range-change in interferogram 20974_29491 (25/4/99-10/12/2000). By comparing the synthetic LOS range-change to the observed LOS range-change we refined the dislocation parameters obtained from the GNStress model. The final Zofar model reproducing the entire LOS range-increase of 40 mm, was constructed by extrapolation of the refined dislocation parameters obtained for interferogram 20974_29491 (30 mm of LOS range-increase).

Figure 4.2. Zofar GNStress fault model displaying approximately 40 mm of vertical surface deformation (a), and 30 mm of left-lateral motion (b). The two faults are outlined by black rectangles, horizontal surface deformation field (b) is indicated with arrows (length correlates to magnitude). The vertical displacement field (a) fits the observed deformation pattern and magnitude, and also the subtle uplift to the north of the subsiding feature (yellow area at the northern tip of the fault).

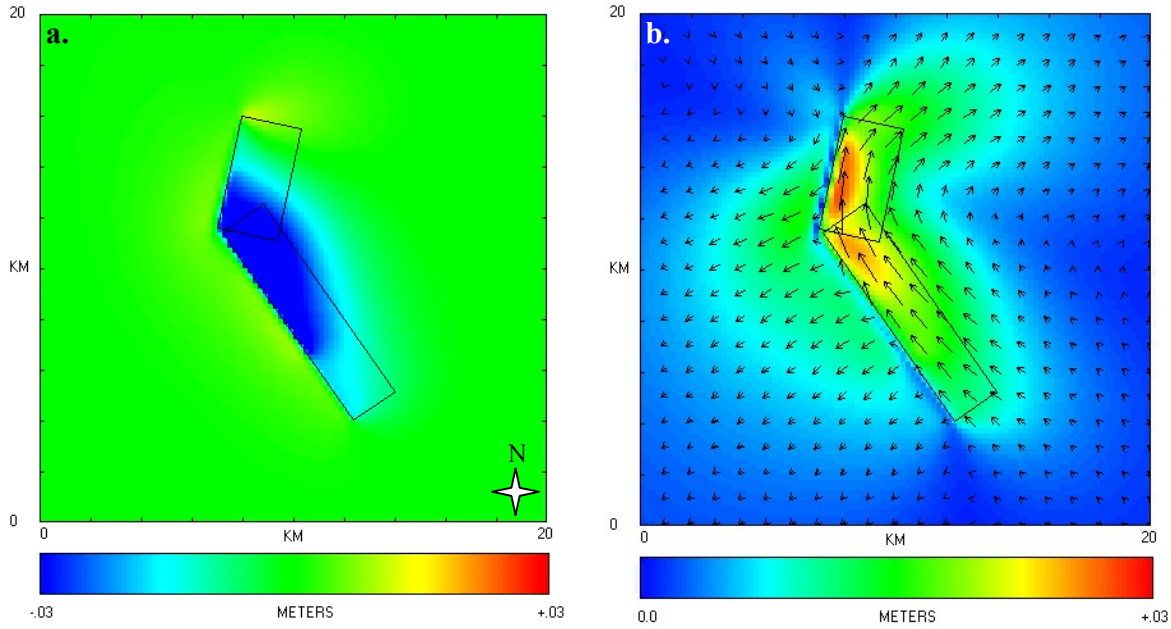

Figure 4.3. Zofar synthetic interferogram displaying surface deformation similar to interferogram 20974_29491 (Figure 3.6). The faults in the model are indicated by black lines, and correlate to surface traces of Zofar and Wadi-Musa faults.

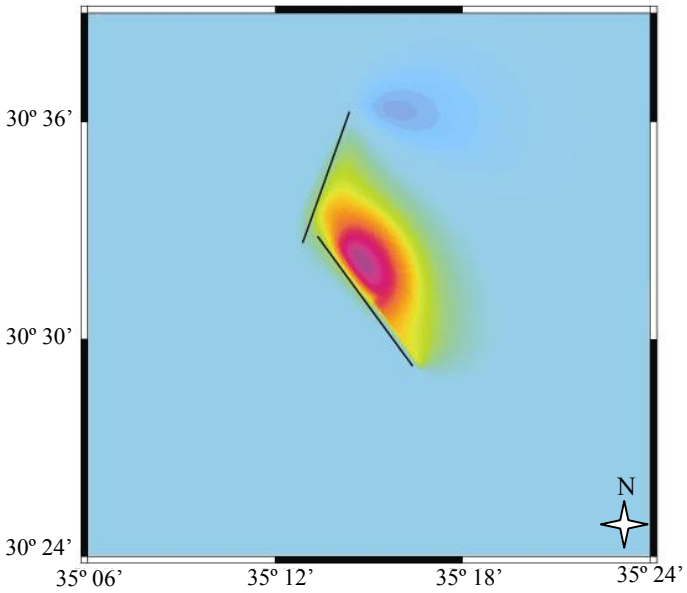

Zofar dislocation model (Figure 4.4, Table 4.1) indicates that during the period of 23/4/98 - 19/10/2000 a slip of ~60 mm occurred over an area of approximately 30 km^2 along Zofar Fault (60º/105º; dip/dip direction), and an average slip of ~35 mm over an area of approximately 35 km^2 along Wadi-Musa Fault (57º/055º). The model rake on Zofar Fault is -25º, namely predominant strike-slip motion, and the model rake on the Wadi-Musa Fault is -80º, namely predominant normal faulting. The dislocation parameters of Zofar model are presented in Table 4.1, and Figure 4.4.

Table 4.1. Fault and slip parameters of Zofar dislocation model (23/4/98 - 19/10/2000).

Fault segment	Dip/ Strike	Length, Width (km)	Top of fault (km)	Slip (mm)	Rake
Zofar	60º/105º	5.7 , 5.0	1.0	60	-25
NW Wadi-Musa	57º/055º	3.8 , 4.5	0.9	54	-83
SE Wadi-Musa	57º/055º	3.8 , 4.5	0.1	19	-82

Figure 4.4. Zofar surface deformation dislocation model (for the entire study period, 40 mm LOS range change). Fault parameters (dip/dip-direction) and slip distribution (rake, magnitude) according to our synthetic interferogram. The rake on Zofar Fault is approximately -25º, and on Wadi-Musa Fault approximately –80º.

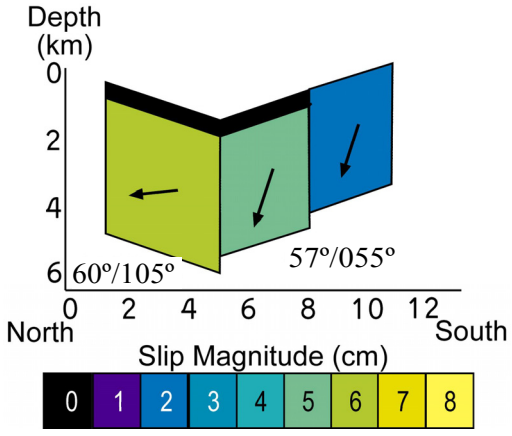

Through trial-and-error we found that a wide range of dislocation parameters yield a synthetic interferogram that reproduces the observed displacement field. This robustness strengthens our tectonic interpretation of the observed surface deformation feature, however it also indicates that variations and tradeoffs may exist in the model parameters. First, due to the inverse correlation between the magnitude of surface displacement and the depth of the source dislocation, geodetic methods (such as InSAR) usually offer poor constrains on the depth extent of model faults (Wright et al., 2004). In the case of Zofar and Wadi-Musa model faults, the vertical surface displacement field deviates from the observed displacement only if their width is extended to ~150% of the selected parameters (Figure 4.5.a). Second, due to the low sensitivity of InSAR to DST-parallel strike-slip

motion (see 3.1.2) the horizontal component of displacement and the related rake are also poorly constrained. Significant deviation from the observed pattern and magnitude of Zofar vertical surface displacement are exhibited only when the horizontal displacements on the model faults are increased by a factor of >1.5 (Figure 4.5.b).

Figure 4.5. Error analysis for Zofar dislocation model (compare with Figure 4.2.a). a. Zofar GNStress model with faults width extended to 150% of the width in our final model. b. Zofar GNStress model with horizontal displacements increased to 200%. The displacement field in both cases (a,b) exhibits a small deviation from our final model.

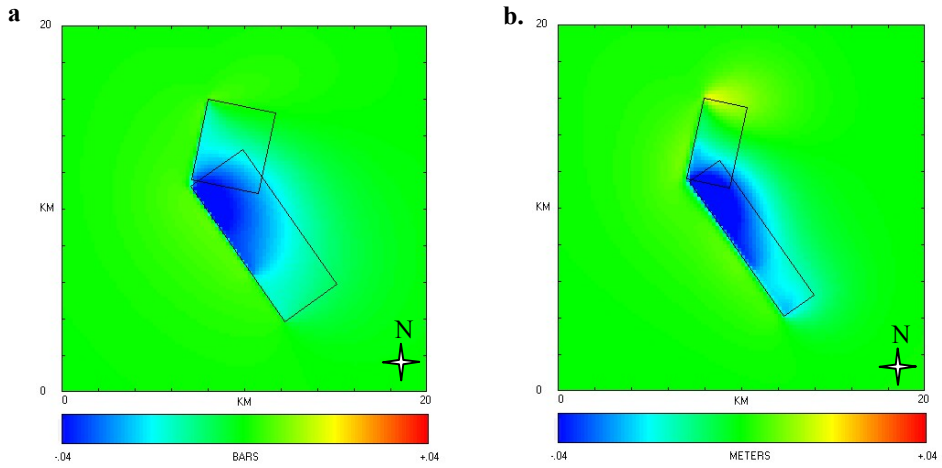

4.2 Yotvata Playa uplift

4.2.1 Related tectonic features

Yotvata Playa is located in the central deepest part of Yaalon Basin in the southern AV (Frieslander, 2000; ten-Brink et al., 1999, 1993). The playa is an internally drained basin approximately 8 km long, 7 km wide (Figure 4.6), it is filled with 1000-1500 m thick sequence of Upper-Miocene and younger sediments (Frieslander, 2000; ten-Brink et al., 1999). The northeastern tip of the playa is delimited by the eastern boundary fault of the Arava (Aqaba-Gharandal Fault; Garfunkel, 1981; Bartov, 1994). The northwestern tip of the playa coincides with the southern termination zone of the Yaalon Fault (Garfunkel, 1970; Frieslander, 2000), which is assumed to accommodate about 60 km of the 105 km of left-lateral displacement along the DST (Bartov, 1994). Based on field mapping and analysis of aerial photos, Garfunkel (1970) suggested that Elat Fault which is the western boundary fault of the Gulf of Elat (Aqaba) approaches the southeastern edge of the playa

and terminates there (coordinate 157/913) without displacing the surface playa sediments (Figure 4.6). An active left stepover between Yaalon Fault (N-NW from Yotvata Playa) and Elat or Aqaba-Gharandal Fault (S-SE from Yotvata Playa) could have been the source of extension and subsidence that formed Yotvata Playa and the deep center of Yaalon Basin.

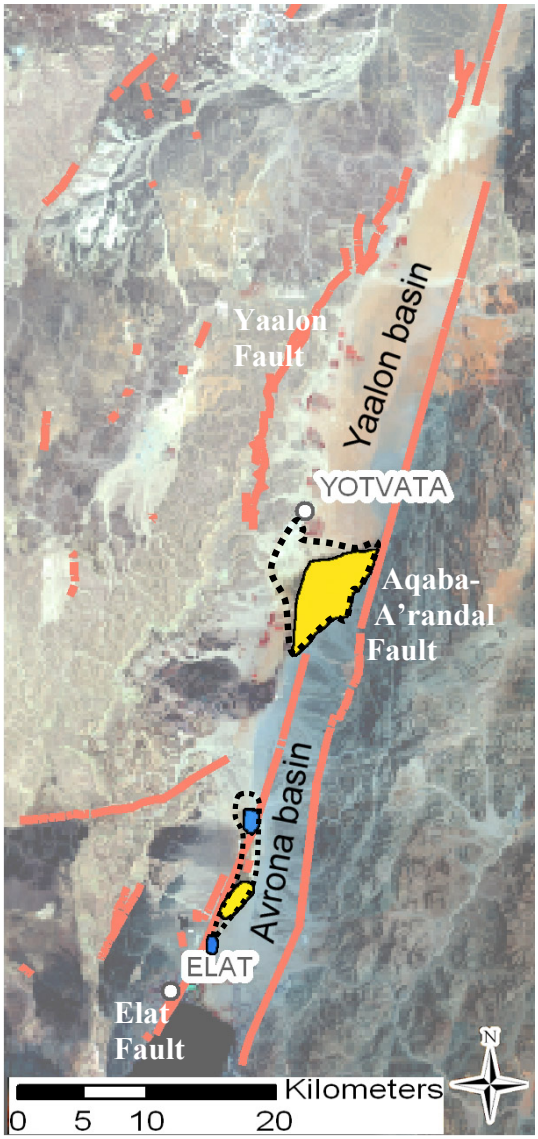

Figure 4.6. Southern AV Landsat image showing Yaalon Basin, Avrona Basin and the location of the observed surface deformation features (blue for subsidence and yellow for uplift). Surface traces of active DST faults are outlined in red (based on Bartov et al., 2002). Yotvata and Avrona playas are outlined based on the geological map of Israel (Sneh et al., 1998).

4.2.2 Fault dislocation models

In the modeling, we assume that Yotvata surface displacement reflects slip along the previously mapped faults of Elat and Aqaba-Gharandal (Garfunkel, 1970) because these faults correlate spatially and structurally with our InSAR observations (Figure 4.6). The uplift at Yotvata Playa suggests a change in the tectonic activity from subsidence at a left stepover to uplift at a right stepover. The current uplift rate (135 mm of LOS range decrease in 50 months) could not have persevered without inducing a substantial topographic expression. This suggests that this current tectonic uplift is either a short term phenomena or represents alternating tectonic activity, for example switching between uplift at the currently suggested right stepover, subsidence at a left stepover, and possibly pure left-lateral displacement along the entire Aqaba-Gharandal Fault.

The dislocation model of Yotvata surface displacement is of a compressional right stepover between two major AV segments. A simple right stepover model consisting of two en-echelon faults could account for part of the observed uplift, but it could not reproduce the asymmetric pattern of uplift and the high deformation gradient along the linear southeastern boundary of the uplifted area (Figure 3.7). These observations suggest that the stepover is interconnected by a near-surface reverse fault with a left-lateral slip component.

A synthetic interferogram (Figure 4.7) reproducing the 45 mm of LOS range-change in interferogram 19369_21874 (March - September 1995) was used to determine the dislocation parameters for Yotvata surface deformation model. The resulting model (Figure 4.8, Table 4.2) indicates that both AV fault segments (strike N15ºE) accommodate between 85 mm of left-lateral slip (near the stepover) and 20 mm (away from the stepover). The gradually decreasing displacements on the segments of these faults are required to fit the lack of observed displacements along the faults' extensions away from the stepover (Figure 4.7). Both strike-slip faults in this model dip to the west at angles of approximately 70º±5º; this inclination is essential in order to reproduce the asymmetric surface displacement pattern (displacement is confined to the western side of these faults). The tops of the two strike-slip faults are buried to depths of approximately 2 km, and the width of dislocations on these faults are 2-4 km. According to our model, the central reverse fault (dip 50º/320º) is 6.5 km long, 3.5-5.5 km wide, and it almost reaches the

surface (depth to top <500 m). The reverse fault consists of two segments with slip magnitudes of 85 and 25 mm on the NE and SW segment, respectively. Both segments exhibit a vertical component slightly larger than the horizontal component (rake is ~50º). The relatively low dip of this fault is necessary to enable the shallow depth of the fault top while reproducing the asymmetric surface deformation observed (abrupt uplift NW of the fault trace with no subsidence on the SE side).

It should be noted again that due to the low sensitivity of InSAR to DST-parallel displacements and to lateral displacements at depth, the faults may extend deeper than suggested in our model and the length of the strike-slip faults may be much greater (with a limit of surface displacements lower than 25 mm during the study period, see 3.1.2). In addition, the slip magnitude and depth of the strike-slip model faults are not well constrained due to the possible tradeoff between these parameters. The dimensions and slip parameters of the central reverse fault are better constrained by the observations (i.e. linear SE border and high displacement gradient along it).

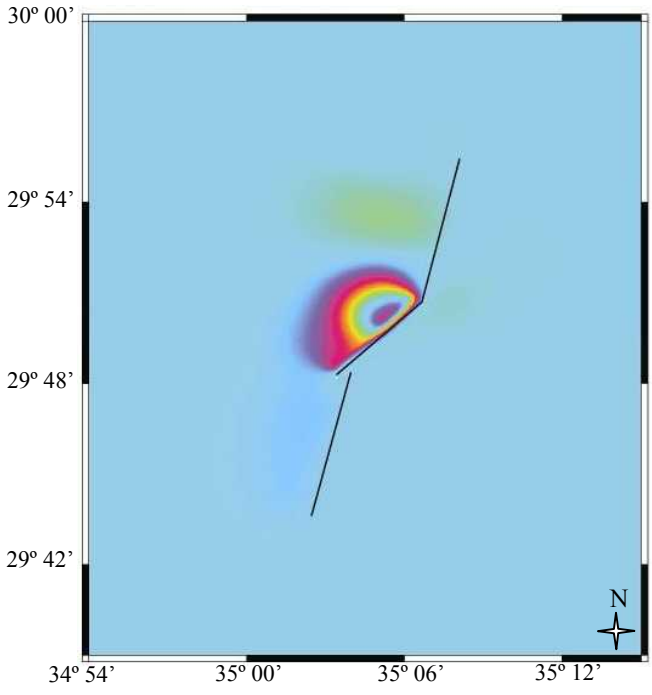

Figure 4.7. Yotvata synthetic interferogram resembling surface deformation exhibited in interferogram 19369_21874 (Figure 3.7). Black lines indicate the faults in the model. The southwestern fault correlates with the inferred continuation of Elat Fault (Garfunkel, 1970), and the northeastern fault correlates with the surface traces of Aqaba-Gharandal Fault (Garfunkel, 1970; Bartov, 1994).

Table 4.2. Fault and slip parameters of Yotvata dislocation model (29/3/95 - 20/9/95). The faults are noted AGF for Aqaba-Gharandal Fault, Reverse for the reverse fault, and Elat for Elat Fault, the segments of each fault are described in order from north to south and noted N, C (Central), or S.

Fault, Segment	Dip/ Dip direction	Length, Width (km)	Top of fault (km)	Slip (mm)	Rake
AGF, N	70º/285º	3.0, 2.5	2.1	20	0
AGF, C	70º/285º	3.0, 2.5	2.1	40	0
AGF, S	70º/285º	3.0, 2.5	2.1	85	0
Reverse, N	50º/320º	3.2, 4.0	0.5	86	+49
Reverse, S	50º/320º	3.2, 4.0	0.5	26	+50
Elat, N	70º/285º	3.0, 2.0	1.7	75	0
Elat, C	70º/285º	3.0, 2.0	1.7	35	0
Elat, S	70º/285º	3.0, 2.0	1.7	20	0

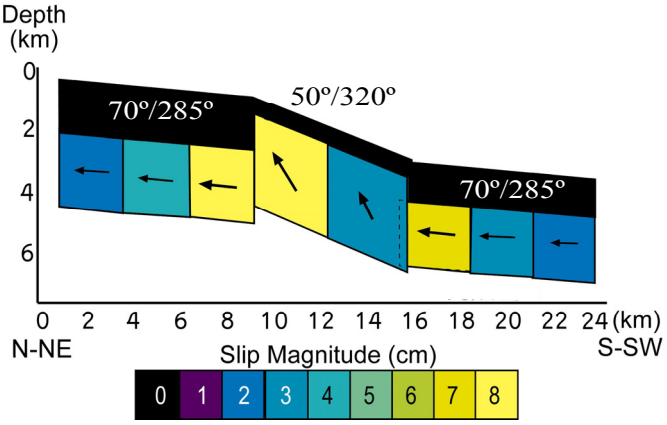

Figure 4.8. Yotvata surface deformation dislocation model (for Mar.-Sep. 1995, 45 mm LOS range change). Fault parameters (dip/dip-direction) and slip distribution (rake, magnitude) according to the synthetic interferogram (Fig 4.7). Dislocation parameters are summarized in Table 4.2.

Based on Yotvata synthetic interferogram and dislocation model of the displacement observed in interferogram 19369_21874 (Mar.-Sep. 1995; 45 mm of LOS range-decrease) we estimated the slip that occurred during the entire study period. As the total (3/1995 – 5/1999) LOS range-decrease accumulated to 135 mm (triple than during Mar.-Sep. 1995) we estimate that the total slip values on the model faults are triple than those in Table 4.2. Namely: Aqaba-Gharandal model fault segments slipped 60 mm, 120 mm, 255 mm (N, C and S segments respectively); The reverse model fault segments slipped 258 mm, 78 mm (N and S segments respectively); And Elat model fault segments slipped 225 mm, 105 mm, 60 mm (N, C and S segments respectively).

4.3 Avrona Basin surface deformation

4.3.1 Related tectonic features

Avrona Basin is one of several en-echelon tectonic basins bounded by left stepping subparallel DST segments (Garfunkel et al., 1981; Frieslander, 1995). It is approximately

20 km long and 5 km wide (trending N20º-25ºE), and is filled with fluvial post-Eocene sediments up to 2000 m thick (Ben Gai et al., 1993; Frieslander, 1995). Being the on-land continuation of the Gulf of Elat (Aqaba), Avrona Basin is confined between Elat Fault in the west and Aqaba-Gharandal Fault in the east (Zak and Fruend, 1966; Garfunkel et al., 1981; Reches et al., 1987). The Avrona Playa is a 10 km-long and 1–2 km wide area at the southwestern quadrate of Avrona Basin (Figure 4.6). It is crossed diagonally by a north-northeast trending branch of Elat Fault (Garfunkel, 1970; Shtivelman et al., 1997). The playa area at present is an open basin that drains southward through Elat coastal plane toward the Gulf of Elat (Aqaba). It consists of an elevated ridge (composed of low longitudinal subridges up to 4 m high and 5 km long) and shallow braided channels flowing along and across these ridges (Amit et al., 1999). Paleoseismic studies y of Avrona Playa indicated that at least six surface rupture events affected the Avrona Playa during the past 14,000 yr, the last of which occurred in 1068 A.D. (Shtivelman et al., 1997; Amit et al., 2002).

4.3.2 Fault dislocation models

Although Avrona surface displacement could not be fully attributed to tectonic processes, we constructed a fault dislocation model assuming that apart from the uplift observed at Avrona South (4/97-1/99) the entire surface displacement is tectonic (see subsection 3.2.3). The faults in our model correlate with lineaments that we mapped on aerial photos (Figure 4.9) as well as active faults mapped by Garfunkel et al. (1981) and Amit et al. (2002).

The dislocation model of Avrona feature consists of four sub-parallel fault segments forming two extensional stepovers and a fifth fault exhibiting a reverse slip component (Table 4.3, Figure 4.10, Figure 4.11). According to this model, the subsiding zones of Avrona North and Avrona South are generated by oblique slip (normal and left-lateral) on four DST-parallel faults (strikes N5ºE - N25ºE). These faults are buried 500-1000 m below the surface, they dip towards each other at angles of 70º-80º and their width is 4-6 km (Table 4.3). The uplift at central Avrona is modeled as compression along a fault segment (N45ºE) that deviates by approximately 30º from the typical DST orientation. This NE trending fault segment almost reaches the surface (depth of top < 500 m), it dips at 75º-80º to the NW, and its width is 3-4.5 km. The above model fault characteristics were derived

from the GNStress model of the deformation that occurred during 3-11/1995 (Figure 4.10) and from the refined model based on the synthetic interferogram representing the period of 3/1995-5/1996 (Figure 4.11).

Figure 4.9. An aerial photo of the SW corner of Avrona Basin showing Avrona Playa and Elat coastal plane in the south. Surface lineaments are outlined in black, inferred active faults relevant to Avrona dislocation model are outlined with dashed red lines (compiled from Garfunkel et al., 1981; Amit et al., 2002), and the deformation features are superimposed (blue for subsidence and yellow for uplift).

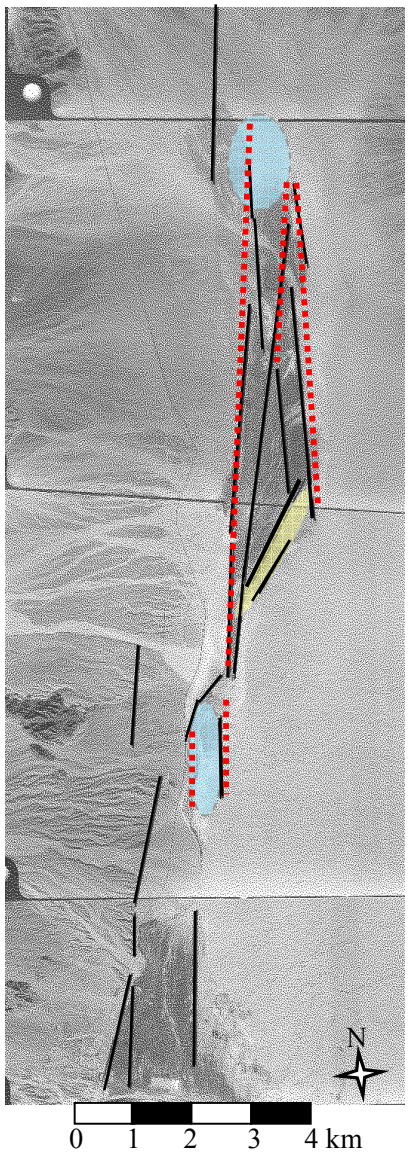

Table 4.3. Dislocation parameters of Avrona model for the entire study period (29/3/95 - 28/1/99, disregarding the uplift at Avrona South). Faults are listed from north to south. The slip and rake values in the table represent the average values of all segments of each fault. The solution ranges of the width, slip and rake are noted in brackets.

Fault (num. of segments)	Dip/ Dip direction	Length (km)	Width (km)	Top of fault (km)	Slip (mm)	Rake
NW (2)	70º/103º	3.4	5.0 (3-9)	0.9	65 (±30)	-33 (±15)
NE (3)	77º/275º	4.5	5.0 (3-9)	0.6	70 (±40)	-20 (±10)
Central (3)	78º/315º	2.5	3.5 (2-8)	0.3	90 (±50)	+21 (±10)
SW (2)	75º/115º	3.8	5.0 (3-9)	0.9	60 (±30)	-22 (±10)
SE (2)	75º/282º	3.6	4.5 (3-8)	0.8	90 (±40)	-38 (±15)

Figure 4.10. GNStress dislocation model of Avrona deformation consisting of five sub-parallel segments (fault planes projected to the surface). The model reproduces surface deformation observed during 3-11/1995 in Avrona North (26 mm subsidence), Central Avrona (13 mm uplift) and Avrona South (22 mm subsidence).

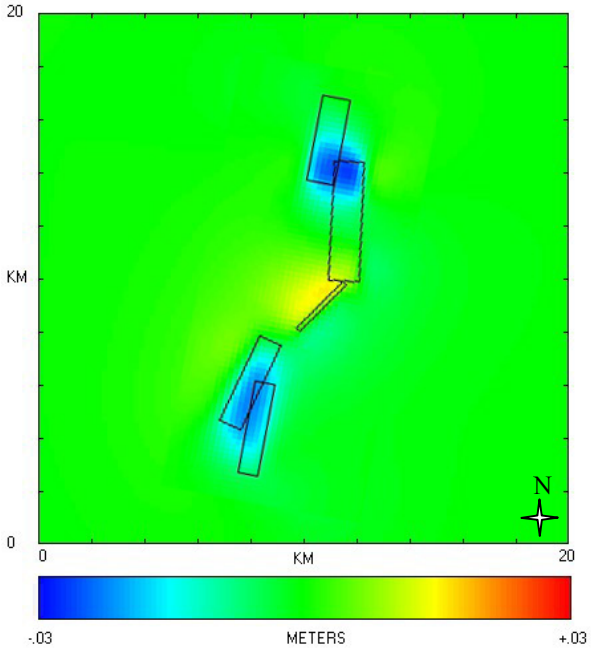

Figure 4.11. Synthetic interferogram of Avrona deformation features during the period of 3/1995-5/1996. The model displays subsidence of 30 mm at Avrona North and 25 mm at Avrona South. At Central Avrona it displays uplift of 20 mm.

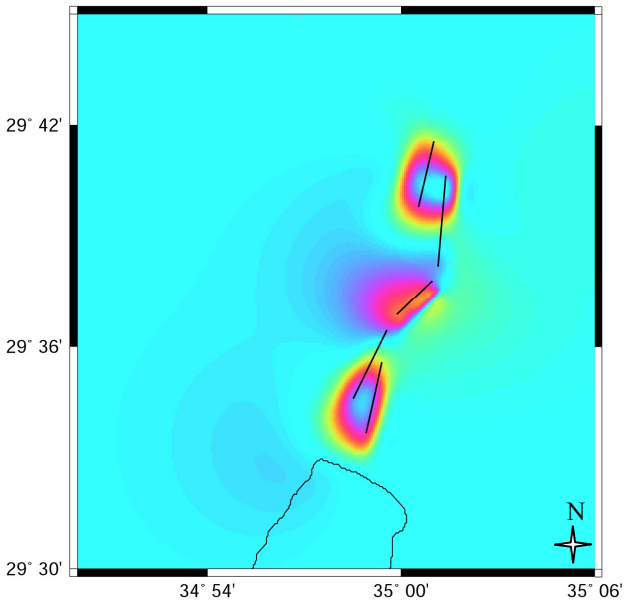

Although our final Avrona model reproduces the observed displacement pattern and magnitude (Figure 3.6, 3.7), it should be noted that the lack of distinctive features (e.g. linear boundaries, high displacement gradients and asymmetric pattern) limits our ability to resolve tradeoff between parameters and to better constrain the model parameters. In particular, the fault width and average slip are poorly constrained due to the low sensitivity of InSAR to slip at depth and to DST parallel displacements, and due to the tradeoff between slip-magnitude and fault-depth. By way of trial-and-error we estimate that the width of the model faults may range between 60% and 200% of the selected value, and the slip and rake values have an error range of 50% (Table 4.3). An additional shortcoming of the proposed model is the wide spread uplift it generates along the western side of the Avrona Playa (Figure 4.11). This uplift could represent subtle (~5 mm) displacement that occurred gradually during 3/1995-5/1996. Such a displacement might not be detected in interferograms with shorter time span (e.g. 19369_21874, 03203_25381, 21874_22876 in Figure 3.7) and might be obscured by decorrelation or by other InSAR artifacts in interferograms with a long time span.

5. IMPLICATIONS: ASEISMIC DEFORMATION WITHIN ARAVA VALLEY

5.1 Aseismic nature of observed deformation features

We have modeled the observed InSAR displacements by slip along fault segments in Zofar, Yotvata and Avrona regions (Tables 4.1, 4.2, 4.3). In this section, we examine the nature of the modeled deformation, and conclude that it was induced by aseismic fault creep. In the following section we evaluate the role of creep in accommodating seismic moment accumulated along the AV segments of the DST.

Although Zofar and Yotvata features are located in seismically active regions of the AV (Figure 3.1), the timing of the observed displacements does not correlate with periods of increased seismicity rates. During 1990-2000, about 20 earthquakes of magnitude $2.5<M_L<3.7$ occurred in Zofar region (GII, 2000); we calculated a relatively constant seismicity rate of $1.3 \cdot 10^{14}$ N·m/yr for this period. The creep period in Zofar was

accompanied by a decrease in seismicity with only two $M_L > 2.5$ earthquakes during 1998-2000 (Figure 5.1.a). Further, the M_L=4.2 earthquake of 08/10/2001 occurred 5 km from the location of Zofar feature without inducing any surface displacement. In Yotvata the creep rate and seismicity are both relatively high in 1995, but they do not show a correlation during the period of 1996-1999 (Figure 5.1.b). During the period of highest creep rate (3-10/1995) only four small earthquakes were recorded ($1.5<M_L<2.5$), and during 1999 when the creep rate rises again only two earthquakes were reported (M_L=1.7, M_L=1.9). In the case of Avrona, due to the possibility that post 1997 displacement is not entirely tectonic, the creep period is too short to compare with temporal changes in seismicity rate. It is noteworthy that, as in Yotvata, the creep rate in Avrona is maximal during 3-9/1995 and the seismicity rate is maximal during 11-12/1995. A second indication that the modeled slip is induced by creep rather than by earthquakes is the gradual and monotonous accumulation of surface deformation (Figure 5.2). Finally, the moment released by the

Figure 5.1. Temporal comparison between creep intensity and seismicity intensity in the regions of Zofar (a) and Yotvata (b). Seismicity is presented as yearly seismic moment released by earthquakes near the creep features (within a distance < 15 km). Creep is presented as yearly LOS range change (Tables 4.1, 4.2).

a. Zofar creep displays no temporal correlation with the region's seismicity.

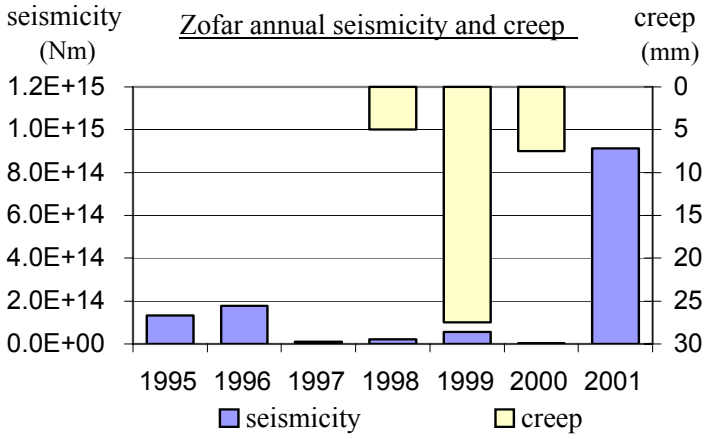

b. Yotvata creep displays no apparent correlation with the region's seismicity during 1996-99. An apparent correlation appears for 1995 that is probably related to the aftershocks of Nuweiba earthquake.

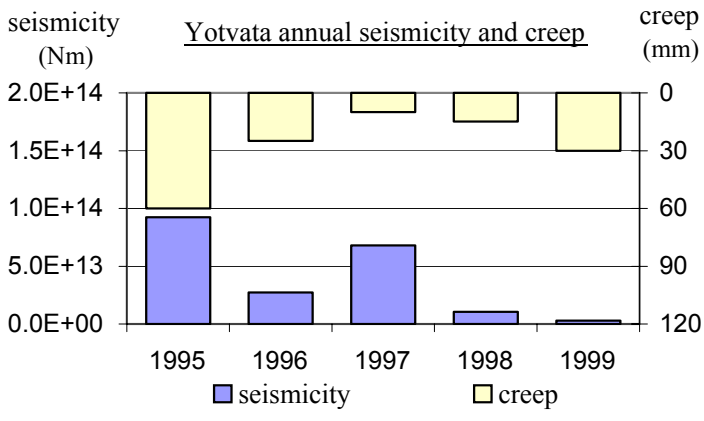

modeled dislocations is two orders of magnitude greater than that released by earthquakes recorded during the study period (Figure 5.2).

Figure 5.2. Seismic moment released by creep events (left Y axis) and by earthquakes (right Y axis) along the AV. The moment release by earthquakes is dominated by three large events in the vicinity of the AV: Oct. 2001 - Zofar earthquake M_L=4.2; Dec. 1999 – Themed earthquake M_L=4.1 (located approximately 15 km SW of Yotvata); Nov. 1995 – Nuweiba aftershocks in southern AV.

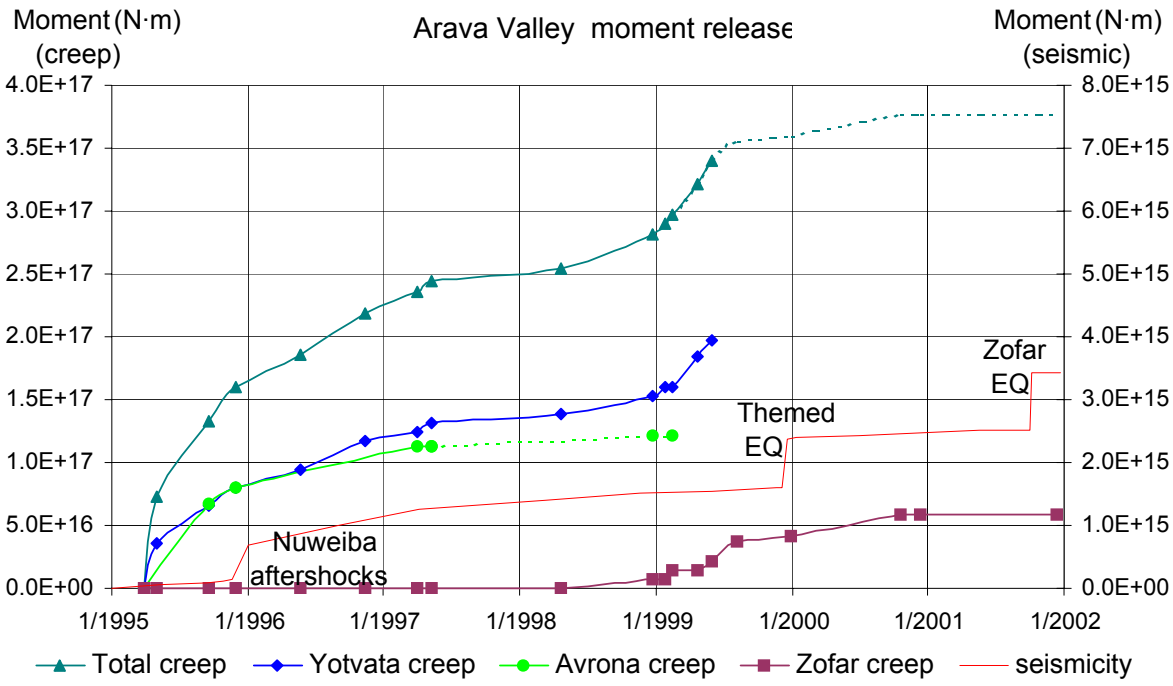

5.2 Aseismic moment release and aseismic efficiency

To examine the contribution of creep to the tectonic activity along the AV segments of the DST, we calculate the moment released by the modeled creep events. Two parameters are derived from the calculated moment: the "equivalent magnitude" (M_e) that estimates the magnitude of an earthquake with moment release similar to that of the modeled creep, and the "aseismic efficiency" that represents the ratio between the moment released by aseismic creep and the expected seismic moment accumulation along the AV. Following Kostrov (1974), the moment released by creep (hereafter referred to as "aseismic moment") is defined as: $M_0=\mu As$

where A is fault area, s is the average slip and μ is the crustal rigidity. This relation was derived from dislocation theory of faulting (Maruyama, 1963) and it is used to calculate seismic moment release in earthquakes (Brune, 1968; Kanamori and Anderson, 1975), as

well as moment release in aseismic creep (Kostrov, 1974).

For the present calculations, the rigidity was estimated from shear wave velocities and density profiles of shallow (1-12 km) units in the Arava Valley (Al-Zoubi and ten Brink, 2002; Desert Group, 2002, 2004; Frieslander, 2000). These works indicate that the properties in the upper 12 km of the AV basins are: ρ~2200 kg/m^3 and Vs~1.5-2 km/s for Pliocene-Recent sediments, ρ~2400 kg/m^3 and Vs~2-2.5 km/s for Miocene rocks, and ρ~2600 kg/m^3 and Vs~3-3.5 km/s for pre-rift sequences. Considering the thickness and lithology variations in the local basins the following rigidity values were used. An average rigidity of 20 GPa was estimated for the top 12 km of the AV basins. An upper rigidity limit of μ =30 GPa represents the rigidity at 7-12 km depth, in agreement with values used in seismic studies of the DST (Salamon et al., 1996; Shamir, 1996). A lower limit of μ =10 GPa was estimated for the Quaternary units found near the surface of the AV. The creep parameters of fault area and average slip from were derived from our dislocation models (Tables 4.1, 4.2, 4.3). Error analysis of the aseismic moment calculation is based on the observation that the average slip is better constrained than the rigidity and the fault area. The estimated errors for these parameters are 30-50%, 50% and 40-60% respectively. The plausible range of solutions was estimated using the minimal and maximal credible fault area and the rigidity (Figure 5.3). This calculation produced an error range with values between ~30% and ~240% of our moment release best estimation.

Figure 5.3. Aseismic moment error analysis demonstrated on Wadi-Musa Fault (WMF) parameters. Estimation of the plausible solution range was done by plotting equal rigidity lines (μ=10,20,30 GPa) and lines of plausible fault area (A=25, 34, 50 km^2) on a moment versus fault area graph. The intersection of the minimal fault area and minimal rigidity indicates the minimal (plausible) aseismic moment released in the dislocation. This analysis suggests that the moment release on WMF during the study period is M_o =2.4 $\cdot 10^{16}$ N·m ($0.9 \cdot 10^{16}$ – $5.25 \cdot 10^{16}$ N·m).

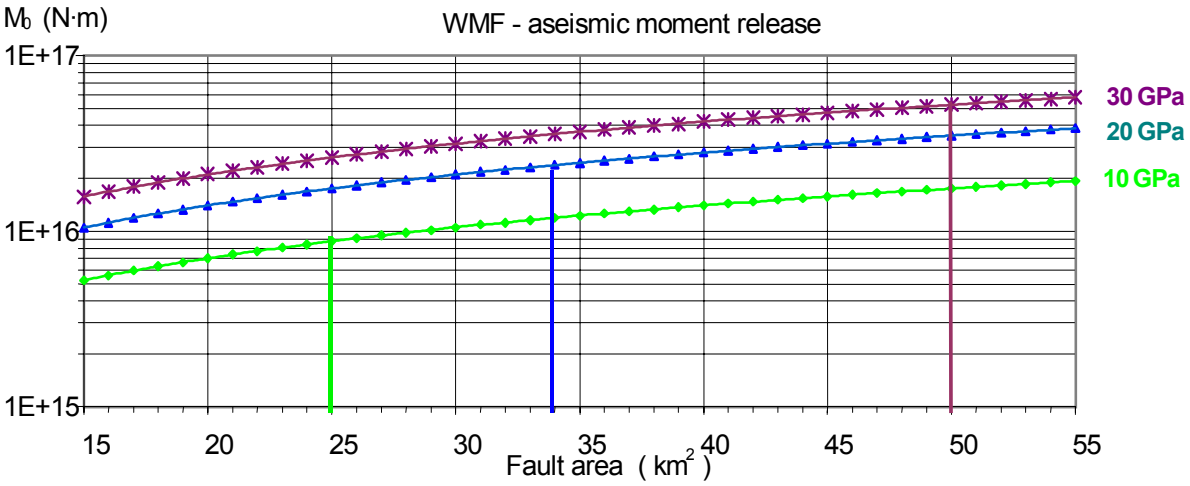

The aseismic moment calculations indicate that during the period of 3/1995-5/1999 creep at Yotvata released $M_o=19.7\cdot10^{16}$ N·m. Zofar creep event (4/1998-10/2000) released $M_o=5.9\cdot10^{16}$ N·m. And the creep at Avrona released $M_o=12.2\cdot10^{16}$ N·m during the period of 3/1995-1/1999 (Table 5.1 and Figure 5.2).

The "equivalent magnitude" is calculated here as the magnitude of a virtual earthquake that releases the same amount of seismic moment as the aseismic moment release calculated for the modeled creep events (Table 5.1). The "equivalent magnitude" was calculated using two moment-magnitude relations recently published based on DST earthquake shear-wave spectra, $Log(M_o)=(1.5\pm0.1)M_L+(16.0\pm0.4)$ (Shapira and Hofstetter, 1993), and $Log(M_o)= (1.59\pm0.07)M_B+(15.63\pm0.28)$ (Shapira and Hofstetter, 2000). These relations are in agreement with moment-magnitude relations deduced from Californian earthquakes and from global seismicity (see Shapira and Hofstetter, 1993, 2000). The equivalent magnitudes calculated from these relations were also compared to a moment-magnitude relation based on low magnitude earthquakes in the Dead Sea region, $Log(M_o)=1.2M_L+17.0$ (Van Eck and Hofstetter, 1989), and to a relation derived from European seismicity $Log(M_o)=33.87-[197.37-20.83M_L]^{0.5}$ (Ambraseys and Free, 1997).

The equivalent magnitudes assigned to Yotvata, Zofar and Avrona creep events are $M_e=5.5$, $M_e=5.2$ and $M_e=5.4$ respectively (Table 5.1). These equivalent magnitudes are significantly higher than the cumulative magnitude of seismic events recorded in the regions of the deformation features during the previous decade, and even during the entire previous century. This suggests that the observed deformation could not have been induced by recorded seismic events or by events smaller than the detection threshold of the Israel Seismic Network along the AV (M~1.5; Hofstetter, 2003 personal communication), and therefore the displacement is considered aseismic. The high equivalent magnitudes assigned to the modeled creep events manifest the importance of aseismic creep in accommodating the seismic moment accumulated along the AV segments of the DST.

Calculation of the error range of the equivalent magnitude (Table 5.1) was based on the error range of the moment released in each creep event (using Shapira and Hofstetter, 1993, 2000).

Table 5.1. Aseismic moment release and equivalent magnitude of modeled creep events. Equivalent magnitude and Moment release error ranges are presented in brackets. Moment release error ranges are calculated according to the plausible variations in modeled dislocation parameters.

Creep site	Moment release (N·m)	Equivalent magnitude
Zofar	$5.9 \cdot 10^{16}$ $(1.5\text{-}18.8 \cdot 10^{16})$	5.2 (4.8-5.5)
Yotvata	$19.7 \cdot 10^{16}$ $(6.6\text{-}52.0 \cdot 10^{16})$	5.5 (5.2-5.8)
Avrona	$12.2 \cdot 10^{16}$ $(2.6\text{-}41.5 \cdot 10^{16})$	5.4 (4.9-5.7)

The M_e error ranges for Yotvata and Zofar are well within the magnitudes derived from Ambraseys and Free (1997) and Van Eck and Hofstetter (1989) (yielding $4.6 < M_e < 5.6$ for Zofar, and $5.1 < M_e < 6.1$ for Yotvata), and within the accuracy limits calculated by Shapira and Hofstetter (1999, 2000) for their moment-magnitude relations. This indicates that the moment release error ranges calculated for Yotvata and Zofar do not inflict a wide M_e error range (M_e values are robust). The wider range of M_e in the case of Avrona results from the poorly constrained parameters, particularly slip magnitude and fault width. Finally, it is important to note that moment-magnitude relations are based on elastic rheology, and are calibrated using earthquake shear-wave spectra (Brune, 1970; Shapira and Hofstetter, 1993). Therefore these relations do not necessarily represent the physical process of creep.

To evaluate the aseismic efficiency we calculated the expected annual moment accumulation on the AV segment of the DST using the relation $M_o = \mu A s$ where s is the annual slip. A moment accumulation rate of $1.42 \cdot 10^{17}$ N·m/yr along the entire AV was calculated using the following parameters: seismogenic width w=10 km (Salamon et al., 1996), fault length 170 km (Elat to the Dead Sea Basin), rigidity μ = 27 GPa (average rigidity of the upper 15 km along the AV), and slip rate s=3.1 ± 1.1 mm/yr (current geodetic rate estimated for AV and Dead Sea region by Wdowinski et al., in press). The accurate determination of aseismic and seismic efficiencies require discrimination of the moment released by horizontal DST-parallel displacements from other slip components, which is problematic with available seismic and geodetic data. Therefore, the calculated efficiencies may be regarded only as crude estimates.

The aseismic and seismic efficiencies during 1995-1999 are calculated here by summing the moment released by creep and by earthquakes, respectively, in the AV region, and dividing them by the estimated moment accumulation during this time. During

the period of 3/1995-5/1999 the mean aseismic efficiency is 55% (45%-90% for slip rates of 4-2 mm/yr). This value is two orders of magnitude larger than the seismic efficiency of the AV (~0.3%, based on GII earthquake record), indicating that aseismic creep plays a central role in the current moment balance of the AV segment of the DST.

6. DISCUSSION

6.1. Creep along strike slip fault systems

Aseismic deformation detected within the AV indicates that some portions of Elat, Aqaba-Gharandal and Zofar faults, all of which are principal AV segments, are currently creeping or display episodic creep events. Such creep has been reported along other major strike-slip systems in the world. The most documented and studied are the creeping segments along the North America - Pacific plate boundary: the San Andreas Fault (SAF), Calaveras Fault (CAL) and Hayward Fault (HF) (Prescott and Lisowski, 1983; Bakun and Lindh, 1985; Roeloffs, 2000; Tullis, 1999; Wyss et al., 1990; Nadeau and McEvilly, 1999; Simpson et al., 1988; Lyons and Sandwell, 2003). Along these faults dense arrays of geodetic and geophysical instruments accurately monitor displacements and strains, velocity and acceleration, electric, magnetic and seismic variations (Roeloffs and Langbein, 1994). Continuous surface creep is measured along these fault segments, with averages slip rates of: ~30 mm/yr along the SAF (Lienkaemper and Prescott, 1989), ~3 mm/yr along the CAL (Prescott and Lisowski, 1983) and ~6 mm/yr along the HF (Prescott and Lisowski, 1983; Burgmann et al., 2000; Simpson et al., 2001; Malservisi et al., 2003). According to Roeloffs and Langbein (1994), the creeping section of the SAF accommodates aseismically 40-50% of the plate motion between the North America and Pacific plates. According to the seismic hazard analysis for the San-Francisco Bay area (WG99) aseismic efficiencies of 40%, 20% and 60% were assigned for the Northern HF, Southern HF and CAL faults respectively.

Comparing the aseismic efficiency of the AV (~55%) to the aseismic efficiencies of these creeping faults could imply that the AV is a creeping segment of the DST. In

addition, the AV and the creeping segments of the SAF and HF are bounded by highly seismic sections of the DST (Salamon et al. 2003; Garfunkel et al., 1981), the SAF (Ward, 1998) and the HF (Lienkaemper et al., 1991). In particular, the episodic creep and apparent seismic gap documented along the AV (Amit et al., 2002; Salamon et al., 1996; Ben Menahem, 1991; Ambraseys et al., 1994) resemble characteristics of the Parkfield segment of the SAF. In spite of the to significant differences of size, rates and tectonic styles between the AV of the Dead Sea system and the SAF, HF and CAL of the San Andreas system, it is striking that these systems display fairly similar creep characteristics.

6. 2 Vertical creep at transform stepovers - contribution to basin formation

Substantial aseismic uplift and subsidence detected at the AV stepovers of Zofar, Yotvata and Avrona indicate that creep could contribute to the formation of local basins and ridges within the AV. The role of such creep events in basin formation can be evaluated by comparing the vertical slip rate measured at Zofar and Yotvata (15 mm/yr, 28 mm/yr, respectively) to documented vertical rates at AV local basins. The subsidence rate at basins along the AV varies from less than 0.1 mm/yr (since the Miocene) in the southern end of Zofar Basin to approximately 1-2 mm/yr (since the Pleistocene) in Southern Dead Sea Basin (Frieslander, 2000; Gardosh et al., 1990). Paleoseismic studies conducted within Avrona Playa (Amit et al., 2002; Amit et al., 1999) suggested that tectonic (seismic) uplift of 2-4 m occurred during the past 14,000 years while normal slip occurred on faults flanking the playa (western margin of the playa) at a similar average rate (0.1-0.3 mm/yr). It is suggested here that episodic creep at stepovers could play an important role in the formation of local basins within the AV. For example, the occurrence of seven “Zofar-like” creep events on consecutive fault stepovers within Zofar Basin (i.e. Wadi-Musa, Um-Mitla, Bureide, En-Yahav etc) could induce an average subsidence of 25-30 mm throughout the basin (accounting for 70-130 years of basin subsidence at long-term rates of 0.2-0.4 mm/yr). Such creep events would also accommodate 15-30% of the left lateral slip along Zofar section of the AV (average slip of ~65 mm), and release 10-20% of the seismic moment accumulated within Zofar basin during that time.

6.3 Seismic hazard implications

The importance of creep for seismic hazard evaluation is discussed in various papers dealing with creeping transform segments such as the SAF, HF and CAL. Several studies suggested that creep reduces seismic hazard by accommodating strain along plate boundaries. In San-Francisco bay area, both the HF and CAL faults are creeping at the surface with slip rates of 6 mm/yr and 3 mm/yr respectively (Prescott and Lisowski, 1983). To evaluate how much of the seismic moment is accommodated aseismically, long term (~30 yr) slip rates were measured using geodetic instruments and offset cultural features (Simpson et al., 2001), and short-term slip rates were measured using space geodetic instruments (InSAR and GPS, Burgmann et al., 2000). Fault models based on these measurements indicate that during 1992-1997 creep rates of 3-7 mm/yr dominate the upper 6 km of the HF and reach the bottom of the seismogenic crust (12 km) along a ~20 km segment of the Northern HF and at the southern end of the HF. Based on the creeping fault model by Burgmann et al. (2000) and on a long-term slip rate of ~10 mm/yr, it is possible to calculate a 25-35% aseismic efficiency for the HF. This value is in agreement with the aseismic efficiency assigned in the seismic hazard analysis for the San-Francisco Bay area (WG99). Determination of the seismic and aseismic moment release rates enables the estimation of the moment accumulation since the last earthquake. According to Lienkaemper et al. (1991), in spite of the creep on HF the seismic moment accumulated since the last earthquake (Oct. 1968, M~6.8) corresponds to a M~6.8-7 earthquake potential. This assessment is in agreement with the high earthquake probability assigned by the WG99 for the HF. The creep detected at AV stepovers accommodates a significant portion (~50%) of the strain along the plate boundary reducing the moment accumulation rate to $6.4 \cdot 10^{16}$ N·m/yr (see 5.2). This implies that creep reduces the seismic hazard along the AV, however as the moment accumulation rate is based on short-term measurements (~7 yr), it might not represent the long-term tectonic activity along the AV.

Another approach to seismic risk analysis is based on the observation that creep events or increased seismicity sometimes bound locked segments with seismic potential. Burgmann et al. (2000) shows that two HF segments exhibiting high creep rates bound a middle segment that is believed to have produced the 1868 earthquake (M~7), and is currently locked at depths of 6-12 km. Such activity of consecutive segments could

indicate an oncoming failure of the locked segment. A somewhat similar pattern was observed prior to the November 1995 Nuweiba earthquake. During 1993, an earthquake sequence occurred at the Aragonese/Arnona fault stepover releasing approximately $3.2 \cdot 10^{17}$ N·m at the southern tip of the 1995 Nuweiba earthquake (Shamir, 1996; Hofstetter personal communication). Other significant earthquake sequences (1983, 1991) occurred in the Elat/Aragonese fault stepover near the northern tip of the 1995 Nuweiba earthquake. It should be noted that the physical relations between the increased tectonic activity at these fault stepovers and the occurrence of the Nuweiba earthquake were not resolved. In analogy to the 1983-1995 seismic activity in the Gulf of Elat (Aqaba) and to the HF creep, it could be suggested that Yotvata and Zofar creep events express the accumulation of strain along the interconnecting segment, and may indicate the growing potential for a large earthquake. It should be noted that the central AV segment, was already suggested to constitute a seismic gap (Amit et al., 2002; Salamon et al., 1996).

Finally, during the current study period (3/1995-12/2001) a correlation was found between the observed creep rates and the occurrence of moderate/large earthquakes near the creep sites. The creep rate of each particular creep event increased prior to the occurrence of an earthquake in its vicinity. This pattern was observed in Avrona and Yotvata prior to the Nuweiba sequence (including several aftershocks, $M_L<3.5$, in Southern AV), in Yotvata prior to a magnitude $M_L=4.1$ earthquake (Dec. 1999, 15 km S-SW from Yotvata), and in Zofar prior to a magnitude $M_L=4.2$ earthquake (Oct. 2001, 5 km East from Zofar feature). In addition, the creep rates at Avrona and Yotvata decrease significantly after the Nuweiba sequence (Figure 5.2). Unfortunately, we could not analyze the post earthquake creep rate changes in the cases of Zofar (after the Oct. 2001 earthquake) and Yotvata (after the Dec. 1999 earthquake) due to lack of coherent interferograms of those periods. Although each large seismic event was preceded by a creep event or by increased creep rate, this temporal correlation is irregular with precedence intervals ranging between 0.5-2.5 years. Considering the limited data on interactions between seismicity and observed creep events, the construction of an integrated (seismic and aseismic) model of the entire AV was not attempted.

6.4 Static stress transfer between seismic and aseismic events

The changes in Coulomb failure stress (ΔCFS) were calculated for Avrona and Yotvata modeled faults as induced by the Nuweiba earthquake. Based on Nuweiba earthquake parameters of Shamir (1996), the change in Coulomb failure stress ranges from +0.06 to +0.03 MPa along the four Avrona fault segments parallel to the DST and is approximately +0.02 MPa along the reverse fault at Central Avrona. In Yotvata the ΔCFS values are positive with magnitude similar to tidal stress changes (<0.01 MPa). Whether static stress changes of this magnitude could trigger slip is controversial (Emter, 1997; Vidale et al., 1998a,b; Ziv and Rubin, 2000). In any case the positive ΔCFS (Figure 6.1) do not correlate with the observed decrease in Avrona and Yotvata slip rate.

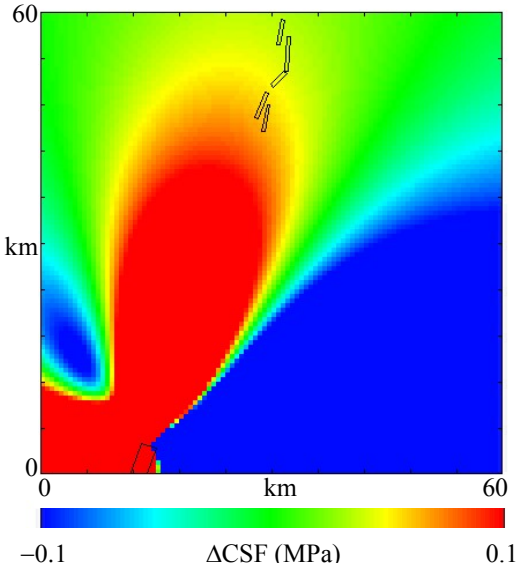

Figure 6.1. Static stress transfer from Nuweiba earthquake to the site of Avrona creep. Warm colors indicate increase in coulomb failure stress (ΔCFS) at 3 km depth calculated for faults similar to those in North and South Avrona model (i.e. DST-parallel left-lateral faults with a small component of normal faulting).

In addition to evaluating earthquake induced stress transfer, we examined the stress transfer induced by Zofar creep event (4/1998-10/2000) on the site of the M_L=4.2 earthquake that occurred near Zofar on Oct. 2001. The changes in Coulomb failure stress induced by the modeled creep event are approximately +0.01 MPa, and may not have a significant effect on the occurrence of Zofar earthquake. Additional research is needed to understand the interaction between seismic and aseismic events, and to determine the implications of such interactions on seismic hazard induced by the DST.

7. SUMMARY

A tectonic analysis of recent deformation processes along the Arava Valley (AV) section of the Dead Sea Transform (DST) was carried out. As the current tectonic activity along the AV is not well monitored and there is uncertainty whether the AV faults are locked or not, InSAR precise measurements of surface displacement were used to shed light on current deformation processes. To achieve a complete analysis we processed all available SAR data of the AV collected by the European Space Agency Remote Sensing Satellites during the period of 1995-2002.

Three deformation features were detected at fault stepovers, attributed to tectonic processes and modeled as fault dislocations:

(a) At Yotvata Playa, southern AV, uplift of ~120 mm occurred during 3/1995-5/1999 at a right stepover between Elat Fault and Aqaba-Gharandal Fault. Yotvata dislocation model consists of left-lateral slip on Elat and Aqaba-Gharandal faults with slip between 60 and 240 mm increasing towards the stepover. Both these dislocations are 9 km long and 2-2.5 km wide, and their tops are buried to depths of ~2 km. Our model indicates that this stepover is interconnected by a shallow (depth ~0.5 km) fault 6.5 km long and 4 km wide that displays oblique slip (rake 50°) of ~80 and 260 mm on its southwestern and northeastern segments, respectively. Based on Yotvata dislocation model and on an average rigidity of 20 GPa, the moment release was calculated to be $19.7 \cdot 10^{16}$ N·m, equivalent to an earthquake with magnitude M_L~5.5.

(b) Near Zofar, northern AV, subsidence of ~37 mm occurred during 4/1998-10/2000. The subsidence is located at the intersection zone of Zofar Fault (AV western border fault) and Wadi-Musa Fault that traverses the AV. Zofar dislocation model indicates that the subsidence is induced by oblique slip of 60 mm on Zofar Fault and by normal slip of 19 and 54 mm on the southeastern and northwestern segments of Wadi-Musa Fault, respectively. Zofar dislocation is 5.7 km long and 5 km wide, buried 1 km under the surface. Wadi-Musa dislocation is 7.5 km long and 4.5 km wide, with depth between 0.1 km (southeastern segment) and 0.9 km (northwestern segment). The moment released by Zofar deformation feature is $5.9 \cdot 10^{16}$ N·m, equivalent to a - M_L~5.2 earthquake.

(c) At Avrona Basin, southern AV, a complex pattern of uplift and subsidence occurred between 3/1995 and 1/1999. Two subsidence features are related to two left stepovers

between segments of Elat Fault. An uplift feature is related to a compressional right bend in Elat Fault. The left stepovers consist of four faults ~4 km long, ~5 km wide buried to depths of 0.5-1 km, and slipping between 60 and 90 mm. The compressional bend is 2.5 km long 3.5 km wide, buried less than 500 m, and accommodates ~90 mm of oblique slip. The moment released by Avrona deformation feature is $12.2 \cdot 10^{16}$ N·m, equivalent to a - M_L~5.4 earthquake.

The moment release in Zofar, Yotvata and Avrona is two orders of magnitude larger than the moment release in AV earthquakes, and it does not correlate with increase in seismicity rate, indicating that the deformation observed is induced by aseismic creep.

Our InSAR analysis has yielded the first geodetic indications for aseismic deformation along the DST. Our tectonic analysis revealed that creep at the stepover zones of Yotvata, Zofar and Avrona play a significant role in the moment balance of the AV.

REFERENCES

Adler, R., J. Forrai, and Y. Melzer, 2001, The evolution of geodetic-geodynamic control network in Israel, Isr. J. Earth Science, 50, 1, 1-7.

Al-Zoubi, A., and U. ten Brink, 2002, Lower crustal flow and the role of shear in basin subsidence: an example from the Dead Sea basin, Earth and Planet. Sci. Lett., 199, 67-69.

Ambraseys, N.N., C.P. Melville, and R.D. Adams. 1994, The seismicity of Egypt, Arabia and the Red Sea—A historical review, Cambridge, UK, Cambridge University Press, 181 p.

Ambraseys, N. and M. Free, 1997, Surface-wave magnitude calibration for European region earthquakes, J. Earthquake Eng., 1, 1-22.

Amelung, F., D.L. Galloway, J.W. Bell, H.A. Zebker, and R.J. Laczniak. 1999, Sensing the ups and downs of Las Vegas: InSAR reveals structural control of land subsidence and aquifer-system deformation: Geology. 27,483–486.

Amit, R., E. Zilberman, N. Porat, and Y. Enzel, 1999, Relief inversion the Avrona playa as evidence of large-magnitude historical earthquakes, southern Arava Valley, Dead Sea Rift, Quaternary Res., 52, 76-91.

Amit, R., E. Zilberman, Y. Enzel, and N. Porat, 2002, Paleoseismic evidence for the time dependency of seismic response on a fault system in the southern Arava Valley, Dead Sea rift, Israel: Geological Society of America. 114, 192-206.

Baer, G., D. Sandwell, S. Williams, G. Shamir, and Y. Bock. 1999, Coseismic deformation associated with the November 1995, MW = 7.1 Nuweiba earthquake, Gulf of Elat (Aqaba), detected by synthetic aperture Radar interferometry: Journal of Geophysical Research. 104, 25221–25232.

Baer, G., G. Shamir, D. Sandwell, and Y. Bock. 2001, Crustal deformation during 6 years spanning the MW = 7.2 1995 Nuweiba earthquake, analyzed by Interferometric Synthetic Aperture Radar: Israel Journal of Earth Science. 50, 9-22.

Baer, G., U. Schattner, D. Wachs, D. Sandwell, S. Wdowinski, and S. Frydman. 2002, The lowest place on Earth is subsiding—An InSAR (interferometric synthetic aperture Radar) perspective: Geological Society of America Bulletin. 114, 1, 12–23.

Bakun, W. H., and A. G. Lindh, 1985, The Parkfield, California, earthquake prediction experiment, Science, 229, 619-624.

Bartov, Y., 1994, Geological photomap of Israel and adjacent areas; seismicity of Israel and adjacent areas, Institute for Petroleum Research and Geophysics, Holom, Israel

Bartov, Y., Y. Avni, R. Calvo, and U. Frieslander, 1998, The Zofar fault – a major intra-rift feature in the Arava rift valley, Geological Survey of Israel, current research 11, 27-32.

Bartov, Y., A. Sneh, L. Fleischer, V. Arad, and M. Rosensaft. 2002, Map of potentially active faults in Israel: Geological Survey of Israel Report GSI/29/2002, 28 p.

Ben Gai, Y., Y. Rotstein, and Y. Bartov, 1993, High resolution seismic reflection survey in the Avrona area, Holon, Israel, Institute of Petroleum and Geophysics, Report 1/357/93, 18p.

Ben-Menahem, A. and E. Aboodi, 1981, Micro- and macro-seismicity of the Dead Sea rift and off-coast eastern Mediterranean, Tectonophysics, 80, 199-233.

Ben-Menahem, A. 1981, Variation of slip and creep along the Levant rift over the past 4500 yr: Tectonophysics. 80, 183–197.

Ben-Menahem, A. 1991, Four thousand years of seismicity along the Dead Sea rift: Journal of Geophysical Research. 96B,20195–20216.

Ben-Zion, Y., J. Rice, and R. Dmowska, 1993, Interaction of the San Andreas Fault creeping segment with adjacent great rupture zones and earthquake recurrence at Parkfield, J. Geophys. Res., 98, 2135-2144.

Brune, J. N., 1968, Seismic moment, seismicity, and slip rate along major fault zones, J. Geophys. Res., 73, 777-784.

Brune, J. N., 1970, Tectonic stress and the spectra of seismic shear waves from earthquakes, J. Geophys. Res., 75, 4997-5009.

Burgmann, R. D. Schmidt, R.M. Nadeau, M. d'Alessio, E. Fielding, D. Manaker, T. McEvilly, and M.H. Murray, 2000, Earthquake potential along the Northern Hayward fault, California, Science, 289, 1178-1182.

Burgmann, R., P. A. Rosen, and E. J. Fielding. 2000, Synthetic aperture Radar interferometry to measure earth's topography and its deformation: Annual Reviews Earth Planetary Science. 28, 169-209.

Curlander, J.C., and R.N. McDonough. 1991, Synthetic aperture radar: Systems and signal processing: New York, John Wiley and Sons, Inc., 647 p.

DeMets, C., Gordon, R. G,. Argus, D. F. and Stein, S., 1994. Effects of recent revisions to the geomagnetic reversal time scale on estimates of current plate motions, Geophysical Research Letters. 21, 2191-2194.

Desert Group, 2002, The DESERT passive seismic experiment 2000/2001 in the Middle East, ORFEUS Newsletter, 4, 1-6.

Desert Group, Weber M., Abu-Ayyash K., Abueladas A., Agnon A., Al-Amoush H., Babeyko A., Bartov Y., Baumann M., Ben-Avraham Z., Bock G., Bribach J., El-Kelani R., Förster A., Förster H.-J., Frieslander U., Garfunkel Z., Grunewald S., Götze H.J., Haak V., Haberland C., Hassouneh M., Helwig S., Hofstetter A., Jäckel K.-H., Kesten D., Kind R., Maercklin N., Mechie J., Mohsen A., Neubauer F.M., Oberhänsli R., Qabbani I., Ritter O., Rümpker G., Rybakov M., Ryberg T., Scherbaum F., Schmidt J., Schulze A., Sobolev S., Stiller M., Thoss H., Weckmann U., Wylegalla K., 2004, Geophys. J. Int., 156, 3, 655-681.

Emter, D., 1997, Tidal triggering of earthquakes and volcanic events, in Tidal Phenomena, Lect. Notes in Earth Sci., vol. 66, edited by H. Wilhelm, W. Zurn, and H.G. Wenzel, pp. 293-310, Springer-Verlag, New York.

Enzel, Y., R. Amit, J. Bruce, J. Harrison, and N. Porat, 1994, Morphologic dating of fault scarps and terrace rises in the southern Arava, Israel: Comparison to other age-dating techniques and implications for paleoseismicity: Israel Journal of Earth Science. 43, 91-103.

Freund, R., 1970, The geometry of faulting in the Galillee: Israel Jurnal of Earth Science. 19, 117-140.

Freund, R., I. Zak, and Z. Garfunkel. 1968, Age and rate of the sinistral movement along the Dead Sea Rift: Nature. 220, 253-255.

Frieslander, U., 1995, The subsurface of the southern Arava Valley – results from seismic surveys, Holon, Israel, The Institute of Petroleum and Geophysics, Report 846/257/92(c).

Frieslander, U., 2000, The structure of the Dead Sea transform emphasizing the Arava using new geophysical data [Ph.D. thesis]: Hebrew University of Jerusalem, 101 p.

Gabriel, A.K., and R.M. Goldstein, 1988, Crossed orbit interferometry – theory and experimental results from SIR-B, Int. J. Remote Sens., 9, 857-872.

Gabriel, A.K., R.M. Goldstein, and H.A. Zebker. 1989, Mapping small elevation changes over large areas: Differential Radar interferometry: Journal of Geophysical Research. 94, 9183–9191.

Gao, S., P. Silver, and A. Linde, 2000, Analysis of deformation data at Parkfield, California: Detection of a long-term strain transient, J. Geophys. Res., 105, 2955-2967.

Gardosh, M., Z. Reches, and Z. Garfunkel, 1990, Holocene tectonic deformation along the western margins of the Dead Sea, Tectonophysics, 180, 123-137.

Gardosh, M., E. Kashai, S. Salhov, H. Shulman, and E. Tannenbaum, 1997. Hydrocarbon exploration in the southern Dead Sea basin. In T. M. Niemi, Z. Ben-Avraham & J. R. Gat, The Dead Sea: the lake and its setting, Oxford University Press.

Garfunkel, Z., 1970, The tectonics of the western margin of the southern Arava, Ph.D. Thesis, Hebrew university, Jerusalem, 204 pp. (in Hebrew, English abst.).

Garfunkel, Z., I. Zak, and R. Freund, 1981, Active faulting in the Dead Sea rift, Tectonophysics. 80,1–26.

Garfunkel, Z., 1981, Internal structure of the Dead Sea leaky transform in relation to plate kinematics, Tectonophysics. 80, 81–108.

GII, 2000, Earthquakes in and around Israel, 1900-2000, Geophysical Institute of Israel.

Ginat, H., Y. Enzel, and Y. Avni. 1998, Translocated Plio-Pleistocene drainage systems along the Arava fault of the Dead Sea Transform: Tectonophysics, 284, 151-160.

Goldstein R.M., H. Engelhardt, B. Kamb, and R.M. Frolich, 1993, Satellite radar interferometry for monitoring ice sheet motion: Application to an Antarctic ice stream, Science, 262, 1525-1530.

Goldstein, R.M., and H.A. Zebker. 1987, Interferometric Radar measurements of ocean surface currents: Nature 328:707-9.

Hall, J. K., 1993, The GSI Digital Terrain Model (DTM) completed. In R. Bogoch and Y. Eshet (eds.), GSI Current Research, 8, 47-50.

Hall, J. K., R. Weinberger, S. Marco, and G. Steinitz, 1999, Test of the Accuracy of the DTM of Israel, GSI Report TR – GSI/1/99, 16 pp.

Hanssen, R. F., 2001, Radar interferometry data interpretation and error analysis, Kluwer academic publishers - Dordrecht/Boston/London, 308 pp.

Hydrologic Service annual report, 1997

Jaeger, J.C., and Cook, N.G.W., 1979, Fundamentals of rock mechanics (3d ed.): London, Chapman and Hall, 593 p.

Joffe, S., and Z. Garfunkel, 1987. Plate kinematics of the circum Red Sea - a re-evaluation. Tectonophysics, 141, 5-22.

Kanamori, H. and D. L. Anderson, 1975, Theoretical basis of some empirical relations in seismology, Bull. Seismol. Soc. Am., 65, 1073-1095.

Karcz, I., H. Pelzer, J. van Mierlo, and K. Foppe, 1997, Geodetic Monitoring of Crustal Movements Along the Dead Sea Jordan Rift (DSR) - Retrospect and Prospects, Proceedings at 13th GIF Meeting. In: „The Dead Sea Rift as a Unique Global Site“ , Dead Sea, Israel, Terra Nostra, Schriften der Alfred-Wegener-Stiftung 4/97.

Kiremidjian, A.S. and T. Anagnos, 1984, Stochastic Slip-predictable model for earthquake occurrences, Bull. Seismol. Soc. Am., 74, 2, 739-755.

Klinger, Y., J. P. Avouac, N. Abou Karaki, L. Dorbath, D. Bourles, and J. L. Reyss. 2000a, Slip rate on the Dead Sea Transform fault in northern Araba valley (Jordan): Geophysical Journal International. 142, 755-768.

Klinger, Y., J. P. Avouac, N. Abou Karaki, L. Dorbath, and N. Tisnerat, 2000b, Seismic behavior of the Dead Sea fault along Araba valley, Jordan, Geophys. J. Int., 142, 769-782.

Kostrov, V. V., 1974, Seismic moment and energy of earthquakes, and seismic flow of rock, Earth Physics, 1, 23-40.

Lienkaemper, J., J. Galehouse, and R. Simpson, 2001, Long-term monitoring of creep rate along the Hayward fault and evidence for a lasting creep response to 1989 Loma Prieta earthquake, Geophys. Res. Lett., 28, 2265-2268.

Lienkaemper, J., G. Borchardt, and M. Lisowski, 1991, Historic creep rate and potential for seismic slip along the Hayward fault, California, J. Geophys. Res., 96, 18261-18283.

Lienkaemper, J., and W. H. Prescott, 1989, Historic surface slip along the San Andreas fault near Parkfield, California, J. Geophys. Res., 94, 17647-17670.

Lyons, S., and D. Sandwell, 2003, Fault creep along the southern San Andreas from interferometric synthetic aperture radar, permanent scatterers, and stacking, J. Geophys. Res., 108(B1), 2074, doi: 10.1029/2002JB001831.

Malservisi, R., C. Gans, and K.P. Furlong, 2003, Numerical modeling of strike-slip creeping faults and implications for the Hayward fault, California, Tectonophysics, 361, 121-137.

Marco, S., 1996. Paleomagnetism and paleoseismology in the Late Pleistocene, Dead Sea Graben. Ph.D. Thesis, Hebrew Univ. Jerusalem.

Marco, S., M. Stein, A. Agnon, and H. Ron, 1996. Long term earthquake clustering: a 50,000 year paleoseismic record in the Dead Sea Graben. .Journal of Geophysical Research. 101, 6179-6192.

Maruyama, T. F., 1963, On the force equivalent of dynamic elastic dislocations with reference to the earthquake mechanism, Bull. Earthquake Res. Inst. Tokyo Univ., 41, 467.

Massonnet, D., and T. Rabaute. 1993, Radar interferometry: Limits and potential: IEEE Transactions on Geoscience and Remote Sensing. 31,455–464.

Massonnet, D., M. Rossi, C. Carmona, F. Adragna, G. Peltzer, K. Feigl, and T. Rabaute. 1993, The displacement field of the Landers earthquake mapped by Radar interferometry: Nature. 364, 138–142.

Massonnet, D., K. Feigl, M. Rossi, F. Adragna, 1994, Radar interferometric mapping of deformation in the year after the Landers earthquake. Nature, 369, 227-230.

Massonnet, D., T. Holzer, and H. Vadon, 1997, Land subsidence caused by the East Mesa geothermal field, California, observed using SAR interferometry, Geophys. Res. Lett., 24, 901-904.

Massonnet, D., and K. Feigl, 1995a, Discrimination of geophysical phenomena in satellite radar interferograms, Geophys. Res. Lett. 22, 1537-1540.

Massonnet, D., and K. Feigl. 1998, Radar interferometry and its application to changes in the Earth's surface: Reviews of Geophysics. 36, 441–500.

Nadeau, R. and T. McEvilly, 1999, Fault slip rates at depth from recurrence intervals of repeating microearthquakes, Science, 285, 718-721.

North, R. G., 1974, Seismic slip rates in the Mediterranean and Middle East, Nature, 252, 560-563.

Okada, Y., 1985. Surface deformation due to shear and tensile faults in a half-space. Bulletin of the Seismological Society of America., 75, 1135-1154.

Okada, Y., 1992. Internal deformation due to shear and tensile faults in a half-space. Bulletin of the Seismological Society of America., 82, 1018-1040.

Oppenheimer, D.H., P.A. Reasenberg, and R.W. Simpson, 1988, Fault plane solutions for the 1984 Morgan Hill, California, earthquake sequence: Evidence for the state of stress on the Calaveras fault, J. Geophys. Res. 93, 9007-9026.

Ostrovsky, E., 2001, The G1 GPS geodetic-geodynamic reference network: final processing results, Isr. J. Earth Science, 50,1, 29-37.

Pe'eri, S., S. Wdowinski, A. Shtibelman, N. Bechor, Y. Bock, R. Nikolaidis, and M. van Domselaar, 2002, Current plate motions across the Dead Sea fault from three years of continuous GPS monitoring, Geophys. Res. Lett., 29, 14, 10.1029/2001GL013879, 2002.

Peltzer, G., P. Rosen, F. Rogez, and K. Hudnut, 1996, Postseismic rebound in fault step-overs caused by pore fluid-flow. Science, 273, 1202-1204.

Prescott, W.H., and M. Lisowski, 1983, Strain accumulation along the San Andreas fault system East of San Francisco Bay, California, Tectonophysics, 97, 41-56.

Price, E.J., and D.T. Sandwell. 1998, Small-scale deformation associated with the June 28, Landers, California, earthquake mapped by synthetic aperture Radar interferometry phase gradients, J. Geophys. Res. 103, 27,001-27,016.

Quennel, A.M., 1959. Tectonics of the Dead Sea Rift: 20th International Geologic Congress. 3 85-405.

Reches, Z., J. Erez, and Z. Garfunkel, 1987. Sedimentary and tectonic features in the northwestern Gulf of Elat, Israel. Tectonophysics, 141, 169-180.

Roeloffs, E. and J. Langbein, 1994, The earthquake prediction experiment at Parkfield, California, Rev. Geophys., 32, 215-336.

Roeloffs, E. 2000, The Parkfield, California earthquake experiment: An update in 2000, Curr. Sci., 79, 1226-1235.

Rosen, P.A., S. Hensley, H.A. Zebker, F.H. Webb, and E. Fielding. 1996, Surface deformation and coherence measurements of Kilauea Volcano, Hawaii from SIR- C Radar interferometry: Journal of Geophysical Research. 101,23109–23125.

Salamon, A., 1993, Seismotectonic analysis of earthquakes in Israel and adjacent areas: Ph.D. thesis, Hebrew University Jerusalem, 135 p.

Salamon, A., A., Hofstetter, Z. Garfunkel and H. Ron, 2003, Seismotectonics of the Sinai subplate – the eastern Mediterranean region, Geophys. J. Int. 155, 149-173.

Salamon, A., A., Hofstetter, Z. Garfunkel and H. Ron. 1996, Seismicity of the Mediterranean region: Perspective from the Sinai subplate, Tectonophysics, 263, 293-305.

Savage, J., 1980, Dislocations in Seismology, in Nabbaro, E. (ed.), Dislocations in Solids, p.258-310.

Scharroo, R., and P. Visser. 1998, Precise orbit determination and gravity field improvement for the ERS satellites: Journal of Geophysical Research. 103,8113–8127.

Scholz, C.H., 1990, The mechanics of earthquakes and faulting: Cambridge, U.K., Cambridge University Press, 439. p.

Shamir, G., 1996, The November 22, l995, Nuweiba earthquake, Gulf of Elat: Mechanical analysis, Holon, Israel, Institute of Petroleum Research and Geophysics, Report 550/87/96 (114), 33 p.

Shapira, A. and A. Hofstetter, 1993, Source parameters and scaling relationships of earthquakes in Israel, Tectonophysics, 217, 217–226.

Shapira, A., and G. Shamir. 1994, Seismicity parameters of seismic zones in and around Israel: Holon, Israel, Institute of Petroleum Research and Geophysics, Report Z1/567/79 (109), 20 p.

Shapira, A. 1997, Seismicity patterns of the Dead Sea transform—A review: Dead Sea, Israel, 13th GIF meeting on the Dead Sea rift as a unique global site, Proceedings, 160 p.

Shapira, A. and A. Hofstetter, 2000, Determination of earthquake energy release in Eastern Mediterranean region, Geophys. J. Int., 143, 898–906.

Shimazaki, K. and T. Nakata, 1980, Time predictable recurrence model for large earthquakes, Geoph. Res. Lett., 7, 279-282.

Shtivelman, V., U. Frieslander, E. Zilberman, and R. Amit, 1997, High resolution seismic reflection survey in the Evrona area, southern Arava valley, GSI report no. GSI/5/97.

Simpson, R., S. Schulz, L. Dietz, and R. Burford, 1988, The response of creeping parts of the San Andreas fault to earthquakes on nearby faults: Two examples, Pure Appl. Geophys. 126, 665-685.

Simpson, R.W., J.J. Lienkaemper, and J.S. Galehouse, 2001, Variation in creep rate along the Hayward fault, California, interpreted as changes in depth of creep, Geophys. Res. Lett., 28, 2269-2272.

Smith, D. E., R. Kolenkiewicz, J. W. Robbins, P. J. Dunn, and M. H. Torrence, 1994, Horizontal crustal motion in the central and eastern Mediterranean inferred from satellite Laser ranging measurements, Geophys. Res. Lett., 21, 1979-1982.

Stein, R.S., and M. Lisowski, 1983, The 1979 Homestead Valley earthquake sequence, California: Control of aftershock and postseismic deformation, J. Geohys. Res., 88, 6477-6490.

Stein, R.S., 1999, The role of stress transfer in earthquake occurrence, Nature, 402, 605-609.

Tarayre, H. and D. Massonnet, 1996, Atmospheric propagation heterogeneities revealed by ERS-1 interferometry, Geophys. Res. Lett., 23, 9, 989--992.

ten Brink, U.S., Z. Ben-Avraham, R.E. Bell, M. Hassouneh, D.F. Coleman, G. Andreasen, G. Tibor, and B. Coakley, 1993, Structure of the Dead Sea pull-apart basin from gravity analyses, J. Geophys. Res., 98, 21,877-21,894.

ten-Brink, U.S., M. Rybakov, A.S. Al-Zoubi, M. Hassouneh, U. Frieslander, A.T. Batayneh, V. Goldschmidt, M.N. Daoud, and J.K. Hall, 1999, Anatomy of the Dead Sea transform: does it reflect continuous changes in plate motion?, Geology, 27, 10, 887-890.

Tullis, T., 1999, Deep slip rates on the San Andreas fault, Science, 285, 671-672.

Van Eck, T., and A. Hofstetter, 1989, Microearthquake activity in the Dead Sea region, Geophys. J. Int., 99, 605–620.

Vidale, J. E., D.C. Agnew, M.J.S. Johnston, and D.H. Oppenheimer, 1998a, Absence of earthquake correlation with Earth tides: An indication of high preseismic fault stress rate, J. Geophys. Res., 103, 24567-24572.

Vidale, J. E., D.C. Agnew, D.H. Oppenheimer, D. Rodriques, and H. Huston, 1998b, A weak correlation between earthquake and extensional normal stress and stress rate from lunar tides (abstract), EOS Trans. AGU, 79, (45), Fall Meet. Suppl. F641.

Wdowinski, S., Y. Bock, Y. Forrai, Y. Melzer, E. Ostrovsky, G. Baer and D. Levitte, The GIL network of continuous GPS monitoring in Israel for geodetic and geophysical applications, Isr. J. Earth Sci., 50, 1, 39-47, 2001.

Wdowinski S., Y. Bock, G. Baer, L. Prawirodirdjo, N. Bechor, S. Naaman, Knafo, Y. Forrai, and Y. Melzer, In press, GPS measurements of current crustal movements along the Dead Sea Fault, in review for J. Geophys. Res.

Working Group on California Earthquake Probabilities (WG99), 1999, Earthquake probabilities in the San Francisco Bay region: 2000 to 2030 – a summary of findings, U.S. Geol. Surv. Open File Rep. 99-517.

Wright, T.J., B.E. Parsons and Z. Lu, 2004, Toward mapping surface deformation in three dimensions using InSAR, Geophys. Res. Lett., 31(1), L01607, doi:10.1029/2003GL018827.

Wyss, M., L. Slater, and R.O. Burford, 1990, Decrease in deformation rate as a possible precursor to the next Parkfield earthquake, Nature, 345, 428-431.

Zak, I., and R. Fruend, 1966, Recent strike slip motions along the Dead Sea Rift, Israel Journal of Earth Science, 15, 33-37.

Zak, I. 1967, The geology of Mount Sedom, Ph.D. thesis, Jerusalem, Hebrew University, 208 p

Zebker, H.A., and R.M. Goldstein. 1986, Topographic mapping from interferometric SAR observations, J. Geophys. Res., 91, 4993-5001.

Zebker, H.A., C.L. Werner, P.A. Rosen, and S. Hensley. 1994a, Accuracy of topographic maps derived from ERS-1 interferometric Radar: IEEE Transactions on Geoscience and Remote Sensing. 32,823–836.

Zebker, H.A., P.A. Rosen, and R.M. Goldstein. 1994b, On the derivation of coseismic displacement fields using differential Radar interferometry: The Landers earthquake: J. Geophys. Res., 99, 19617–19634.

Zebker, H. A., P.A. Rosen, and S. Hensley. 1997, Atmospheric effects in interferometric synthetic aperture radar surface deformation and topographic maps, J. Geophys. Res., 102, 7547-7563.

Zilberman, E., R. Amit, N. Porat, and U. Avner. 1998, Relocation of the epicenter of the 1068 earthquake in the Avrona playa, southern Dead Sea rift, using paleoseismic and archaeoseismic evidences, ESC XXVI General Assembly, Tel Aviv, Israel, 24 p.

Ziv A., and A.M. Rubin, 2000, Static stress transfer and earthquake triggering: No lower threshold in sight?, J. Geophys. Res., 105, 13631-13642.

ברטוב, י., 1994, הגיאולוגיה של הערבה דברי הסבר למפה גיאולוגית, ירושלים, ישראל, המכון הגיאולוגי דו״ח GSI/4/94.

Appendix A. Well location and Hydrologic Service I.D. number

Avrona region

Well name	I.D.	longitude	latitude
elat 1	88614601	146.8	886.44
sabcha 18	89114801	148.66	891.64
amram 2	89314001	148	893.2
amram 3	89314701	147.3	893.6
ora 4	90014801	148.52	900.31
ora 6	90215001	150.74	902.67
ora 7	90114801	148.77	901.55
timna 50	90415001	150.1	904.8

Zofar region

Well name	I.D.	longitude	latitude
omer 1	98916701	167	989.4
zofar 3	99116702	167.43	991.06
zofar 11	99417202	172.43	994.49
zofar 4	99016701	167.35	990.35
zofar 7	99416901	169.44	994.41
zofar 10	99217101	171.66	992.98

Yotvata region

Well name	I.D.	longitude	latitude
timna zimche shmama	91415202	152.79	914.07
yotvata 21/7	91515201	152.2	915.52
yotvata 19/25	91915201	152.97	919.99
yotvata 9 t	92215505	155.08	922.21
yotvata 9	92215501	155.08	922.24
yotvata 5	92415501	155.74	924.92

longitude and latitude coordinates are given in - old Israel coordinate system

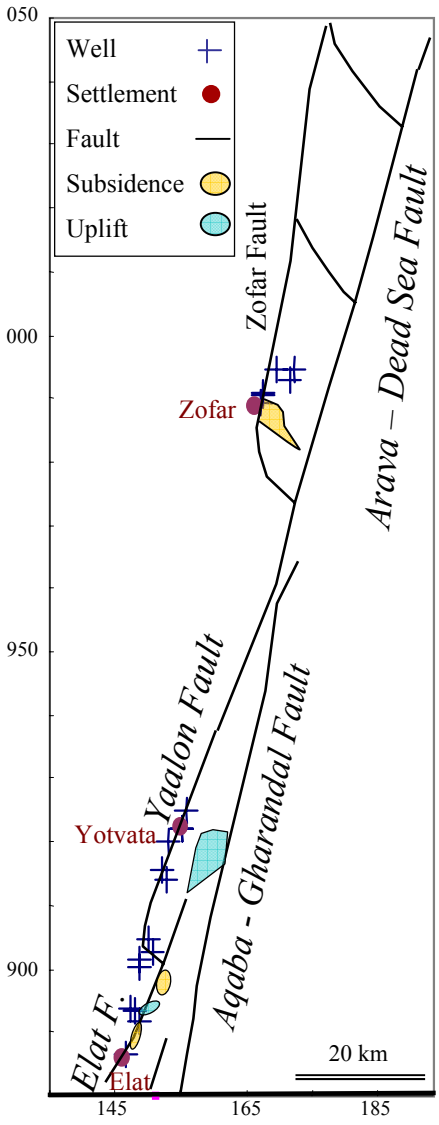

אירועי המעוות הטקטוני בצופר, יוטבתה ועברונה אינם מלווים בעליה בפעילות הסיסמית באתרים אלו. בנוסף, המומנט המשוחרר באירועים אלו גדול בשני סדרי גודל מזה המשוחרר ברעידות אדמה לאורך הערבה כולה במשך תקופת המחקר, ושחרורו הנו רציף. לכן, ניתן לקבוע שמעוות זה אינו סיסמי אלא נובע מזחילה במדרגי-העתק. בהנחה שקצב ההעתקה האפקית לאורך דרום טרנספורם ים המלח הוא 3.1 מ"מ בשנה (מנתוני GPS), ניתן לקבוע שהזחילה במדרגי-העתק לאורך הערבה משחררת כ- 50% מהמומנט הנצבר לאורכה במשך השנים 1995-1999.

שיטת ההתאבכות מלווין הניבה מדידות גיאודטיות חסרות תקדים של זחילה לא-סיסמית לאורך טרנספורם ים המלח בערבה. ניתוח המעוות הטקטוני הראה שאירועי הזחילה שנמדדו במדרגי-העתק בצופר, יוטבתה ועברונה משחררים חלק משמעותי מהמומנט הנצבר לאורך הערבה כולה, ועל כן מהווים גורם חשוב במאזן האנרגיה הסיסמית בקטע זה של גבול הלוחות. אף על פי שלא נמדדה העתקה/זחילה לאורך מקטעי ההעתק הראשיים בערבה (מחוץ לאזורי המדרג שהוזכרו), יתכן שהמעוות שנצפה באזורי המדרג משקף תנועה על מקטעי ההעתק הראשיים בקצב נמוך מ- 4 מ"מ בשנה, המהווה סף המדידה במחקר הנוכחי לתנועות אופקיות מקבילות לטרנספורם ים המלח.

מאפייני ההעתקים וההעתקה עליהם שגרמו להעתקות פני השטח.

התהליכים הטקטוניים שנמדדו ותוארו במודל הנם:

(א) במלחת יוטבתה, דרום הערבה, במהלך התקופה 3/1995-5/1999 נמדדה התרוממות של עד 120 מ"מ בשטח של כשלושים קמ"ר. מודל ההעתקה של יוטבתה מורכב מתנועה שמאלית מצטברת של 60-240 מ"מ על גבי המקטעים של העתקי אילת ועקבה-ע'רנדל (בסמוך למדרג שבין העתקים אלו התנועה מרבית, והיא דועכת הרחק מהמדרג). בנוסף, המודל כולל העתק רדוד המחבר בין העתקי אילת ועקבה-ע'רנדל, ועליו מתבצעת תנועה הפוכה ושמאלית (rake ~50°). על פי המודל, ההעתקה על העתקי אילת ועקבה-ע'רנדל מתבצעת על משטחי העתק שאורכם כ- 9 ק"מ, רוחבם 2-2.5 ק"מ ועומק קבורתם כ- 2 ק"מ מתחת לפני השטח. ההעתק הרדוד שבמרכז המדרג אורכו 6.5 ק"מ רוחבו 4 ק"מ ועומקו כ- 0.5 ק"מ. סך התנועה על גבי העתק זה נעה בין 80 מ"מ בצדו הדרום-מערבי ל- 260 מ"מ בצדו הצפון-מזרחי. בהתבסס על מודל זה של הפעילות הטקטונית ביוטבתה ועל מקדם גזירה ממוצע של 20 GPa בשכבות הסלע הרדודות (עמק 0-10 ק"מ) בערבה, חושב המומנט ששוחרר על ידי ההעתקה המדודה, והוא כ- $19.7\cdot10^{16}$ N·m, ערך התואם רעידת אדמה במגניטודה M_L~5.5 (בהנחה ששחרור המומנט היה מיידי).

(ב) באזור צופר, צפון הערבה, במהלך התקופה 4/1998-10/2000 נמדדה שקיעה של עד 37 מ"מ בשטח של כ- 10 קמ"ר. השקיעה נצפתה באזור המפגש של העתק צופר המהווה מקטע מהעתקי הגבול המערבי של הערבה, והעתק ואדי-מוסא שהנו העתק נורמלי רדוד החוצה את אגן צופר. מודל ההעתקה בצופר מעיד כי המעוות הנמדד נגרם על ידי תנועה אלכסונית (נורמלית ושמאלית, rake -25°) של כ- 60 מ"מ על העתק צופר, ותנועה של 19 ו- 54 מ"מ על המקטעים הדרום-מזרחי והצפון-מערבי של העתק ואדי-מוסא, בהתאמה. על פי המודל ההעתקה על העתק צופר התבצעה על משטח שאורכו כ- 5.7 ק"מ, רוחבו 5 ק"מ ועומקו כ- 1 ק"מ, וההעתקה על העתק ואדי-מוסא התבצעה על משטח שאורכו כ- 7.5 ק"מ, רוחבו 4.5 ק"מ ועומקו קטן מק"מ אחד. בהתבסס על מודל זה, המומנט ששוחרר בפעילות טקטונית בצופר הוא כ- $5.9\cdot10^{16}$ N·m, ערך התואם רעידת אדמה במגניטודה M_L~5.2.

(ג) באגן עברונה, דרום הערבה, במהלך התקופה 1/1995-3/1999 מופו שני אתרי שקיעה וביניהם אתר התרוממות; שטח כל אתר קטן מ- 5 קמ"ר. מודל ההעתקה בעברונה מעיד כי שתי השקיעות מיוחסות להעתקה שמאלית עם רכיב נורמלי (rake -20° - -40°) על מקטעים של העתק אילת היוצרים שני מדרגים שמאליים, וההתרוממות מיחסת להעתקה שמאלית והפוכה (rake +20°) על מקטע המהווה כיפוף ימני (בכוון N45°E) בתוואי העתק אילת. על פי המודל, במדרגים השמאליים התבצעה העתקה של 60-90 מ"מ על ארבעה משטחי העתק באורך כ- 4 ק"מ, רוחב כ- 5 ק"מ ועומק של 0.5-1 ק"מ. אורך ההעתק הגורם להתרוממות כ- 2.5 ק"מ, רוחבו כ- 3.5 ק"מ, עומקו פחות מ- 0.5 ק"מ, ומידת התנועה עליו היא כ- 90 מ"מ. בהתבסס על נתונים אלו, המומנט ששוחרר בפעילות טקטונית בעברונה הוא כ- $12.2\cdot10^{16}$ N·m, ערך התואם רעידת אדמה במגניטודה M_L~5.4.

תקציר מורחב

אנו מציגים ניתוח של המעוות העכשווי לאורך הערבה, דרום טרנספורם ים המלח, המבוסס על ניטור באמצעות התאבכות נתוני רדאר מלווינים. שיטה חדשנית זאת המבוססת על השוואת מדידות לווין בזמנים שונים מאפשרת ניטור תנועות מזעריות של פני השטח בדיוק ובהפרדה מרחבית חסרות תקדים.

טרנספורם ים המלח הנו גבול לוחות שלאורכו מתקיימת גזירה שמאלית בין לוח ערב ללוח ישראל-סיני. הערבה הנה שקע טקטוני באורך כ- 160 ק"מ לאורך טרנספורם ים המלח, בין ים-המלח בצפון ומפרץ אילת (עקבה) בדרום. תוואי ההעתקים הראשיים לאורך הערבה הנם פשוטים יחסית ומעידים על כך שההעתקה לאורכם הנה אופקית בעיקרה. עם זאת מדרגי העתק שמאליים וימניים יוצרים לאורך הערבה אגני מתיחה ומבני לחיצה, בהתאמה. הערבה מורכבת ממספר אגנים מאורכים התחומים על ידי מקטעי העתק תת-מקבילים (אזימוט 20°), אורך האגנים עד עשרות קילומטרים, עומקם בין מאות מטרים למספר קילומטרים, והורבדו בהם סלעי משקע יבשתיים מהמיוקן ועד ההולוקן. רשום רעידות האדמה לאורך טרנספורם ים המלח מעיד כי הפעילות הסיסמית לאורך הערבה נמוכה משמעותית מהפעילות הסיסמית באזורים שכנים לאורך הטרנספורם. עובדה זאת, בצרוף עם עדויות פאלאו-סיסמיות על ירידה בעצמת רעידות האדמה ועדויות מכשירניות לכך שהפעילות הסיסמית ב- 15 השנים האחרונות הנה זניחה, מעלה חשד שטרנספורם ים המלח הנו נעול לאורך הערבה. אם כך אזור הערבה צובר אנרגיה סיסמית יתרה ומהווה אזור של פער סיסמי. בנוסף, קצב התנועה העכשווית ואופן חלוקתה על מקטעי ההעתק לאורך הערבה אינם ניתנים לקביעה מדויקת בשל מחסור בנתונים גיאודטיים.

פיתוח שיטת ההתאבכות מלווין מאפשר מדידת מעוותים עכשוויים בפני השטח בדיוק של מילימטרים בודדים ובהפרדה מרחבית של 5 על 20 מטרים. בשיטה זו לווין שולח קרינה אלקטרומגנטית לקרקע ומודד את החזר הקרינה מהקרקע (משרעת ומופע). מופע הגלים מתכונתי למרחק בין הלווין למטרה, ולכן הפרש המופע בין שתי מדידות שהתבצעו בזמנים שונים מאפשר חישוב תנועות פני שטח בכיוון הלווין שהתרחשו בפרק הזמן בין המדידות. היות ומיקום הלווין בעת ביצוע שתי המדידות אינו זהה לחלוטין, הפרש המופע מושפע גם מתבליט פני השטח, ויש להפחית את תרומת התבליט בכדי לבודד את מעוות פני השטח. לאחר ניכוי הפרשי המופע הללו מתקבלת תמונת התאבכות שבה כל מחזור של הפרש מופע מתכונתי להעתקה של חצי אורך גל בכיוון הלווין (28 מילימטר בעבודה הנוכחית).

מטרת המחקר היא לזהות ולמדוד תנועות פני שטח שהתרחשו בערבה במהלך השנים האחרונות, לבודד את התהליכים הטקטוניים הגורמים לתנועות אלו, ולהעריך את חשיבותם במאזן האנרגיה הסיסמית לאורך מקטעי טרנספורם ים המלח בערבה. במהלך המחקר עובדו כל הנתונים המשמעותיים שנמדדו על ידי שני לווייני סוכנות החלל האירופאית (ERS-1,2) והוכנו כ- 90 תמונות התאבכות המייצגות תקופות של 74-2 חודשים במהלך השנים 2001-1995. שלושה אתרי מעוות המיוחסים לתהליכים טקטוניים אותרו באזורי מדרג-העתק לאורך הערבה. כל אתר תואר על ידי מודל המפרט את

משרד התשתיות הלאומיות
המכון הגיאולוגי

המעוות העכשווי בדרום טרנספורם ים המלח: מדידות באמצעות אינטרפרומטריה של רדאר ומשמעויות טקטוניות

ירון פינצי

עבודה זו הוגשה כחיבור לקבלת תואר "מוסמך במדעי הטבע" במכון למדעי כדור הארץ, האוניברסיטה העברית בירושלים, בהדרכתם של:

פרופ' זאב רכס, המכון למדעי כדור הארץ, האוניברסיטה העברית בירושלים
דר' גידי בר, המכון הגיאולוגי

דו"ח מס' GSI/24/04 ירושלים, יוני 2005